ELECTROSPUN NANOFIBERS FOR REGENERATIVE MEDICINE

A Dissertation
Presented to
The Academic Faculty

by

Wenying Liu

In Partial Fulfillment
of the Requirements for the Degree
Doctor of Philosophy in the
School of Chemical and Biomolecular Engineering

Georgia Institute of Technology
December 2014

Copyright 2014 © by Wenying Liu

ELECTROSPUN NANOFIBERS FOR REGENERATIVE MEDICINE

Approved by:

Dr. Younan Xia, Advisor
Department of Biomedical Engineering
Georgia Institute of Technology

Dr. Sven H. Behrens
School of Chemical & Biomolecular Engineering
Georgia Institute of Technology

Dr. Julie A. Champion
School of Chemical & Biomolecular Engineering
Georgia Institute of Technology

Dr. Andrés J. García
School of Mechanical Engineering
Georgia Institute of Technology

Dr. Lakeshia J. Taite
School of Chemical & Biomolecular Engineering
Georgia Institute of Technology

Date Approved: August 25, 2014

Dedicated to my loving family for their unwavering support and faith in me.

ACKNOWLEDGEMENTS

Over the past five years I have received support and encouragement from a great number of individuals. My advisor Dr. Younan Xia has always been an excellent mentor and exceptional source of suggestions and ideas. His guidance has made my Ph.D. study a thoughtful and rewarding journey. I would like to thank Dr. Stavros Thomopoulos, who has served an advisor-equivalent role during my Ph.D. tenure. His patience and persistence has always inspired me to stick to the aims. I would also like to express my gratitude to Dr. Julie Champion, Dr. Lakeshia Taite, Dr. Andrés García, and Dr. Sven Behrens for serving on my dissertation committee. I am fortunate to have encountered these great people, who are and will always be invaluable assets in my life.

Special thanks go to Dr. Jingwei Xie, who helped me launching into the world of scientific research and generously shared many useful hands-on experiences. I appreciate the input of Justin Lipner, who performed mechanical testing for many of my projects. I am especially grateful for the support and help brought by many of the members in both Xia and Thomopoulos groups: Dr. Xiaoran Li, Dr. Yi-Chun Yeh, Dr. Cionne Manning, Liangzhu Feng, Aleksey Ruditskiy, Shelby Pursley, Nathanael Levinson, Dr. Tianmeng Sun, Dr. Jianhua Zhou, Dr. Lei Zhang, Miaoxin Yang, Dr. Rui Deng, Bo Pang, Dr. Yucai Wang, Dr. Guorong Sun, Dr. Lester Smith, and Ryan Potter, who have made my dissertation work possible. I would also like to thank the administrative staffs at Georgia Tech and Washington University in St. Louis, who facilitated our transition and made it very smooth, Rose Baxter, Janice Whatley-Nwanze, and Denna Cummings, and to the Associate Chair for Graduate Studies in ChBE at the time, Dr. Amyn Teja.

Finally, I would like to express my deepest gratitude to my warm and loving family, especially my parents Xian Liu and Cuiping Ao, for their faith in me. At last, I would like to thank my husband Dr. Yu Shrike Zhang, for his company, love, and encouragement during all these years, and more importantly, perspective for our future.

TABLE OF CONTENTS

LIST OF TABLES

LIST OF FIGURES

LIST OF SYMBOLS AND ABBREVIATIONS

10SBF	10 Times Concentrated Simulated Body Fluid
ANOVA	Analysis of Variance
ALP	Alkaline Phosphatase
ALS	Amyotrophic Lateral Sclerosis
Anti-NCAM	Anti-neural Cell Adhesion Molecules
ASCs	Adipose-derived Mesenchymal Stem Cells
bFGF	Basic Fibroblast Growth Factor
BME	β-Mercaptoethanol
BMP2	Bone Morphogenetic Protein 2
DAPI	4',6-Diamidino-2-phenylindole
DCM	Dichloromethane
DMEM	Dulbecco's Modified Eagle Medium
DMF	Dimethylformaldehyde
DRG	Dorsal Root Ganglia
DSC	Differential Scanning Calorimetry
EBs	Embryoid Bodies
ECM	Extracellular Matrix
EDC	1-Ethyl-dimethylaminopropyl Carbodiimide
EDX	Energy Dispersive X-ray
ESCs	Embryonic Stem Cells
EthD-1	Ethidium Homodimer-1
EtO	Ethylene Oxide
FBS	Fetal Bovine Serum

GFAP	Glial Fibrillary Acidic Protein
HA	Hydroxyapatite
HFIP	Hexafluoro-2-propanol
LIF	Leukemia Inhibitory Factor
m10SBF	Modified 10 Times Concentrated Simulated Body Fluid
microCT	Micro-computed Tomography
MES	2-Morpholinoethane Sulfonic Acid
MSCs	Mesenchymal Stem Cells
MTT	3-(4,5-Dimethylthiazol-2-yl)-2,5-diphenyltetrazolium Bromide
NHS	n-Hydroxysuccinimide
NGS	Normal Goat Serum
OCN	Osteocalcin
PBS	Phosphate-Buffered Saline
P/S	Penicillin-streptomycin
PCL	Poly(ε-caprolactone)
PCNA	Proliferating Cell Nuclear Antigen
PDGF	Platelet-derived Growth Factor
PLA	Poly(Lactic acid)
PLGA	Poly(Lactic-*co*-glycolic) Acid
PVDF	Polyvinylidene Fluoride
ROCK	Rho-associated Protein Kinase
Runx2	Runt-related Transcription Factor 2
SEM	Scanning Electron Microscopy
TCP	Tricalcium Phosphate
TCPS	Tissue Culture Polystyrene

TEM	Transmission Electron Microscopy
TFB	Tendon Fibroblasts
T_g	Glass Transition Temperature
TGF-β	Transforming Growth Factor-beta
T_m	Melting Point
XRD	X-ray Diffraction
α-MEM	α-Minimum Essential Medium

SUMMARY

Electrospun nanofibers represent a class of versatile scaffolds for tissue engineering applications owing to their ability to mimic the nanoscale features of the native extracellular matrix (ECM). In addition, nanofibers produced by electrospinning can be readily collected as uniaxially aligned assemblies to recapitulate the architecture of the ECM in tissues with anisotropic characteristics, such as tendon-to-bone insertions, tendons, and nerves. This dissertation focuses on the design, fabrication, functionalization, and assessment of various types of scaffolds consisting of aligned nanofibers, which can be used to augment regeneration in tissues with anisotropic structures.

Briefly, for tendon-to-bone insertion repair, I assessed the capability of aligned nanofibers with a gradient in mineral content to induce spatially graded osteogenesis of adipose-derived mesenchymal stem cells (ASCs). I also developed an alternative approach to the production of a gradient in the density of osteoblasts. The graded pattern of osteoblasts generated using both approaches could mimic their distribution in the native tendon-to-bone insertion. To further enhance the stiffness of the scaffolds, a new solution was developed to coat the scaffold with a thicker mineral layer. In a third project, a novel method of generating crimp in aligned nanofibers was developed. A solvent plasticizer was employed to release the residual stress retained in the nanofibers during electrospinning, which led to the generation of crimp. Finally, the outgrowth of neurites derived from embryoid bodies (EBs) was studied using aligned nanofibers as the substrates. Depending on the strength of adhesion between nanofibers and neurites, two patterns of outgrowth--parallel and perpendicular (to the alignment)--were observed. Maturation of neurons derived from dissociated EBs was also investigated, as characterized by their extracellular action potential and the ability to form neuromuscular junctions with co-cultured muscle cells.

CHAPTER 1

INTRODUCTION

Many of the tissues in the human body do not possess the ability to regenerate, making the damages to these tissues irreversible [1]. Additionally, injuries to tissues such as nerves, tendons, cartilage, and myocardium also result in significant pain and disability. Even with surgical intervention, return of function is often limited and the healing response is scar-mediated rather than regenerative [2]. More advanced therapies must be developed to promote regeneration and allow the tissues to regain normal function. Regenerative medicine has emerged as an interdisciplinary research field that incorporates biology, material science, and engineering to replace or regenerate human cells, tissues and organs. In regenerative medicine, elements of scaffold design, cellular control, drug delivery, and signaling are often integrated to heal or substitute injured tissues [2-5].

One of the major challenges in regenerative medicine is to design and fabricate a suitable scaffold. Recent advances in biomaterial synthesis and microfabrication have made it possible to pattern cells into complex, three-dimensional structures by using appropriate scaffolds as the templates [6]. With an ever-growing understanding of the intricate interactions between cells and their microenvironment in tissues, more attention is now given to the fabrication of scaffolds capable of recapitulating key features of the ECM that control the migration, proliferation, and differentiation of cells [7]. The ECM is often composed of interwoven protein fibers such as fibrillar collagen and elastin, with diameters ranging from tens to hundreds of nanometers. This matrix also contains nanoscale adhesion proteins that serve as specific binding sites for cell adhesion [8]. Signaling to cells from the ECM occurs by direct interactions between the ligands on the ECM and the receptors on cells, the sequestration of growth factors by the ECM, spatial cues, and mechanical force transduction [8]. As such, the microenvironment provided by

the ECM can control the behavior and fate of a cell [9]. Many techniques have been developed to fabricate fibrous scaffolds for use as ECM substitutes [10]. Among these, electrospinning has recently emerged as one of the most widely used techniques, owning to its ability to generate constructs of fibers similar to the fibrous structures of the native ECM. Figure 1.1 shows some typical examples of tissues in the human body whose regeneration would benefit from the use of nanofiber-based scaffolds [11].

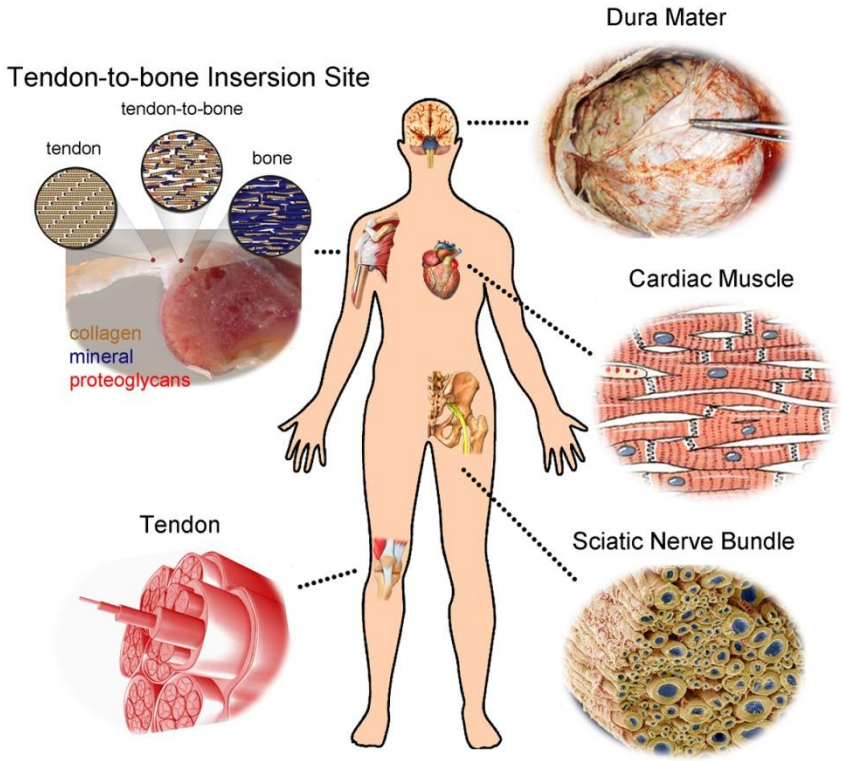

Figure 1.1. *Illustration of some typical examples of tissues in the human body whose regeneration would benefit from the use of nanofiber-based scaffolds.*

1.1 Electrospinning: Set-up and Mechanism

Electrospinning is a remarkably simple, robust, and versatile technique capable of generating fibers with diameters down to the nanoscale [12]. A typical electrospinning set-up, as shown in Figure 1.2A, include four major components [13]: a spinneret (e.g., a hypodermic needle with a blunt-tip), a syringe pump for ejecting the polymer solution at a

controlled rate, a power supply up to 30 kV, and a grounded collector (e.g., a piece of aluminum foil). When the polymer solution emerges from a spinneret, it initially forms a droplet due to the confinement of surface tension. If a high voltage is applied to the spinneret, charges of the same sign will be built on the surface of the droplet. As a result, the droplet will encounter two sets of electrostatic forces, including the repulsion between the surface charges, and the Coulombic force produced by the external electric field [13]. These forces work in combination to distort the droplet into a conical shape commonly known as the Taylor Cone (Figure 1.2A) [14]. Once these forces become sufficiently strong to overcome the surface tension, a liquid jet directed towards the grounded collector will form. The jet will experience both solvent evaporation and whipping instability before it reaches the collector. As a result of stretching by electrostatic repulsion and whipping, the liquid jet will be continuously reduced in size until it has been solidified or deposited on the collector. Conventionally, the as-spun nanofibers are often collected as a randomly oriented, non-woven mat. Figure 1.2B shows a scanning electron microscopy (SEM) image of such a sample.

A non-woven mat of electrospun nanofibers possesses high porosity and spatial interconnectivity well-suited for nutrient and waste transport and cell communication [15]. A scaffold based on electrospun nanofibers also has a large specific surface area for the loading of bioactive molecules to facilitate efficient and selective cellular responses. Electrospinning has been applied to more than 100 different types of polymers [16]. Naturally occurring matrix proteins including collagen, elastin, and fibrinogen and synthetic polymers such as poly(ε-caprolactone) (PCL) and poly(lactic-*co*-glycolic) acid (PLGA) can all be prepared as nanofibers by electrospinning [17]. Since different tissues have distinct criteria for scaffold functionality, having a wide range of materials to choose from allows one to articulate the compositions and other properties of electrospun nanofibers to meet different demands.

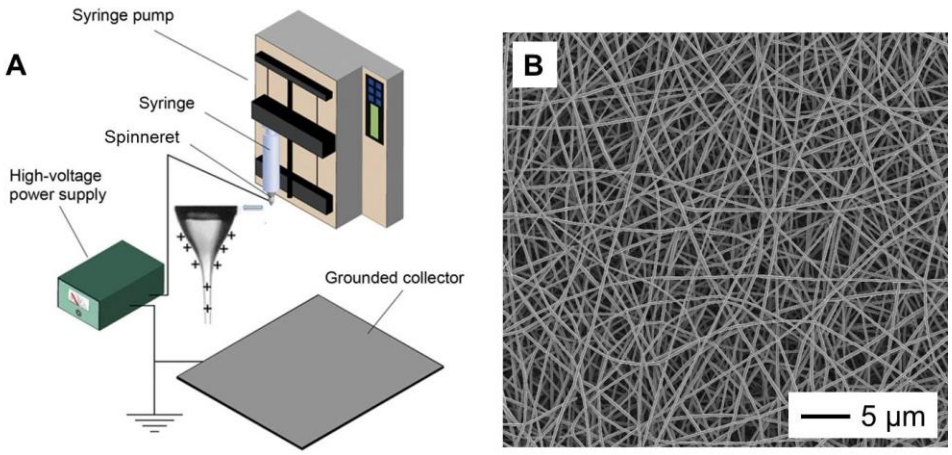

Figure 1.2. *(A) Schematic illustration of the setup for electrospinning. The inset shows a drawing of a typical electrified Taylor Cone. (B) SEM image of randomly oriented PLGA nanofibers collected using the collector in (A).*

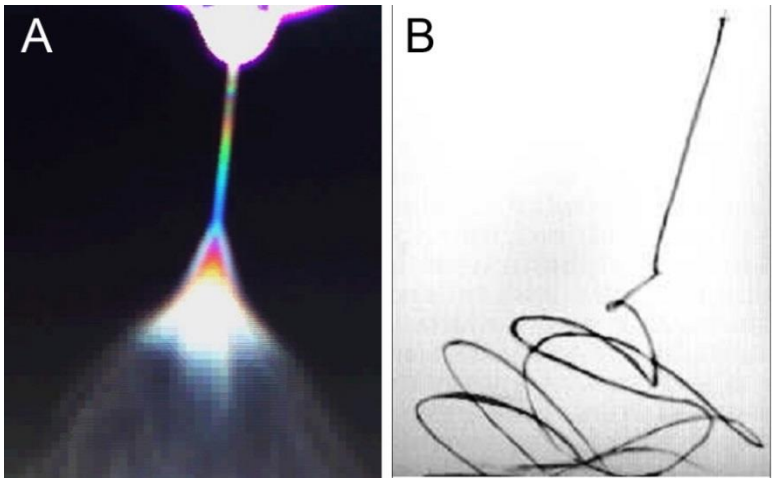

Figure 1.3. *Photographs showing the typical electrospinning jet captured with exposure times of (A) 2 s [18] and (B) 0.1 ms [19].*

Although the setup for electrospinning is very simple, its mechanism can be rather complicated. Prior to 1999, the generation of the ultrathin fibers was attributed to the splitting or splaying of the liquid jet, which was electrified by the external electric field (Figure 1.3A) [12]. Later, a closer examination indicated that the dramatic decrease in size of the liquid jet was mainly a result of the bending instability [14, 20-22]. High-speed

photography was able to capture only one single, rapidly whipping thread, as shown in Figure 1.3B [19]. The shutter speed of conventional photography is more than 1,000 times slower than the frequency of the whipping or bending so that the pictures captured by a conventional camera are composed of numerous overlapped images of the single whipping thread [23].

1.2 Alignment of Electrospun Nanofibers

Many tissues, including the nerve [24], heart [25], tendon [26], and blood vessel [27], have unique anisotropic structures and architectures that cannot be recapitulated by scaffolds fabricated using conventional methods. Electrospinning, in contrast, can be easily used to generate assemblies of aligned nanofibers to mimic the anisotropy of these tissues. In many applications, it is desirable to have a scaffold made of aligned nanofibers, as the anisotropy in topography and structure can greatly affect cell morphology, proliferation, differentiation, and migration [28-33]. Aligned fibrous scaffolds may therefore be useful in replicating the ECM in the aforementioned tissues. A number of methods have been developed for controlling the alignment of electrospun nanofibers. These methods can be categorized into three major categories depending on the type of forces involved (Figure 1.4): mechanical, electrostatic, and magnetic.

In order to align nanofibers using mechanical forces, a metallic rotating mandrel is often used as the collector (Figure 1.4A). When the electrospun nanofibers are collected using a rotating mandrel, the rotating speed of the mandrel determines the degree of alignment of the nanofiber mat. It was shown that random collagen fibers were collected at linear velocity lower than 0.16 m/s, while significant alignment was observed at linear velocities higher than 1.4 m/s [34]. Whereas a higher speed can result in better alignment, a linear velocity higher than 45 m/s will lead to the formation of necks in the nanofibers. At very high rotation speeds, the velocity of the electrospinning jet may be slower than the linear velocity of the mandrel, which may create excessive stress residues and thus necking

in the nanofibers. In order to obtain aligned, uniform nanofibers, it is essential to rotate the mandrel at an appropriate and well-controlled speed [35, 36].

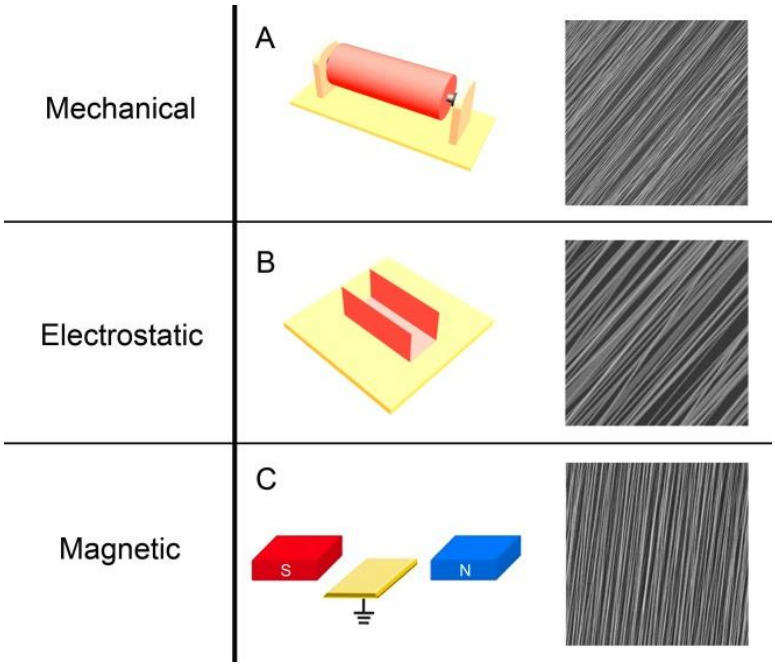

Figure 1.4. *Controlling the alignment of electrospun nanofibers using three different forces: i) mechanical forces through the use of a rotating mandrel (A); ii) electrostatic forces through the use of a metallic staple (B); and iii) magnetic forces through the use of a pair of permanent magnets (C) [37]. The SEM images in the right column show typical morphologies of the aligned nanofibers collected using different methods. The yellow plates are grounded conductive electrodes.*

Nanofibers can also be aligned by electrostatic forces. Since charges are distributed along the electrospinning jet, an external electric field can be used to manipulate and control the alignment of nanofibers. Our group has developed a collector consisting of two pieces of conductive substrates which are separated by a void gap (e.g. a staple collector) to collect uniaxially aligned nanofibers across the gap (Figure 1.4B) [38]. Nanofibers descending from the spinneret will experience two types of electrostatic forces. The

splitting of electric field with electric field lines pointing towards the two electrodes produces the first force, which will pull the fiber towards the electrodes and further induce opposite charges on the surfaces of the electrodes when the fiber travels to their vicinity. This gives rise to a second force, which stretches the nanofiber across the gap to align it perpendicular to the edges of the electrodes. These two types of electrostatic force work together to produce a uniaxially aligned array of nanofibers. If the fibers spanning across the void gap discharge very slowly and repel each other, the extent of alignment will be improved with deposition time [39].

Using an external magnetic field to control the alignment of nanofibers falls into the third category (Figure 1.4C). However, the mechanism for aligning nanofibers electrospun in a magnetic field is rarely investigated. In one study, the researchers found that the magnetic field could assist alignment of electrospun nanofibers, but only when a magnetizable solution was electrospun in a magnetic field [40]. On the contrary, another group concluded that the generation of aligned polymer fibers by magnetic field-assisted electrospinning was independent of the solution and solvent used and did not require the solution to be magnetically active [37]. Although both groups obtained well-aligned nanofibers by applying a magnetic field to electrospinning, their interpretation of the phenomenon was discrepant, indicating that further efforts are needed to investigate the mechanism of alignment for nanofibers electrospun in a magnetic field.

1.3 Scope of This Work

This dissertation focuses on the design, fabrication, functionalization, and assessment of various types of scaffolds consisting of aligned nanofibers for repairing tissues with anisotropic structures. Particular interests were devoted to tendon-to-bone insertion, tendon, and nerve. In addition to mimicking the ECM in these tissues, aligned nanofibers are further modified for better integration with their niche.

In Chapter 2, I first elaborate on how to use aligned nanofibers with a gradient in

mineral content to induce spatially graded osteogenesis of ASCs for tendon-to-bone insertion repair. The insertion connects tendon to bone through gradients in both the composition of ECM and cell phenotypes [41-43]. A scaffold with a gradient in mineral content resembles the gradual increase in mineral content from the tendon side to the bone side of a tendon-to-bone insertion. In order to generate a gradient of osteoblasts that mimics their distribution in the native insertion, this type of scaffolds is utilized to induce graded osteogenesis of ASCs. I also discuss an alternative approach to generating a similar gradient in osteoblasts in Chapter 2. Briefly, a piece of scaffold is inserted into a homogeneous suspension of osteoblasts at a tilted angle. A gradient in cell density can be generated as the cells sediment, because the volume of cell suspension available for sedimentation varies. Both approaches are capable of generating gradients in osteoblasts on aligned nanofibers, which will further the application of aligned nanofibers for repairing the tendon-to-bone insertion.

In Chapter 3, I focus on improving the stiffness at the highly mineralized end of a graded scaffold, which can lead to enhanced osteogenesis of ASCs. For the graded scaffolds, the mineral coating was generated by soaking the nanofibers in a 10 times concentrated simulated body fluid (10SBF) to produce a thin layer of minerals with a large particle size and a flower-like structure [44]. Such coating did not contribute significantly to increasing the stiffness of the scaffold. An alternative solution, the modified 10SBF (m10SBF) [45], is therefore developed to coat the nanofibers with a thick layer of minerals with smaller particle size.

In Chapter 4, I describe a method of generating crimp in aligned nanofibers for tendon tissue engineering. Tendon is a type of highly anisotropic tissue, in which collagen fibrils not only assemble in parallel bundles, but also exhibit a crimped pattern that results in a non-linear stiffening effect with increasing tensile strain to protect the residential fibroblasts from extensive mechanical loading [46-48]. Introducing crimps can reproduce the mechanical characteristics of the native tendon in aligned nanofibers. Crimps in

nanofibers are fabricated by bringing them into contact with their plasticizer. As an example, generation of crimps in poly(lactic acid) (PLA) nanofibers using ethanol is demonstrated.

In Chapter 5, I discuss the potential of using aligned nanofibers as a platform to regulate the outgrowth of neurites derived from embryonic stem cells (ESCs) and their maturation into motoneurons. The therapeutic effect of delivering ESCs to the injured nervous system has been extensively investigated [49-51]. However, functional recovery still remains to be challenging. One potential reason lies in the fact that the neurites derived from these ESCs are sprouting haphazardly without appropriate guidance. The capability of aligned nanofibers to direct the extension of neurites along the alignment has been previously demonstrated by several research groups [52-54]. My observations, however, reveal that the neurites could also be guided to project in the direction perpendicular to the alignment. Preliminary investigation of the mechanism underlying perpendicular outgrowth is presented, along with the characterization of the maturation of neurons derived from ESCs.

1.4 References

[1] Badylak, S. F.; Taylor, D.; Uygun, K. Whole-organ tissue engineering: Decellularization and recellularization of three-dimensional matrix scaffolds. *Annu. Rev. Biomed. Eng.* **2011**, *13*, 27-53.

[2] Vacanti, J. P.; Langer, R. Tissue engineering: The design and fabrication of living replacement devices for surgical reconstruction and transplantation. *Lancet* **1999**, *354*, S32-S34.

[3] Badylak, S. F.; Nerem, R. M. Progress in tissue engineering and regenerative medicine. *Proc. Natl. Acad. Sci. USA* **2010**, *107*, 3285-3286.

[4] Khademhosseini, A.; Vacanti, J. P.; Langer, R. Progress in tissue engineering. *Sci. Am.* **2009**, *300*, 64-71.

[5] Freed, L. E.; Vunjak-Novakovic, G.; Biron, R. J.; Eagles, D. B.; Lesnoy, D. C.; Barlow, S. K.; Langer, R. Biodegradable polymer scaffolds for tissue engineering. *Nat. Biotechnol.* **1994**, *12*, 689-693.

[6] Kelleher, C. M.; Vacanti, J. P. Engineering extracellular matrix through nanotechnology. *J. R. Soc. Interface* **2010**, *7*, S717-S729.

[7] Dvir, T.; Timko, B. P.; Kohane, D. S.; Langer, R. Nanotechnological strategies for engineering complex tissues. *Nat. Nanotechol.* **2011**, *6*, 13-22.

[8] Prestwich, G. D. Simplifying the extracellular matrix for 3D cell culture and tissue engineering: A pragmatic approach. *J. Cell. Biochem.* **2007**, *101*, 1370-1383.

[9] Lutolf, M. P.; Gilbert, P. M.; Blau, H. M. Designing materials to direct stem-cell fate. *Nature* **2009**, *462*, 433-441.

[10] Madurantakam, P. A.; Cost, C. P.; Simpson, D. G.; Bowlin, G. L. Science of nanofibrous scaffold fabrication: Strategies for next generation tissue-engineering scaffolds. *Nanomedicine* **2009**, *4*, 193-206.

[11] Liu, W.; Thomopoulos, S.; Xia, Y. Electrospun nanofibers for regenerative medicine. *Adv. Healthcare Mater.* **2012**, *1*, 10-25.

[12] Reneker, D. H.; Chun, I. Nanometre diameter fibres of polymer, produced by electrospinning. *Nanotechnol.* **1996**, *7*, 216-223.

[13] Li, D.; Xia, Y. Electrospinning of nanofibers: Reinventing the wheel? *Adv. Mater.* **2004**, *16*, 1151-1170.

[14] Yarin, A.; Koombhongse, S.; Reneker, D. Taylor cone and jetting from liquid droplets in electrospinning of nanofibers. *J. Appl. Phys.* **2001**, *90*, 4836-4846.

[15] Pham, Q. P.; Sharma, U.; Mikos, A. G. Electrospinning of polymeric nanofibers for tissue engineering applications: A review. *Tissue Eng.* **2006**, *12*, 1197-1211.

[16] Agarwal, S.; Wendorff, J. H.; Greiner, A. Progress in the field of electrospinning for tissue engineering applications. *Adv. Mater.* **2009**, *21*, 3343-3351.

[17] Frenot, A.; Chronakis, I. S. Polymer nanofibers assembled by electrospinning. *Curr. Opin. Coll. Interface Sci.* **2003**, *8*, 64-75.

[18] Reneker, D. H.; Yarin, A. L. Electrospinning jets and polymer nanofibers. *Polymer* **2008**, *49*, 2387-2425.

[19] Kowalewski, T. A.; Błonski, S.; Barral, S. Experiments and modeling of electrospinning process. *Bull. Pol. Acad. Sci. Tech. Sci.* **2005**, *53*, 385-394.

[20] Reneker, D. H.; Yarin, A. L.; Fong, H.; Koombhongse, S. Bending instability of electrically charged liquid jets of polymer solutions in electrospinning. *J. Appl. Phys.* **2000**, *87*, 4531-4547.

[21] Shin, Y.; Hohman, M.; Brenner, M.; Rutledge, G. Electrospinning: A whipping fluid jet generates submicron polymer fibers. *Appl. Rhys. Lett.* **2001**, *78*, 1149-1151.

[22] Shin, Y.; Hohman, M.; Brenner, M.; Rutledge, G. Experimental characterization of electrospinning: The electrically forced jet and instabilities. *Polymer* **2001**, *42*, 09955-09967.

[23] Theron, S. A.; Zussman, E.; Yarin, A. L. Experimental investigation of the governing parameters in the electrospinning of polymer solutions. Polymer **2004**, *45*, 2017-2030.

[24] Schnell, E.; Klinkhammer, K.; Balzer, S.; Brook, G.; Klee, D.; Dalton, P.; Mey, J. Guidance of glial cell migration and axonal growth on electrospun nanofibers of poly(ε-caprolactone) and a collagen/poly(ε-caprolactone) blend. *Biomaterials* **2007**, *28*, 3012-3025.

[25] Zong, X.; Bien, H.; Chung, C.-Y.; Yin, L.; Fang, D.; Hsiao, B. S.; Chu, B.; Entcheva, E. Electrospun fine-textured scaffolds for heart tissue constructs. *Biomaterials* **2005**, *26*, 5330-5338.

[26] Yin, Z.; Chen, X.; Chen, J. L.; Shen, W. L.; Hieu Nguyen, T. M.; Gao, L.; Ouyang, H. W. The regulation of tendon stem cell differentiation by the alignment of nanofibers. *Biomaterials* **2010**, *31*, 2163-2175.

[27] Lu, H.; Feng, Z.; Gu, Z.; Liu, C. Growth of outgrowth endothelial cells on aligned PLLA nanofibrous scaffolds. *J. Mater. Sci. Mater. Med.* **2009**, *20*, 1937-1944.

[28] Mo, X.; Xu, C.; Kotaki, M. E. A.; Ramakrishna, S. Electrospun poly(LLA-CL) nanofiber: A biomimetic extracellular matrix for smooth muscle cell and endothelial cell proliferation. *Biomaterials* **2004**, *25*, 1883-1890.

[29] Silva, G. A.; Czeisler, C.; Niece, K. L.; Beniash, E.; Harrington, D. A.; Kessler, J. A.; Stupp, S. I. Selective differentiation of neural progenitor cells by high-epitope density nanofibers. *Science* **2004**, *303*, 1352-1355.

[30] Xin, X.; Hussain, M.; Mao, J. J. Continuing differentiation of human mesenchymal stem cells and induced chondrogenic and osteogenic lineages in electrospun PLGA nanofiber scaffold. *Biomaterials* **2007**, *28*, 316-325.

[31] Xie, J.; Li, X.; Xia, Y. Putting electrospun nanofibers to work for biomedical research. *Macromol. Rapid Comm.* **2008**, *29*, 1775-1792.

[32] Sill, T. J.; von Recum, H. A. Electrospinning: Applications in drug delivery and tissue engineering. *Biomaterials* **2008**, *29*, 1989-2006.

[33] Xie, J.; MacEwan, M. R.; Ray, W. Z.; Liu, W.; Siewe, D. Y.; Xia, Y. Radially aligned, electrospun nanofibers as dural substitutes for wound closure and tissue regeneration applications. *ACS Nano* **2010**, *4*, 5027-5036.

[34] Matthews, J. A.; Wnek, G. E.; Simpson, D. G.; Bowlin, G. L. Electrospinning of collagen nanofibers. *Biomacromol.* **2002**, *3*, 232-238.

[35] Teo, W.; Ramakrishna, S. A review on electrospinning design and nanofibre assemblies. *Nanotechnol.* **2006**, *17*, R89.

[36] Barnes, C. P.; Sell, S. A.; Boland, E. D.; Simpson, D. G.; Bowlin, G. L. Nanofiber technology: Designing the next generation of tissue engineering scaffolds. *Adv. Drug Deliver. Rev.* **2007**, *59*, 1413-1433.

[37] Liu, Y.; Zhang, X.; Xia, Y.; Yang, H. Magnetic-field-assisted electrospinning of aligned straight and wavy polymeric nanofibers. *Adv. Mater.* **2010**, *22*, 2454-2457.

[38] Li, D.; Wang, Y.; Xia, Y. Electrospinning of polymeric and ceramic nanofibers as uniaxially aligned arrays. *Nano Lett.* **2003**, *3*, 1167-1171.

[39] Li, D.; Wang, Y.; Xia, Y. Electrospinning nanofibers as uniaxially aligned arrays and layer-by-layer stacked films. *Adv. Mater.* **2004**, *16*, 361-366.

[40] Yang, D.; Lu, B.; Zhao, Y.; Jiang, X. Fabrication of aligned fibrous arrays by magnetic electrospinning. *Adv. Mater.* **2007**, *19*, 3702-3706.

[41] Thomopoulos, S.; Williams, G.; Soslowsky, L. Tendon to bone healing: Differences in biomechanical, structural, and compositional properties due to a range of activity levels. *J. Biomech. Eng.* **2003**, *125*, 106-113.

[42] Thomopoulos, S.; Williams, G. R.; Gimbel, J. A.; Favata, M.; Soslowsky, L. J. Variation of biomechanical, structural, and compositional properties along the tendon to bone insertion site. *J. Orthop. Res.* **2003**, *21*, 413-419.

[43] Thomopoulos, S.; Genin, G. M.; Galatz, L. M. The development and morphogenesis of the tendon-to-bone insertion what development can teach us about healing. *J. Musculoskelet. Neuro. Interactions* **2010**, *10*, 35.

[44] Li, X.; Xie, J.; Lipner, J.; Yuan, X.; Thomopoulos, S.; Xia, Y. Nanofiber scaffolds with gradations in mineral content for mimicking the tendon-to-bone insertion site. *Nano Lett.* **2009**, *9*, 2763-2768.

[45] Liu, W.; Yeh, Y.-C.; Lipner, J.; Xie, J.; Sung, H.-W.; Thomopoulos, S.; Xia, Y. Enhancing the stiffness of electrospun nanofiber scaffolds with a controlled surface coating and mineralization. *Langmuir* **2011**, *27*, 9088-9093.

[46] Kastelic, J.; Galeski, A.; Baer, E. The multicomposite structure of tendon. *Connect. Tissue Res.* **1978**, *6*, 11-23.

[47] Kastelic, J.; Palley, I.; Baer, E. A structural mechanical model for tendon crimping. *J. Biomech.* **1980**, *13*, 887-893.

[48] Franchi, M.; Trirè, A.; Quaranta, M.; Orsini, E.; Ottani, V. Collagen structure of tendon relates to function. *Sci. World J.* **2007**, *7*, 404-420.

[49] Cui, L.; Jiang, J.; Wei, L.; Zhou, X.; Fraser, J. L.; Snider, B. J.; Yu, S. P. Transplantation of embryonic stem cells improves nerve repair and functional recovery after severe sciatic nerve axotomy in rats. *Stem Cells* **2008**, *26*, 1356-1365.

[50] McDonald, J. W.; Liu, X.-Z.; Qu, Y.; Liu, S.; Mickey, S. K.; Turetsky, D.; Gottlieb, D. I.; Choi, D. W. Transplanted embryonic stem cells survive, differentiate and promote recovery in injured rat spinal cord. *Nat. Med.* **1999**, *5*, 1410-1412.

[51] Keirstead, H. S.; Nistor, G.; Bernal, G.; Totoiu, M.; Cloutier, F.; Sharp, K.; Steward, O. Human embryonic stem cell-derived oligodendrocyte progenitor cell transplants remyelinate and restore locomotion after spinal cord injury. *J. Neurosci.* **2005**, *25*, 4694-4705.

[52] Xie, J.; MacEwan, M. R.; Schwartz, A. G.; Xia, Y. Electrospun nanofibers for neural tissue engineering. *Nanoscale* **2010**, *2*, 35-44.

[53] Xie, J.; MacEwan, M. R.; Willerth, S. M.; Li, X.; Moran, D. W.; Sakiyama-Elbert, S. E.; Xia, Y. Conductive core-sheath nanofibers and their potential application in neural tissue engineering. *Adv. Funct. Mater.* **2009**, *19*, 2312-2318.

[54] Xie, J.; Liu, W.; MacEwan, M. R.; Bridgman, P. C.; Xia, Y. Neurite outgrowth on electrospun nanofibers with uniaxial alignment: The effects of fiber density, surface coating, and supporting substrate. *ACS Nano* **2014**, *8*, 1878-1885.

CHAPTER 2

GENERATION OF CONTUNUOUS GRADIENT IN CELL PHENOTYPES FOR TENDON-TO-BONE INSERTION REPAIR

2.1 Introduction

Tendon-to-bone insertion is a functionally graded transitional tissue, with spatial variations in structural organization, cell phenotype, and ECM composition [1-6]. As shown in Figure 1.1, up left, the orientation of collagen fibrils in the insertion gradually transitions from highly organized in the tendon to less organized in the bone. Aligned nanofibers mimic the overal anisotropy in the insertion, and can therefore be used as a scaffold for tendont-to-bone insertion repair. In addition to structural organization, there exists a gradient in phenotypes for the cells residing in enthesis. While tendon is populated by tendon fibroblasts (TFBs), the bone is populated by osteoblasts, osteocytes, and osteoclasts [5]. A increasing gradient of osteoblasts and a decreasing gradient of TFBs from the tendon side to the bone side are observed at the insertion. These gradients in cell phenotypes cannot be recreated after injury [4, 6]. Approaches to generating gradients in cell phenotypes on aligned nanofibers need to be developed, in order to promote healing in tendon-to-bone insertion.

In this chapter, two approaches were developed to generate gradients in cell phenotypes. In the first approach, a scaffold with a gradation in mineral content was developed in order to mimic the compositional transition in the ECM of the enthesis. The hypothesis is that the relevant stem cells seeded onto such a scaffold will respond to the minerals in a graded fashion, thus achieving a gradient in cell phenotype. Our group previously developed a simple method for fabricating nanofibers scaffolds with gradients in mineral content [7]. In the previous study, 10SBF was gradually added into a glass vial containing the electrospun nanofiber scaffold placed at a tilted angle. A gradient in mineral

content was formed due to the longer immersion time at the lower portions of the scaffolds in the coating solution. As a follow-up study, I investigated the differentiation of ASCs on such graded scaffolds. ASCs have a number of advantages over other sources of mesenchymal stem cells for: *i)* they can be harvested using minimally invasive procedures; *ii)* they are available in abundant quantities; *iii)* they possess the ability to differentiate into multiple mesenchymal lineages, and *iv)* they display immunosuppressive capabilities [8-12].

In the second approach, I directly seeded tendon fibroblasts and osteoblasts onto a scaffold in a graded fashion, with opposite cell density profiles along the length of the scafold, in an effort to mimic the distribution of cell phenotype in enthesis. Briefly, a nanofiber scaffold was inserted into a homogeous suspension of cells at a tilted angle. A gradient in cell density formed after the cells sedimented, because the number of cells available for sedimentation above the scaffold varied. The second phenotype of cells can be seeded in a separate sedimentation procedure, with the scaffold rotated horizontally by 180 degrees prior to cell seeding. Both approaches were able to generate gradients in cell phenotypes, and may be used in combination with aligned nanofibers for repairing the tendon-to-bone insertion [13, 14].

2.2 Inducing Graded Osteogenesis of ASCs *in vitro*

The goal of this study was to induce spatially controlled osteogenesis of ASCs using a nanofiber scaffold with graded mineral coatings. The gradient in mineral content led to a gradient in local modulus for the scaffold [7]. Since stem cells respond to both the stiffness and composition of the substrate, I hypothesized that ASC osteogenesis would be positively correlated to the mineral content.

2.2.1 Fabrication of Nanofiber Scaffolds with Spatial Gradients in Mineral Content

Figure 2.1 shows a schematic of the approach to generating a graded coating of calcium phosphate on a nonwoven mat of electrospun nanofibers. Since the amount of mineral deposited on the nanofiber scaffold is directly proportional to the immersion time in the coating solution, a mineral gradient can be generated by gradually adding the coating solution into the beaker.

Figure 2.1. *Photography of the set-up used for fabricating a nanofiber scaffold with a gradient in mineral content. As the 10SBF being added into the beaker, the minerals were gradually deposited on the nanofiber scaffold that was immersed in the solution. As the level of the solution rose, a gradient in mineral content would form due to the difference in immersion time among different locations on the scaffold.*

In the present study, the gradient was achieved by adding the mineralization solution at a constant rate into a beaker containing the scaffold (supported on a substrate) in a tilted angle. The shape of scaffold is rectangular, with the nanofibers aligning in the longitudinal direction. To improve the hydrophilicity of the nanofibers and activate their

surfaces for calcium phosphate deposition, the scaffold was treated with air plasma first. For the mineralization solution, I used a 10SBF, in which the concentrations of calcium and phosphate ions were ten times of those found in human plasma. Rapid deposition of minerals (within a period of 2-6 h) was achieved by mixing the 10SBF with $NaHCO_3$ [15].

Figure 2.2 shows SEM images of uniaxially aligned PLGA nanofibers covered with a graded mineral coating. The longitidinal position along the scaffold was registered to the interface set by air and the 10SBF solution, which corresponded to d=0. The images shown here were taken from the scaffolds at positions of d=1, 2, 3, and 5 cm. The density and thickness of the mineral coating increased gradually from d=1 cm to d=5 cm.

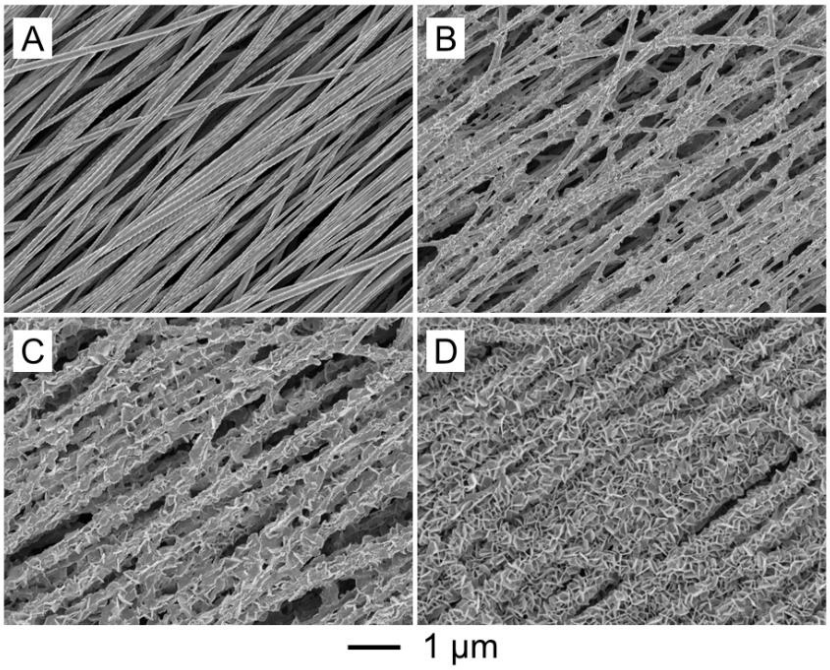

Figure 2.2. *SEM images of calcium phosphate coatings on a plasma-treated non-woven mat of PLGA nanofibers at d= (A) 1, (B) 2, (C) 3, and (D) 5 cm.*

The relative amount of mineral was determined by energy dispersive X-ray (EDX) measurements. As shown in Figure 2.3, the atomic Ca/(Ca+C) ratio changed from ~2% to ~50% over the distance of 5 cm along the scaffold. Five locations along the long axis of

each scaffold were analyzed for the experiments described below. Locations 1 and 5 were chosen to represent the unmineralized and fully mineralized regions, respectively, whereas locations 2-4 were chosen from the central portion of the scaffold, as indicated in Figure 2.3. The Ca/(Ca+C)% for location 2, 3, and 4 were 12.8%, 25.3%, and 37.9%, respectively.

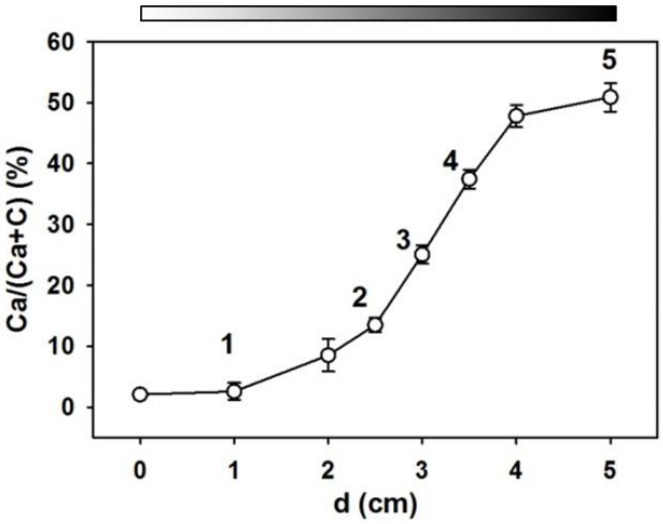

Figure 2.3. *EDX analysis of the gradient in mineral content (N=3). The mineral content increased monotonically along the 5 cm length of the scaffold. The grayscale legend above the plot shows the gradient in mineral content, with the highest mineral level shown in black.*

2.2.2 Viability of ASCs on Nanofiber Scaffolds with Graded Mineral Coating

In order to investigate the response of ASCs to the mineral gradients on the scaffolds, cells were cultured on the scaffolds in the presence of proliferation medium for 2 h, 7 day, 14 day, and 28 day. Cell viability was visualized by live/dead staining at the end of each time period. The first column in Figure 2.4 shows that ASCs were distributed homogeneously on the scaffolds and remained highly viable 2 h post initial seeding. The ASCs successfully adhered to the scaffolds and cell density increased with prolonged duration of incubation time. The ASCs maintained high viability at all locations on the scaffolds regardless of mineral content.

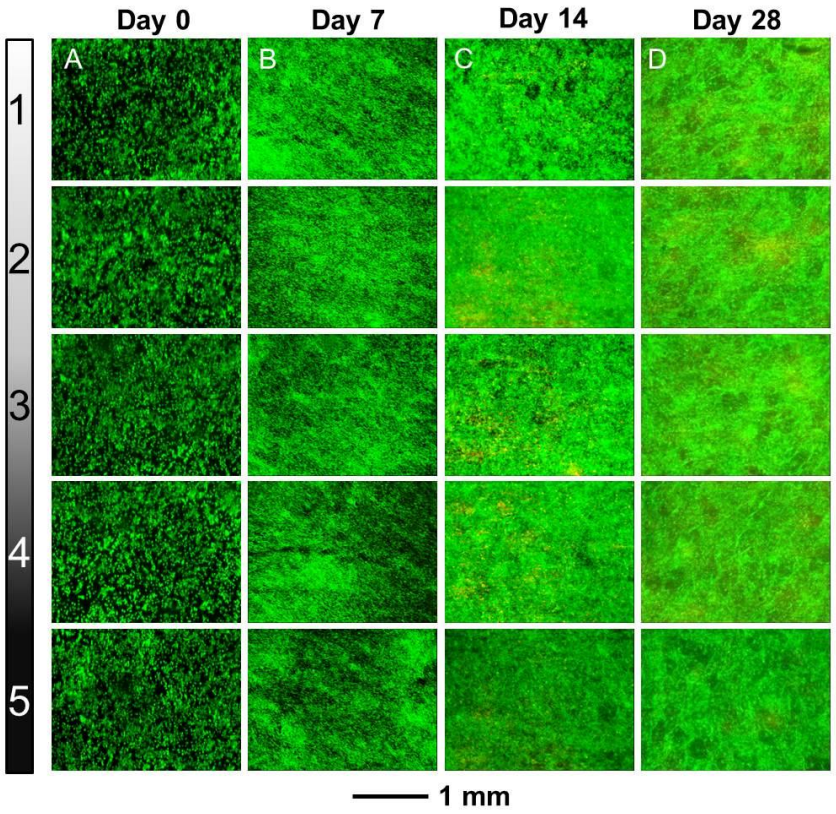

Figure 2.4. *Live/Dead staining of ASCs seeded on aligned nanofibers with a spatial gradient in mineral content (locations 1-5) after incubation for (A) 2 h, (B) 7 days, (C) 14 days, and (D) 28 days. Cells remained viable through the culture period, with few apparent dead cells (red).*

To visualize proliferative activity in the ASCs, I performed proliferating cell nuclear antigen (PCNA) staining for the cells after 7 and 14 days of culture (Figure 2.5). PCNA staining was negatively correlated with mineral content. For the proliferative group at day 7, ~95% of the ASCs at location 1 (no mineral) maintained their proliferative status, whereas only ~50% of the cells at location 5 (the highest in mineral content) were proliferative (Figure 2.5, A–C). At day 14, although the cell density remained relatively unchanged, almost all of the ASCs at location 5 were negative for PCNA staining (Figure 2.5, D–E).

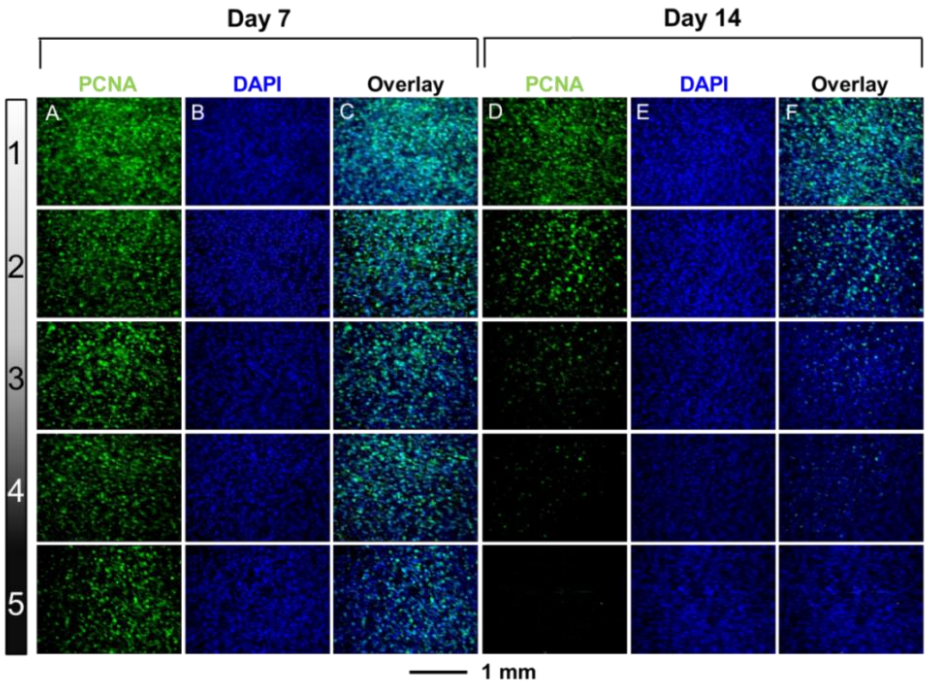

Figure 2.5. *PCNA staining of ASCs seeded on aligned nanofibers with a spatial mineral gradient after culture for (columns A–C) 7 days and (columns D–F) 14 days. (A, D) PCNA staining of ASCs on day 7 and 14, respectively. (B, E) DAPI staining of ASCs on day 7 and 14, respectively. (C) Superimposed images of (A) and (B). (F) Superimposed images of (D) and (E). Cellular density (as visualized with DAPI) was similar from location 1-5 on the scaffold and over time. PCNA staining was negatively correlated with the mineral content.*

I further conducted 3-(4,5-dimethylthiazol-2-yl)-2,5-diphenyltetrazolium Bromide (MTT) assay to analyze the response of ASCs to the scaffold. During the initial seeding process, ASCs were distributed homogeneously on the scaffolds, with similar cell densities on all samples. Figure 2.6 shows the absorbance of formazan crystals (dissolved in *iso*-propanol) metabolized from MTT by live ASCs. The set of columns for day 1 had similar values of absorbance, indicating comparable cell densities across the entire length of each scaffold. However, a gradient in cell density, negatively correlated with the mineral content, began to appear at day 7 and became more prominent with increasing culture time. Specifically, the cell density was the lowest at location 5 (corresponding to the location

with the highest mineral content) and the highest at location 1 (corresponding to the location with no mineral) for each scaffold. Both factors (culture time and location) contributed significantly to these differences in absorbance ($p<0.05$).

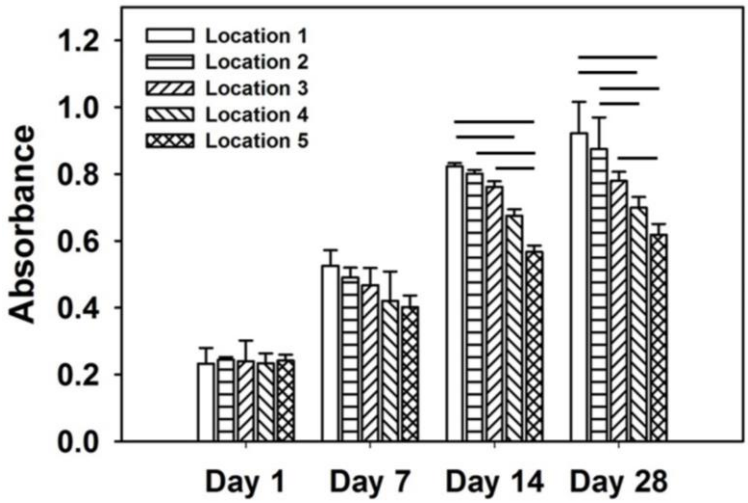

Figure 2.6. *Quantification of cell proliferation on aligned nanofibers with a graded mineral coating for 1, 7, 14, and 28 days. The data were obtained using the MTT assay. Proliferation was negatively correlated with mineral content.*

2.2.3 Osteogenesis of ASCs on Nanofiber Scaffolds with Graded Mineral Coating

Osteogenesis of ASCs was evaluated at day 7, 14, and 28 after seeding. Alkaline phosphatase (ALP) is an enzyme that is highly expressed in bone cells, which interacts with organic phosphates present in tissue fluids, leading to the accumulation of inorganic phosphate necessary for mineralization. This phosphate binds to locally present calcium ions to generate calcium phosphate crystals and stimulate bone formation [16]. Therefore, ALP is commonly used as an early marker of osteogenesis [17, 18].

Images of the localized staining of ALP can be found in Figure 2.7. There was an increase in ALP expression by ASCs over time, which was positively correlated with mineral content.

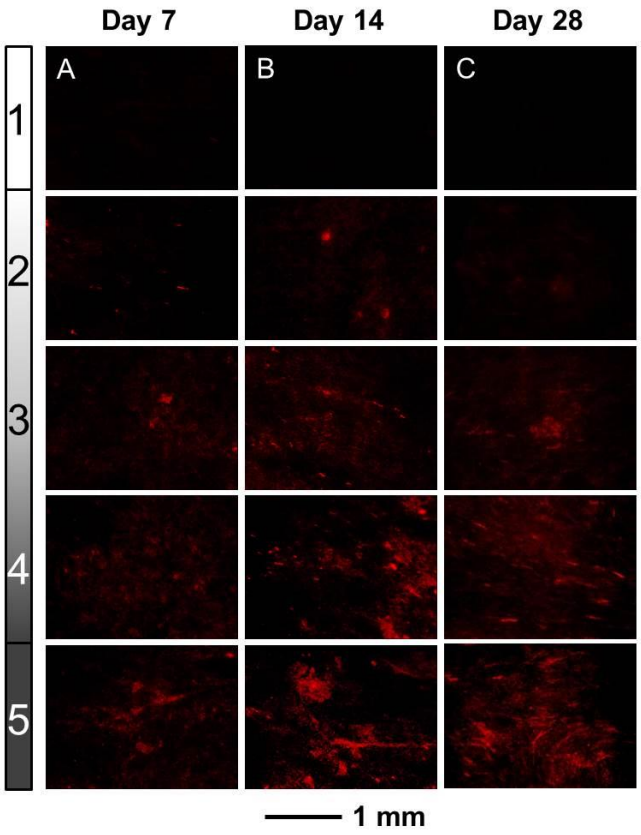

Figure 2.7. *ALP staining of ASCs seeded on aligned nanofibers with a spatial gradient in mineral after (A) 7, (B) 14, and (C) 28 d. There was an increase in ALP expression by ASCs over time and this expression was positively associated with mineral content.*

Quantification of ALP activity was performed by assessing the mean pixel intensity of images using the software Image J. The intensities of ALP activities at different locations are shown in Figure 2.8. There were significant effects ($p<0.05$) on ALP activity from the factor of location (*i.e.*, mineral content), culture time, and culture medium at all of the time points except for day 1. This analysis supported the staining results: *i*) there was a positive correlation between ALP activity and spatial location (*i.e.*, mineral content), *ii*) ALP activity increased with culture time. Statistically, there was a significant effect of location (mineral content) on ALP activity ($p<0.05$).

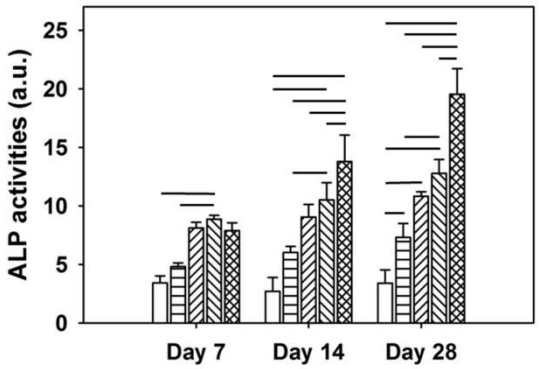

Figure 2.8. *Quantification of ALP activity of ASCs seeded on aligned nanofibers with a graded mineral coating for 7, 14 and 28 d. There was an increase in ALP expression by ASCs over time and this expression was positively correlated with mineral content. Significance indicated by lines over the bars.*

To further evaluate osteogenesis on the graded scaffolds, immunocytochemistry was performed for runt-related transcription factor 2 (Runx2) (an early marker of osteoblast differentiation) and osteocalcin (OCN) (a late marker of osteoblast differentiation). Runx2 is an essential early transcription factor that drives mesenchymal stem cells (MSCs) toward osteoblast differentiation [19-22]. For instance, Runx2-deficient mice lack bone formation due to the absence of osteoblasts [23]. Results from Runx2 staining at day 14 and 28 are shown in Figure 2.9. Runx2 staining was positively correlated with mineral content, and increased with culture time. Co-localization of Runx2 and 4',6-diamidino-2-phenylindole (DAPI) staining confirmed that Runx2 staining was localized to the cell nuclei (Figure 2.10).

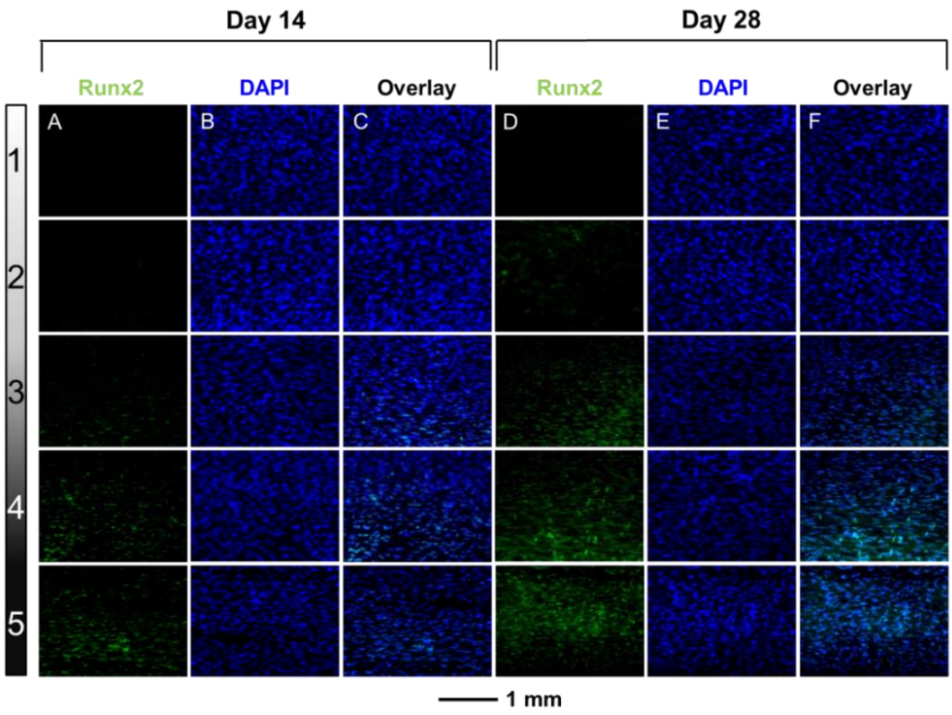

Figure 2.9. *Runx2 staining of ASCs seeded on aligned nanofibers with a spatial mineral gradient after culture for (A-C) 14 and (D-F) 28 days. (A, D) Runx2 staining of ASCs on day 14 and 28, respectively. (B, E) DAPI staining of ASCs on day 14 and 28, respectively. (C) Superimposed images of (A) and (B). (F) Superimposed images of (D) and (E). Runx2 staining was positively correlated with increasing mineral content and increased with culture time.*

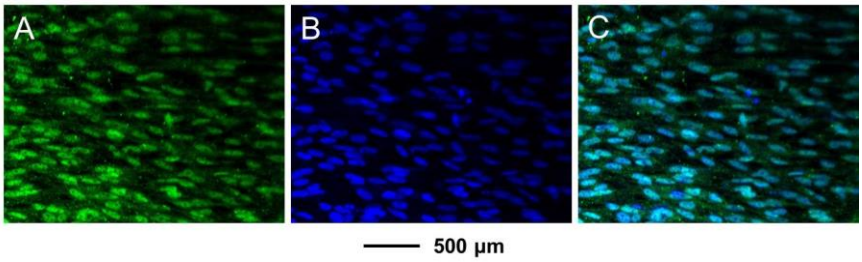

Figure 2.10. *Representative high-magnification images of Runx2 and DAPI staining of ASCs cultured on a nanofiber scaffold with a spatial gradient in mineral content. Runx2 expression was localized to cell nuclei.*

OCN is a non-collagenous protein found in the ECM of bones and is involved in regulating mineralization [24, 25]. OCN is a specific marker of osteoblasts and is therefore a useful marker for the late stages of osteogenesis [26]. No expression of OCN was detected at day 7. No positive staining could be found at locations 1–4 at day 14, while some positive staining was evident at location 5 (Figure 2.11, columns A–C). At day 28, in addition to location 5, OCN was observed at locations 3 and 4 (Figure 2.11, columns D–F). In general, the level of OCN expression was positively correlated with mineral content along the length of the scaffold. Figure 2.12 shows images of OCN expression at a higher magnification, demonstrating its localization to the ECM.

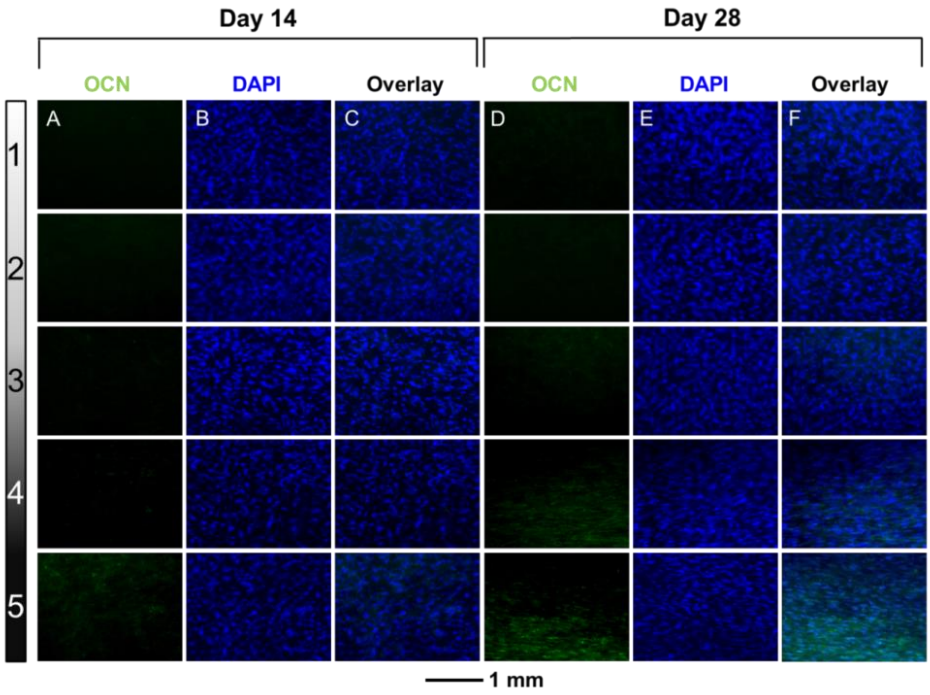

Figure 2.11. *OCN staining of ASCs seeded on aligned nanofibers with a spatial mineral gradient after culture for (A-C) 14 and (D-F) 28 days. (A, D) OCN staining of ASCs on day 14 and 28, respectively. (B, E) DAPI staining of ASCs on day 14 and 28, respectively. (C) Superimposed images of (A) and (B). (F) Superimposed images of (D) and (E). OCN staining was positively correlated with increasing mineral content and increased with culture time.*

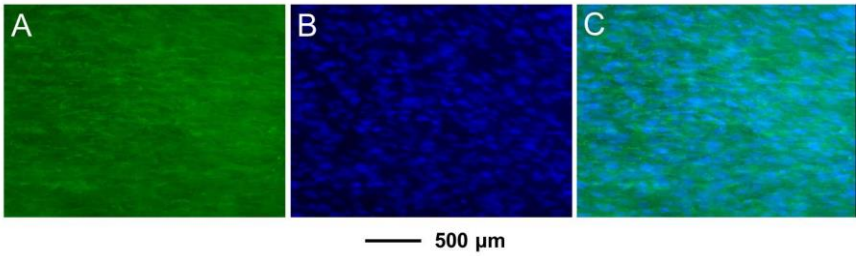

Figure 2.12. *Representative high-magnification images of OCN and DAPI staining of ASCs cultured on a nanofiber scaffold with a spatial gradient in mineral content. OCN was localized to the ECM.*

ASCs demontrated either proliferative or differentiated phenotypes, depending on the local mineral content and culture time. The fate of the ASCs was controlled by both compositional cues and scaffold stiffness. Although cells were evenly distributed on scaffolds at the time of seeding, increased culture time resulted in more cells being present on the bare fibers than those mineralized. These differences in cell distribution became more prominent over time. This was consistent with the PCNA results, which showed that ASC proliferation was negatively correlated with the mineral content. Under the proliferation condition (*i.e.*, in medium lacking osteogenic factors), the mineral content was sufficient to encourage ASCs towards osteogenic differentiation. At day 14, almost no cells exhibited positive PCNA staining at location 5, whereas ALP, Runx2, and OCN were highly expressed, indicating a shift from proliferation to differentiation that was correlated with the mineral content. Live/dead staining showed very few dead cells at any location on the scaffold, further supporting the interpretation that ASCs shifted from proliferation to differentiation after 14 days of culture due to the presence of mineral coating. These results are consistent with reports by others. For example, Triffitt *et al.* found that the proliferation of MSCs was reduced on mineral surfaces compared to plastics, while differentiation was enhanced by the presence of mineral [27]. Missirlis *et al.* reported lower proliferation and higher ALP activity for MSCs on hydroxyapatite (HA) than on culture plastics [28].

Nevertheless, contrasting results have also been reported by several groups. For example, Mooney *et al.* observed that MSCs grew faster on mineralized substrates, when compared to tissue culture plastics, whereas osteogenesis was inhibited by the presence of minerals [29]. This apparent contradiction may be explained by the differences in the type and morphology of minerals among the various studies. While HA promotes osteogenesis in most cases, tricalcium phosphate (TCP) can inhibit osteogenesis due to its low crystallinity, small crystal size, high surface roughness, and rapid dissolution rate relative to HA [30-33]. My obervations are consistent with the literature in that the mineral in the current study was primarily HA [34].

Osteogenesis of ASCs increased gradually from location 1 to 5 on the graded scaffolds. ASCs showed no signs of osteogenesis on the unmineralized portion of the scaffold, demonstrated an osteoprogenitor phenotype in the center of the scaffolds, and displayed an osteoblast phenotype on the fully mineralized portion of the scaffolds. These trends were reinforced with increasing culture time. Runx2 and OCN were chosen as representative early and late immunocytochemistry markers of osteogenesis, respectively [18, 25]. Runx2 is a transcription factor necessary for early differentiation of MSCs into osteoprogenitors [19]. In contrast, OCN is primarily secreted by mature osteoblasts and osteocytes, and is therefore a marker of mature bone cells [26]. A relatively large number of osteoprogenitor cells were evident at locations 4 and 5 by day 28, while only a moderate number of mature osteoblasts were present at this time point. HA mineral is considered osteoconductive based on its capacity to promote osteogensis both *in vitro* and *in vivo* [35-37]. Huang *et al.* showed that both ALP activity and OCN expression of MSCs increased due to the introduction of HA into nanofibrous scaffolds [38]. Ramakrishna *et al.* electrosprayed HA onto electrospun nanofibers to enhance MSC differentiation [39]. The same group also precipitated HA onto electrospun nanofibers to induce the osteogenesis of ASCs [40]. Positive staining for both CD105 (an ASC-specific marker) and OCN showed that ASCs were undergoing osteogenesis due to the influence of HA. These and other

results confirmed that polymer/mineral composite substrates can enhance the differentiation of MSCs by encouraging osteogenesis [41].

2.3 Generation of Controllable Gradient in Cell Density

In this work, I developed a simple and versatile method for generating gradients in cell density. It involved the insertion of a substrate into a homogeneous suspension of cells at a tilted angle (Figure 2.13). I hypothesized that, due to the varying volumes of cell suspension above the substrate, the number of cells available for sedimentation onto the substrate would vary along the direction of insertion, naturally leading to the establishment of a gradient in cell density on the substrate. Different gradients in cell density could be obtained by altering the tilted angle of the substrate.

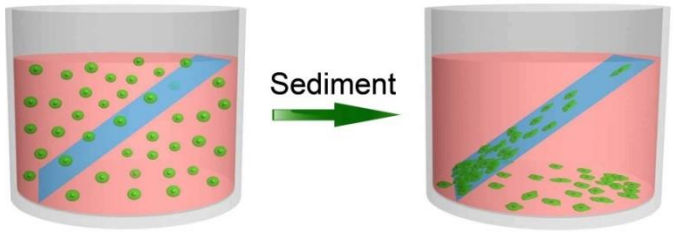

Figure 2.13. *A schematic of the experimental setup. A glass slide is placed at a tilted angle in a beaker filled with a homogeneous suspension of cells. Due to the varying volumes of cells available for sedimentation above the slide, the cells are deposited on the slide with a gradient in density.*

2.3.1 Generation of Different Gradient Profiles by Varying the Tilted Angle

The experiments were carried out with the glass slides being tilted at 15, 30, and 45 degrees, respectively. In order to improve cell attachment, the glass slides were pre-coated with fibronectin and then inserted into homogeneous suspensions of MC3T3 preosteoblasts at a concentration of 2×10^5/mL (one slide per cell suspension). This concentration of cells was chosen to allow for a clear observation of cell density by fluorescence staining. All the glass slides were 5 cm in length. The highest point on a slide during the sedimentation

process was denoted as the starting point and the lowest point was denoted as the position of 5 cm. The schematic in Figure 2.14 shows a detailed description of the experimental design. The volume of the cell suspension was set in such a way that the starting point of each slide was barely immersed for each tilted angle. Therefore, the depth of the cell suspension in the beaker was $5\times\sin15^{o}=1.3$ cm, $5\times\sin30^{o}=2.5$ cm, and $5\times\sin45^{o}=3.53$ cm for tilted angles of 15, 30, and 45 degrees, respectively. Similarly, the relationship between the distance to air/water interface for any given point on the slide, D, its location along the length of the slide, L, and the tilted angle θ is: $D = L\cdot\sin\theta$ (Figure 2.14). In this way, all of the gradient patterns started from a density of zero at the starting point (*i.e.*, there were no cells at this position available for sedimentation). In an alternative protocol, one could fix the volume of cell suspension for all samples so all of the slides would have the same cell density at the position of 5 cm. However, this scenario would result in variable cell densities at the starting point, and the pattern of the gradient would not stand out as clearly. Therefore, the former protocol was adopted for the entire study.

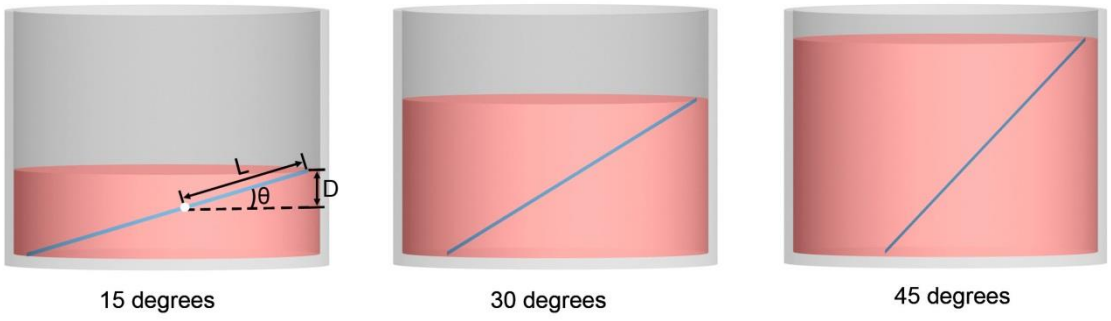

Figure 2.14. *Schematics showing the detailed experimental design. At a given tilted angle, the volume of the cell suspension was set such that the surface of the medium was at the same height of the top of the glass slide.*

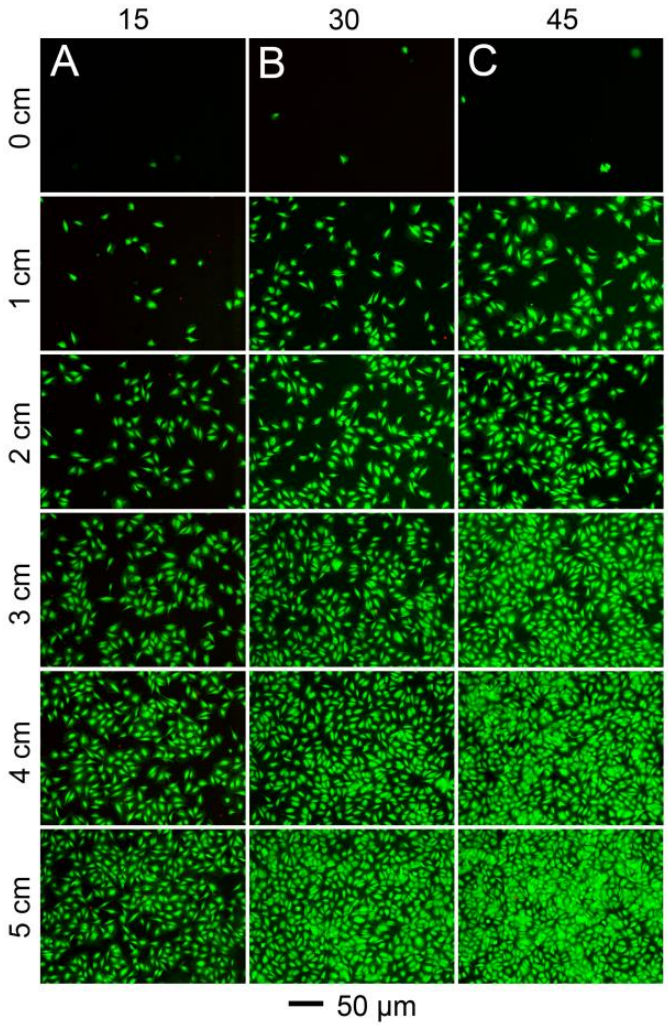

Figure 2.15. *Fluorescence micrographs showing gradients in cell density generated on glass slides at tilted angles of (A) 15, (B) 30, and (C) 45 degrees, respectively. The cells were stained with a live/dead kit immediately after seeding to give live and dead cells green and red colors, respectively.*

Live/dead staining was performed immediately after sedimentation to help visualize the cells, where live and dead cells were stained green and red, respectively (Figure 2.15). As expected, all the samples had cell viabilities close to 100% after sedimentation. While all the three groups showed gradient patterns, the cell density increased faster at a larger tilted angle. There were almost no cells present at the starting point in any of the three groups. Different cell densities were observed at the 5-cm position depending on the tilted angle, with the lowest cell density at 15 degrees (Figure 2.15A),

intermediate cell density at 30 degrees (Figure 2.15B), and the highest cell density at 45 degrees (Figure 2.15C). These results suggest that the slope of the gradient can be tuned by simply changing the tilted angle of the glass slide during cell seeding.

The relationships between the fluorescence intensities of the cells and their locations on the glass slides are plotted in Figure 2.16A. In all cases, a linear regression provided a close fit to the data, indicating that local cell density increased linearly with position on the glass slide. The slopes of the regression lines were calculated to be 4.0, 7.5, and 10.5 for tilted angles of 15, 30, and 45 degrees, respectively. The linear relationship between the tilted angle and cell density supported my hypothesis that the density of cells on the slide depends on the depth in the cell suspension. As expected, the slope of the regression also adopted a linear relationship with sinθ (Figure 2.16B).

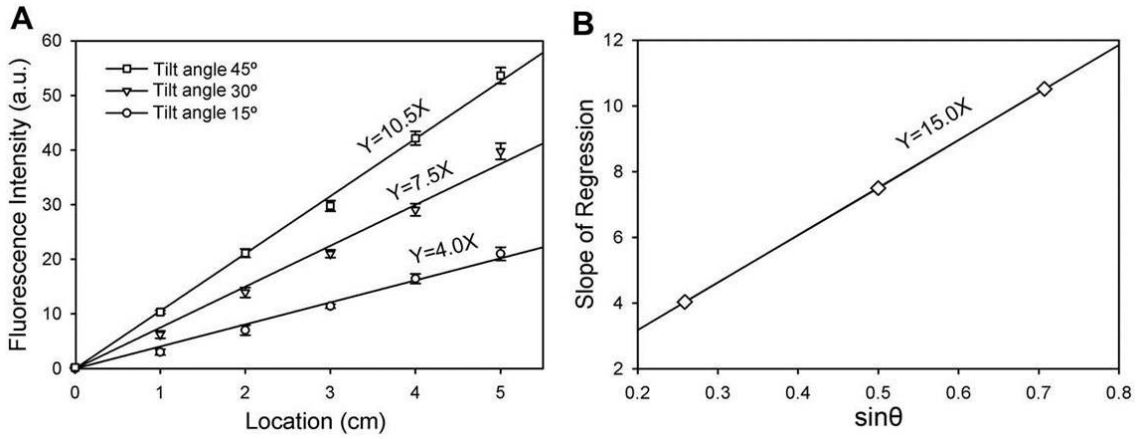

Figure 2.16. *(A) Plots showing linear correlations between the cell densities and the positions on the glass slides at three different tilted angles.* R^2*=0.99 for all groups. (B) The linear relationship between the slope of regression and the value of sinθ, where θ is the tilted angle.*

To test the predictive power of this relationship, I calculated the expected cell density for a tilted angle of 75 degrees using the regression equation and seeded cells onto a slide placed in a cell suspension at a tilted angle of 75 degrees. The slope of regression for the cell density gradient at a tilted angle of 75 degrees was predicted to be 14.5.

However, seeding cells at 75 degrees for 2 h did not support this estimation, with very few cells adhering to the entire glass slide (Figure 2.17A). One possible reason for the observed low cell density is that, at large angles, most of the cells rolled down to the bottom of the container before they had a chance to adhere to the substrate.

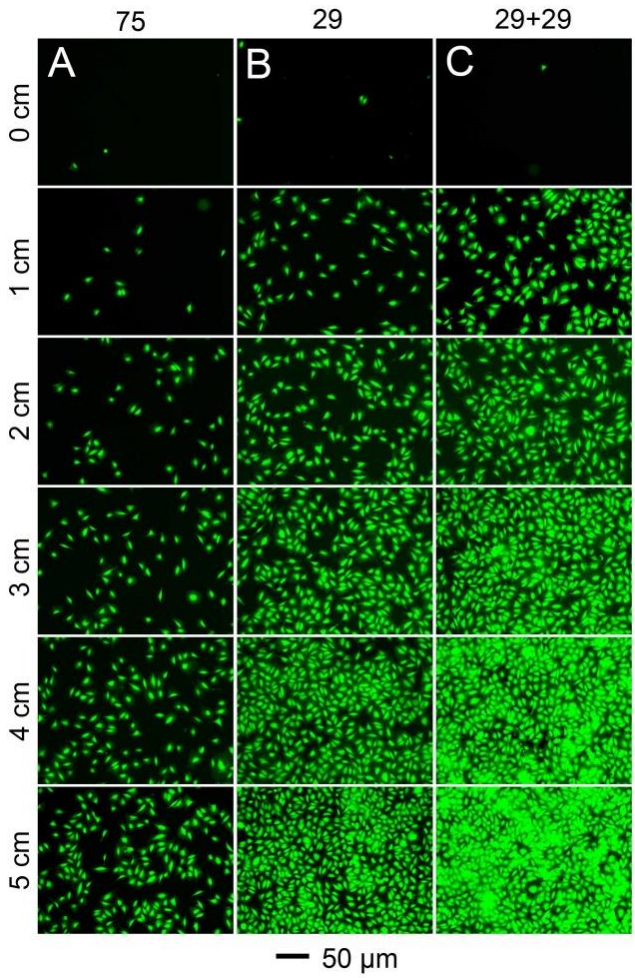

Figure 2.17 *Fluorescence micrographs showing gradients in cell density generated on glass slides at tilted angles of (A) 75 and (B) 29 degrees, respectively. (C) Cumulative gradients in cell density generated after two consecutive seeding processes at 29 degrees. The cells were stained using a live/dead kit immediately after seeding to give live and dead cells green and red colors, respectively.*

Since $2 \cdot \sin 29^{o}$ was roughly the same as $\sin 75^{o}$, I performed two sequential seedings at 29 degrees to obtain the gradient in cell density estimated for a tilted angle of 75 degrees.

Figure 2.17B shows the gradient after the first seeding process at 29 degrees. Figure 2.17C shows the cumulative gradient after two sequential seeding procedures at 29 degrees. The fluorescence intensity at each location fit well with the prediction, with a slope of 14.6 (Figure 2.18). These data indicate that consecutive seeding processes can be used to overcome cell adhesion issues associated with large tilted angles, where cell rolling across the surface becomes an issue.

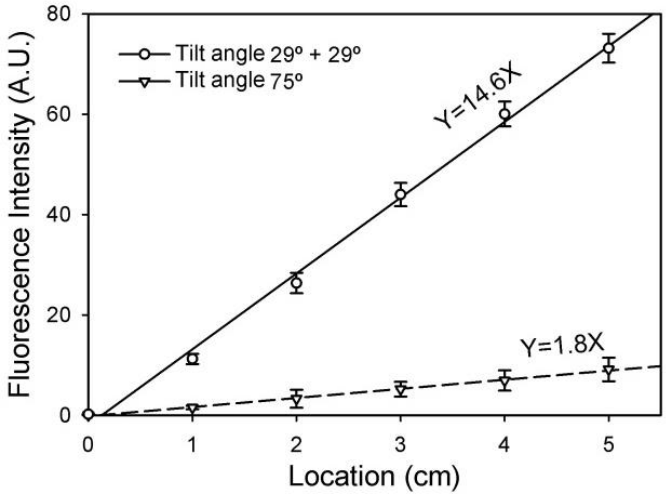

Figure 2.18. *Quantification of the gradients in cell density fabricated using either a single seeding process at a tilted angle of 75 degrees or two consecutive seeding processes at a tilted angle of 29 degrees each.* R^2*=0.99 for both groups.*

I was also able to generate opposite gradients in cell density on the same glass slide. Specifically, MC3T3 preosteoblasts and TFBs were used to generate reverse gradients for the densities of these two cell types. MC3T3 and TFB were pre-labeled with DiO (green) and DiI (red), respectively, prior to sedimentation. The MC3T3 preosteoblasts were seeded onto the glass slide at a tilted angle of 30 degrees for 2 h. The glass slide was briefly rinsed with culture medium to wash off loosely attached cells and observed under a fluorescence microscope (Figure 2.19). The glass slide was then horizontally rotated for 180 degrees and inserted into a suspension of TFBs at a tilted angle of 30 degrees for 2 h. After washing

off loosely attached TFBs, the glass slide was imaged again.

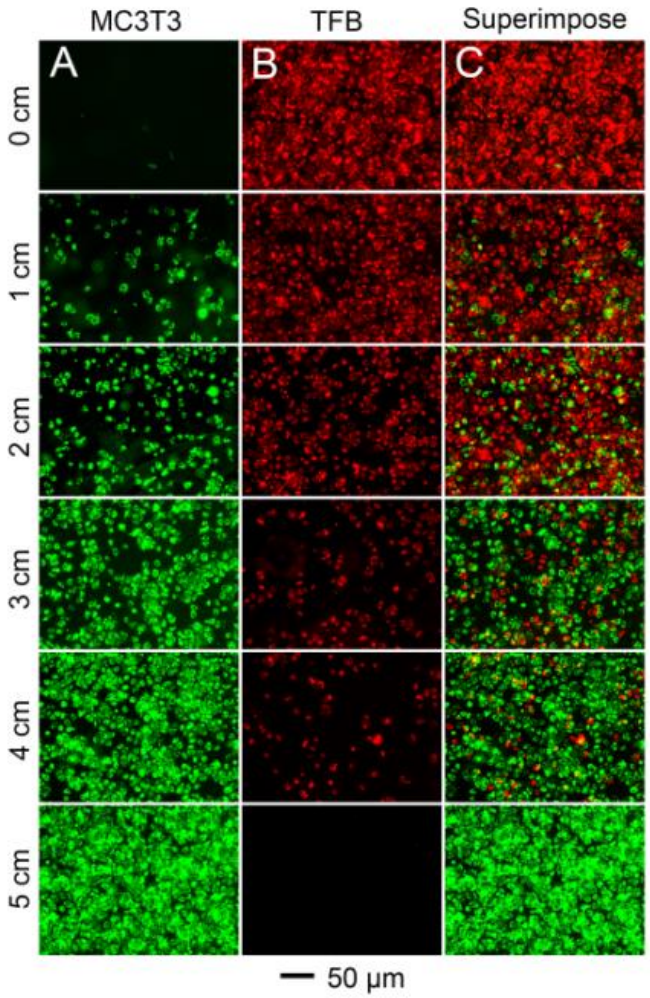

Figure 2.19. *Fluorescence micrographs showing the generation of reverse gradients in cell density for MC3T3 preosteoblasts and TFB on the same glass slide after two consecutive sedimentation processes along opposite directions. The two types of cells were labeled with different membrane dyes prior to seeding.*

As shown in Figure 2.19A, a similar gradient in the density of TFB cells was generated along the glass slide but in the reverse direction of MC3T3 preosteoblasts. Figure 2.19C shows a superimposed image of the images in Figure 2.19, A and B, indicating a transition zone at the center of the scaffold where MC3T3 preosteoblasts and TFBs were

brought into close proximity.

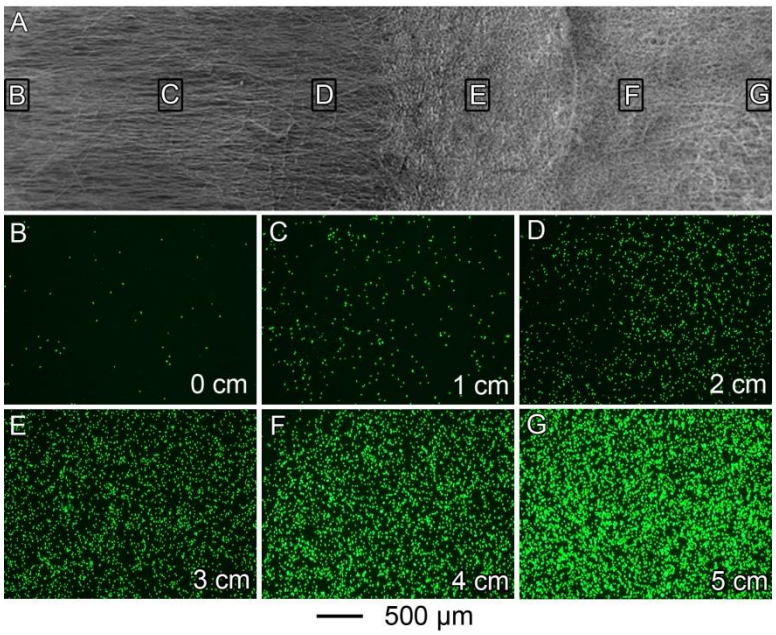

Figure 2.20. *Micrographs showing the gradient in density for MC3T3 preosteoblasts on a scaffold of electrospun nanofibers that was attached to the surface of a glass slide. The tilting angle was 30 degrees. A) SEM image of the nanofiber scaffold with both aligned and random regions. B-G) Fluorescence micrographs taken from the regions indicated by small boxes in (A). The cells were stained with calcein AM before imaging.*

The gradient in cell density could also be fabricated on a scaffold of electrospun nanofibers using the same procedure (Figure 2.20). The scaffold was attached to a glass slide prior to seeding and the tilted angle was set to 30 degrees. The scaffold was designed to have two different types of structures with uniaxially aligned nanofibers on one region and random nanofibers on the other. When placed in the cell suspension, the random nanofibers were kept at the bottom whereas the aligned end was kept at the top. A clear gradient in cell density can be observed on the scaffold with no obvious difference in cell attachment between the aligned region and the random region. This observation indicates that both aligned and random nanofibers are suitable substrates for the generation of

gradients in cell density using this simple method.

There are several advantages associated with this method for generating gradients in cell density as compared to previously published approaches [42-44]. First, the experimental setup is simple and cell-friendly compared to the printing techniques for live cells. Maintaining sterility is trivial for the method presented in this study, but can be difficult for the cell printing approaches. Due to minimal cell processing, it is expected that the cells will display similar behaviors to the cells plated using the conventional methods. A second advantage of the method presented here is the predictability of the gradient based on the tilted angle. A simple linear relationship can be used to reproducibly generate cell gradients in a particular profile. A third advantage of the present method is the ability to easily produce complex gradients in terms of patterns and cell types *via* sequential seeding processes, many of which would be difficult to be fabricated using the previously reported techniques.

2.4 Summary

In this chapter, I discussed two approaches to generating continuous gradient in cell phenotypes for mimicking the cell distribution in native tendon-to-bone insertion. In the first approach, nanofiber scaffolds with graded mineral coatings were used as substrates to induce spatially controlled osteogenesis of ASCs. The scaffolds were fabricated by gradually adding 10SBF coating solution into a glass vial containing nanofibers supported on a frame with an orientation close to the vertical direction. ASCs not only remained viable on the scaffolds, but also differentiated into osteoblasts, whose density was positively correlated with the mineral content.

In the second approach, a gradient in cell density was generated by inserting a scaffold into a homogeneous suspension of cells at a tilted angle. Since the amount of cells above the scaffold varied, a gradient in cell density could form as the cells sedimented. Different gradients in cell density could be generated by varying the tilted angle. Reverse

gradients in TFBs and osteoblasts, as seen in native enthesis, could be generated using multiple sedimentation procedures. I allowed the TFBs to sediment first, rotated the scaffold horizontally by 180 degrees, and then performed a second sedimentation with MC3T3 preosteoblasts. Both approaches described in this chapter are efficient in generating gradients in cell phenotypes and can be employed to fabricate scaffolds for the tendon-to-bone insertion repair.

2.5 Experimental

2.5.1 Experimental Procedures for Inducing Graded Osteogenesis of ASCs *in vitro*

2.5.1.1 Materials

PLGA (M_w=50,000-75,000, lactide:glycolide = 85:15), dichloromethane (DCM), dimethylformaldehyde (DMF), acetic acid, and all chemicals used for the preparation of 10SBF were obtained from Sigma-Aldrich (St. Louis, MO). All chemicals were used as received.

2.5.1.2 Electrospinning and Plasma Treatment

The solution for electrospinning was prepared by dissolving PLGA in a mixture of DCM and DMF (with a volume ratio of 80:20) at a concentration of 25%. The solution was loaded into a 5 mL plastic syringe with a 23 ½-gauge needle attached, and dispensed using a syringe pump. The injection rate was 0.5 mL/h. The fibers were collected using a rotating mandrel at a speed of 2 m/s. The distance between the tip of needle and the collector was about 20 cm, and a voltage of 15 kV was applied. The electrospun nanofiber scaffold was then transferred onto a metal frame for plasma treatment. Plasma treatment was conducted in a plasma cleaner (PE50, Unitronics, NV) for 3 min to make the scaffold hydrophilic and completely wettable by the coating solution.

2.5.1.3 Generation of a Mineral Gradient

A stock solution of 10SBF containing NaCl, KCl, $CaCl_2$, $MgCl_2$, and $NaH_2PO_4 \cdot H_2O$ was prepared in advance, and $NaHCO_3$ was added at room temperature

prior to initiation of the mineralization process [7]. To create a gradient in mineral along the longitudinal direction of the scaffold, the as-prepared mineral solution was loaded into a 50-mL plastic syringe and fed continuously into a glass vial using a syringe pump at a feeding rate of 36 mL/h. A uniaxially aligned nonwoven mat of electrospun nanofibers supported on a metal frame was placed inside the vial at a tilted angle. Prior to the coating process, the scaffolds were pre-soaked in 10SBF(without $NaHCO_3$) for 0.5 h, allowing for the easier attachment of mineral coatings.

2.5.1.4 Characterization of Mineral Content and Morphology

A SEM (Ultra 60, Carl Zeiss, Thornwood, NY) was used to examine the morphologies of the deposited minerals crystals at different locations along the longitudinal direction of nanofiber scaffolds. The atomic ratio Ca/(Ca+C)% was determined at different locations along the length of the scaffold using EDX. Three samples were examined.

2.5.1.5 ASC Isolation, Culture and Seeding

All animal protocols were approved by the Washington University Animal Studies Committee. ASCs were isolated from young Sprague-Dawley rats obtained from Charles River Labs (Wilmington, MA) using standard techniques [45]. Animals were sacrificed using carbon dioxide narcosis. Fat was isolated from the subdermal abdomen and minced using scalpel blades. The minced fat was then placed into a solution of 0.2 wt% Collagenase A (Roche, Indianapolis, IN) for 2 h in a cell culture incubator (37 °C, 95% relative humidity, 5% CO_2). After incubation, the solution was centrifuged and the fat and collagenase solution were removed. The remaining suspension was filtered using a Nylon 100 μm filter (Fisher Scientific, Pittsburgh, PA) and cultured in a standard proliferation medium -- α-Minimum Essential Medium (α-MEM, Invitrogen, Carlsbad, CA), 10% fetal bovine serum (FBS, Invitrogen), 1:1000 penicillin/streptomycin (P/S, Invitrogen), and 1% Amphotericin B (Fisher Scientific). The culture was washed after 24 h with phosphate buffered saline (PBS, Invitrogen) to remove any remaining debris and passaged once to assure adherence selection. The cells were incubated at 37 °C under 95% relative humidity

and 5% CO_2. The medium was changed every 2 days until 80% confluence. Cells were seeded onto rectangular nanofiber scaffolds (1×5 cm^2) glued to petri dishes. 2×10^5 cells (as determined by hemocytometer counting) were seeded onto each scaffold. All ASCs were isolated from one rat. All cells for this study were used at passage 2. The cells isolated in the present work demonstrated pluipotency based on standard adipogenic, osteogenic, chonodrogenic, and tenogenic protocols reported in our previous study [46].

2.5.1.6 Live/dead Assay

A live/dead assay kit (Invitrogen), consisting of calcein AM and ethidium homodimer-1 (EthD-1), was used to assess cell viability and cell distribution. The intracellular esterase present in live cells converts calcein AM, a cell permeable dye, to calcein, resulting in a bright green fluorescence. EthD-1 can only penetrate damaged membranes of dead cells where it binds to nucleic acids, producing intense red fluorescence. Briefly, the cells were incubated for 30 min with regular culture medium supplemented with 2 μM calcein AM and 4 μM EthD-1, and analyzed via fluorescent microscopy (Leica DMI6000, Buffalo Grove, IL). Three samples from each group were analyzed at each time point.

2.5.1.7 Cell Viability Assay

The relative number of cells on each scaffold was quantitatively measured by the MTT assay (Invitrogen). MTT is a tetrazole that is metabolized and reduced to purple formazan in live cells. Each scaffold (1×5 cm^2) was cut into 10 pieces, resulting in 0.5×1 cm^2 area per piece. At each time point, 3 samples were analyzed. Assays were carried out in 12-well plates, and 40 μL of MTT solution in PBS (5 mg/mL) was added to each well and incubated at 37 ^oC for 4 h. Culture medium was then withdrawn and 1 mL isopropanol was added to each well to completely dissolve formazan crystals throughout the scaffolds. Absorbance was measured at 560 nm using a spectrophotometer (Infinite 200 Pro, TECAN, Morrisville, NC). All final data were normalized to the dry weight of each scaffold.

2.5.1.8 ALP Staining and Immunocytochemistry

ALP staining was performed using Vector Red Alkaline Phosphatase Substrate Kit (SK-5100, Vector Laboratories, Burlingame, CA) according to the manufacturer's instructions. ALP activities were quantified based on the mean pixel intensity using Image J. Three samples from each group were analyzed at each time point.

PCNA was purchased from Invitrogen. Antibodies for Runx2 and OCN were purchased from Abcam (Cambridge, MA). The scaffolds were fixed in 3.7% formaldehyde (Sigma-Aldrich) in PBS. The cells were then permeabilized in 0.1% Triton X-100 (Sigma-Aldrich) in PBS for 1 h. Subsequently, the cells were blocked with 5% normal goat serum (Sigma-Aldrich) and 1.5% bovine serum albumin (Sigma-Aldrich) in PBS for 1 h. Each of the primary antibodies (dilution: PCNA 1:20, Runx2 1:100, and OCN 1:200) was then applied separately to scaffold samples in blocking buffer at 4 ^{o}C overnight. After washing, the samples were incubated with Alexa Fluor 488 goat anti-mouse IgG (1:200 in PBS, Invitrogen) for 1 h, washed, and observed under the fluorescence microscope. Three samples from each group were analyzed at each time point.

2.5.1.9 Statistical analysis

Results are presented in the form of mean ± standard deviation, with "N" indicating the number of samples per group. A three factor analysis of variance (ANOVA) was used to determine the effects of culture time, culture medium, and mineral content on cell distribution and ALP activities on the scaffolds. Tukey's post-hoc test was used for all pair-wise comparisons and significance was attained at $p<0.05$. Statistical analyses were performed with Systat 13 (Crane Software International, Chicago, IL).

2.5.2 Experimental Procedures for Generating Controllable Gradient in Cell Density

2.5.2.1 Cell Culture

MC3T3 preosteoblasts (ATCC, Manassas, VA) and TFBs (courtesy of Dr. Thomopoulos) were maintained in α-MEM (Invitrogen) supplemented with 10 % fetal bovine serum (ATCC) and 1 % P/S (Invitrogen). The culture medium was changed every

other day.

2.5.2.2 Coating of Fibronectin

Fibronectin (Sigma-Aldrich, St. Louis, MO) solution was prepared at the concentration of 5 μg/mL. Glass slides were soaked in the fibronectin solution for 12 hr at 4ºC. All slides were rinsed for 3 times in de-ionized water before using.

2.5.2.3 Generation of gradients in cell density

MC3T3 preosteoblasts or TFB cells were de-attached from culture flasks at the confluency of ~80% using 0.5% trypsin (Sigma-Aldrich) and prepared as a homogeneous suspension in culture medium at a density of 2×10^5/mL in a sterile beaker. A glass slide was gently inserted into the cell suspension at a preset tile angle, and the cells were allowed to sediment and attach for 2 h. The scaffold was then gently rinsed with PBS (Invitrogen) to wash off loosely-bound cells. In the case of co-culture, the glass slide was seeded first with MC3T3 preosteoblasts, rinsed, and then inserted into a suspension of TFBs in the reverse tilting direction for 2 h. For visualization, the cells were either pre-labeled with membrane dyes (DiO and DiI, Invitrogen) prior to seeding, or post-labeled with live/dead cell viability kit (Invitrogen) immediately after seeding, according to manufacturer's instructions. Fluorescence micrographs were taken with a Leica DMI6000 inverted microscope (Leica, Buffalo Grove, IL). Fluorescence intensities were quantified using ImageJ software (National Institutes of Health, Bethesda, MD).

2.6 References

[1] Thomopoulos, S.; Williams, G.; Soslowsky, L. Tendon to bone healing: Differences in biomechanical, structural, and compositional properties due to a range of activity levels. *J. Biomech. Eng.* **2003**, *125*, 106-113.

[2] Thomopoulos, S.; Williams, G. R.; Gimbel, J. A.; Favata, M.; Soslowsky, L. J. Variation of biomechanical, structural, and compositional properties along the tendon to bone insertion site. *J. Orthop. Res.* **2003**, *21*, 413-419.

[3] Wopenka, B.; Kent, A.; Pasteris, J. D.; Yoon, Y.; Thomopoulos, S. The tendon-to-bone transition of the rotator cuff: A preliminary Raman spectroscopic study documenting the gradual mineralization across the insertion in rat tissue samples. *Appl. Spec.* **2008**, *62*, 1285-1294.

[4] Thomopoulos, S.; Genin, G. M.; Galatz, L. M. The development and morphogenesis of the tendon-to-bone insertion what development can teach us about healing. *J. Musculoskelet. Neuro. Interactions* **2010**, *10*, 35.

[5] Smith, L.; Xia, Y.; Galatz, L. M.; Genin, G. M.; Thomopoulos, S. Tissue-engineering strategies for the tendon/ligament-to-bone insertion. *Connect. Tissue Res.* **2012**, *53*, 95-105.

[6] Lester, S.; Stavros, T. Tendon/ligament-to-bone tissue engineering: Current and emerging strategies. *Connect. Tissue Res.* **2012**, *53*, 95-105.

[7] Li, X.; Xie, J.; Lipner, J.; Yuan, X.; Thomopoulos, S.; Xia, Y. Nanofiber scaffolds with gradations in mineral content for mimicking the tendon-to-bone insertion site. *Nano Lett.* **2009**, *9*, 2763-2768.

[8] Gimble, J. M. Adipose tissue-derived therapeutics. *Expert Opin. Biol. Therapy* **2003**, *3*, 705-713.

[9] Gimble, J. M.; Katz, A. J.; Bunnell, B. A. Adipose-derived stem cells for regenerative medicine. *Circ. Res.* **2007**, *100*, 1249-1260.

[10] Niemeyer, P.; Kornacker, M.; Mehlhorn, A.; Seckinger, A.; Vohrer, J.; Schmal, H.; Kasten, P.; Eckstein, V.; Südkamp, N. P.; Krause, U. Comparison of immunological properties of bone marrow stromal cells and adipose tissue-derived stem cells before and after osteogenic differentiation in vitro. *Tissue Eng.* **2007**, *13*, 111-121.

[11] Fang, B.; Song, Y.; Liao, L.; Zhang, Y.; Zhao, R. In *Favorable response to human adipose tissue-derived mesenchymal stem cells in steroid-refractory acute graft-versus-host disease,* Transplantation proceedings, Elsevier: 2007; pp 3358-3362.

[12] Yanez, R.; Lamana, M. L.; García-Castro, J.; Colmenero, I.; Ramirez, M.; Bueren, J. A. Adipose tissue-derived mesenchymal stem cells have in vivo immunosuppressive properties applicable for the control of the graft-versus-host disease. *Stem Cells* **2006**, *24*, 2582-2591.

[13] Liu, W.; Lipner, J.; Xie, J.; Manning, C. N.; Thomopoulos, S.; Xia, Y. Nanofiber scaffolds with gradients in mineral content for spatial control of osteogenesis. *ACS Appl. Mater. Interfaces* **2014**, *6*, 2842-2849.

[14] Liu, W.; Zhang, Y.; Thomopoulos, S.; Xia, Y. Generation of controllable gradients in cell density. *Angew. Chem. Int. Edt.* **2013**, *52*, 429-432.

[15] Tas, A. C.; Bhaduri, S. B. Rapid coating of Ti6Al4V at room temperature with a calcium phosphate solution similar to 10× simulated body fluid. *J. Mater. Res.* **2004**, *19*, 2742-2749.

[16] Robison, R. The possible significance of hexosephosphoric esters in ossification. *Biochem. J.* **1923**, *17*, 286.

[17] Marom, R.; Shur, I.; Solomon, R.; Benayahu, D. Characterization of adhesion and differentiation markers of osteogenic marrow stromal cells. *J. Cell. Physiol.* **2005**, *202*, 41-48.

[18] Golub, E. E.; Boesze-Battaglia, K. The role of alkaline phosphatase in mineralization. *Curr. Opin. Orthop.* **2007**, *18*, 444-448.

[19] Pratap, J.; Galindo, M.; Zaidi, S. K.; Vradii, D.; Bhat, B. M.; Robinson, J. A.; Choi, J.-Y.; Komori, T.; Stein, J. L.; Lian, J. B. Cell growth regulatory role of runx2 during proliferative expansion of preosteoblasts. *Cancer Res.* **2003**, *63*, 5357-5362.

[20] Ducy, P.; Zhang, R.; Geoffroy, V.; Ridall, A. L.; Karsenty, G. Osf2/cbfa1: A transcriptional activator of osteoblast differentiation. *Cell* **1997**, *89*, 747-754.

[21] Komori, T. Regulation of skeletal development by the runx family of transcription factors. *J. Cell. Biochem.* **2005**, *95*, 445-453.

[22] Komori, T. Regulation of osteoblast differentiation by transcription factors. *J. Cell. Biochem.* **2006**, *99*, 1233-1239.

[23] Otto, F.; Thornell, A. P.; Crompton, T.; Denzel, A.; Gilmour, K. C.; Rosewell, I. R.; Stamp, G. W.; Beddington, R. S.; Mundlos, S.; Olsen, B. R. *Cbfa1*, a candidate gene for cleidocranial dysplasia syndrome, is essential for osteoblast differentiation and bone development. *Cell* **1997**, *89*, 765-771.

[24] Hauschka, P. V.; Lian, J. B.; Cole, D.; Gundberg, C. M. Osteocalcin and matrix gla protein: Vitamin k-dependent proteins in bone. *Physiol. Rev.* **1989**, *69*, 990-1047.

[25] Harada, S.-i.; Rodan, G. A. Control of osteoblast function and regulation of bone mass. *Nature* **2003**, *423*, 349-355.

[26] Lee, N. K.; Sowa, H.; Hinoi, E.; Ferron, M.; Ahn, J. D.; Confavreux, C.; Dacquin, R.; Mee, P. J.; McKee, M. D.; Jung, D. Y. Endocrine regulation of energy metabolism by the skeleton. *Cell* **2007**, *130*, 456-469.

[27] Oreffo, R. O.; Driessens, F.; Planell, J. A.; Triffitt, J. T. Growth and differentiation of human bone marrow osteoprogenitors on novel calcium phosphate cements. *Biomaterials* **1998**, *19*, 1845-1854.

[28] Deligianni, D. D.; Katsala, N. D.; Koutsoukos, P. G.; Missirlis, Y. F. Effect of surface roughness of hydroxyapatite on human bone marrow cell adhesion, proliferation, differentiation and detachment strength. *Biomaterials* **2000**, *22*, 87-96.

[29] Murphy, W. L.; Hsiong, S.; Richardson, T. P.; Simmons, C. A.; Mooney, D. J. Effects of a bone-like mineral film on phenotype of adult human mesenchymal stem cells in vitro. *Biomaterials* **2005**, *26*, 303-310.

[30] Chou, L.; Marek, B.; Wagner, W. Effects of hydroxylapatite coating crystallinity on biosolubility, cell attachment efficiency and proliferation *in vitro*. *Biomaterials* **1999**, *20*, 977-985.

[31] Chang, Y. L.; Stanford, C. M.; Keller, J. C. Calcium and phosphate supplementation promotes bone cell mineralization: Implications for hydroxyapatite (HA)-enhanced bone formation. *J. Biomed. Mater. Res.* **2000**, *52*, 270-278.

[32] Meleti, Z.; Shapiro, I.; Adams, C. Inorganic phosphate induces apoptosis of osteoblast-like cells in culture. *Bone* **2000**, *27*, 359-366.

[33] Ong, J.; Hoppe, C.; Cardenas, H.; Cavin, R.; Carnes, D.; Sogal, A.; Raikar, G. Osteoblast precursor cell activity on ha surfaces of different treatments. *J. Biomed. Mater. Res.* **1998**, *39*, 176-183.

[34] Li, X.; Xie, J.; Yuan, X.; Xia, Y. Coating electrospun poly(ε-caprolactone) fibers with gelatin and calcium phosphate and their use as biomimetic scaffolds for bone tissue engineering. *Langmuir* **2008**, *24*, 14145-14150.

[35] Kaito, T.; Myoui, A.; Takaoka, K.; Saito, N.; Nishikawa, M.; Tamai, N.; Ohgushi, H.; Yoshikawa, H. Potentiation of the activity of bone morphogenetic protein-2 in bone regeneration by a pla–peg/hydroxyapatite composite. *Biomaterials* **2005**, *26*, 73-79.

[36] Zhang, P.; Hong, Z.; Yu, T.; Chen, X.; Jing, X. *In vivo* mineralization and osteogenesis of nanocomposite scaffold of poly (lactide-*co*-glycolide) and hydroxyapatite surface-grafted with poly (*l*-lactide). *Biomaterials* **2009**, *30*, 58-70.

[37] Kim, S.-S.; Sun Park, M.; Jeon, O.; Yong Choi, C.; Kim, B.-S. Poly (lactide-*co*-glycolide)/hydroxyapatite composite scaffolds for bone tissue engineering. *Biomaterials* **2006**, *27*, 1399-1409.

[38] Lü, L.-X.; Zhang, X.-F.; Wang, Y.-Y.; Ortiz, L.; Mao, X.; Jiang, Z.-L.; Xiao, Z.-D.; Huang, N.-P. Effects of hydroxyapatite-containing composite nanofibers on osteogenesis of mesenchymal stem cells in vitro and bone regeneration *in vivo*. *ACS Appl. Mater. Interfaces* **2013**, *5*, 319-330.

[39] Venugopal, J.; Rajeswari, R.; Shayanti, M.; Low, S.; Bongso, A.; R. Giri Dev, V.; Deepika, G.; Choon, A. T.; Ramakrishna, S. Electrosprayed hydroxyapatite on polymer nanofibers to differentiate mesenchymal stem cells to osteogenesis. *J. Biomater. Sci. Polym. Ed.* **2013**, *24*, 170-184.

[40] Ravichandran, R.; Venugopal, J. R.; Sundarrajan, S.; Mukherjee, S.; Ramakrishna, S. Precipitation of nanohydroxyapatite on PLLA/PBLG/collagen nanofibrous structures for the differentiation of adipose derived stem cells to osteogenic lineage. *Biomaterials* **2012**, *33*, 846-855.

[41] Mygind, T.; Stiehler, M.; Baatrup, A.; Li, H.; Zou, X.; Flyvbjerg, A.; Kassem, M.; Bünger, C. Mesenchymal stem cell ingrowth and differentiation on coralline hydroxyapatite scaffolds. *Biomaterials* **2007**, *28*, 1036-1047.

[42] Helm, C.-L. E.; Fleury, M. E.; Zisch, A. H.; Boschetti, F.; Swartz, M. A. Synergy between interstitial flow and vegf directs capillary morphogenesis *in vitro* through a gradient amplification mechanism. *Proc. Natl. Acad. Sci. USA* **2005**, *102*, 15779-15784.

[43] Cheng, S.-Y.; Heilman, S.; Wasserman, M.; Archer, S.; Shuler, M. L.; Wu, M. A hydrogel-based microfluidic device for the studies of directed cell migration. *Lab Chip* **2007**, *7*, 763-769.

[44] Wan, A. M.; Brooks, D. J.; Gumus, A.; Fischbach, C.; Malliaras, G. G. Electrical control of cell density gradients on a conducting polymer surface. *Chem. Commun.* **2009**, 5278-5280.

[45] Guilak, F.; Lott, K. E.; Awad, H. A.; Cao, Q.; Hicok, K. C.; Fermor, B.; Gimble, J. M. Clonal analysis of the differentiation potential of human adipose-derived adult stem cells. *J. Cell. Physiol.* **2006**, *206*, 229-237.

[46] Shen, H.; Gelberman, R. H.; Silva, M. J.; Sakiyama-Elbert, S. E.; Thomopoulos, S. Bmp12 induces tenogenic differentiation of adipose-derived stromal cells. *Plos One* **2013**, *8*, e77613.

CHAPTER 3

ENHANCING THE STIFFNESS OF ELECTROSPUN NANOFIBERS WITH IMPROVED SURFACE MINERALIZATION

3.1 Introduction

In Section 2.2, I discussed how to generate graded mineral coatings on electrospun nanofibers to mimic the compositional transition in the ECM of tendon-to-bone insertion. I employed 10SBF to generate mineral coatings on nanofibers, which were able to induce osteogenesis of ASCs. Although this method was effective in creating a gradient in stiffness of the scaffold, the stiffness of the fully mineralized end still needed to be enhanced.

Previous work has shown that a stiff substrate could induce osteogenesis since integrin-mediated cell adhesion to matrix proteins is the first step that determines the fate of the stem cells and can therefore play an important role in osteogenesis [1]. Once integrins are bound to their ligands, they form specialized protein clusters called focal adhesions. These complexes ensure substrate adhesion and directed assembly of actin filaments. During osteogenesis, morphology of the cells often changes from fibroblast-like (pre-osteoblast) to a flattened and polygonal shape (mature osteoblast) [2]. The changes in the assembly and disassembly of the actin cytoskeleton are therefore critical in supporting osteogenesis [3, 4]. Since the stiffness of a substrate greatly affects the dynamics of actin assembly in individual cells, the enhanced stiffness of the scaffold, due to incorporated minerals, may be a contributing factor to the enhanced osteogenesis.

Given that increasing the stiffness of scaffolds can promote osteogenesis, the fabrication of nanofiber scaffolds with enhanced stiffness is of vital importance. The highly mineralized end of a nanofiber scaffold coated with 10SBF only displayed a moderate Young's modulus of ~120 MPa, compared to ~40 MPa for pristine samples [5]. A possible

reason lies in the fact that the structure of the mineral coating was highly porous, due to the relatively large and randomly oriented grain sizes of the mineral phase. The mineral coating typically exhibited a flower-like morphology leading to large void spaces between adjacent grains. Reducing this porosity may enhance the mechanical properties of the scaffolds. Previous reports have shown a simultaneous increase in both hardness and toughness of calcium phosphate films as the grain sizes were reduced from micrometer to nanometer scale [6].

To this end, m10SBF was developed in the current study to reduce of the grain size of mineral coating on electrospun nanofibers. The major difference between 10SBF and m10SBF was the concentration of bicarbonate ion (HCO_3^-) in the solution. In m10SBF, an increased concentration of HCO_3^- was used, since it has been reported that this ionic species can reduce the grain size of calcium phosphate [7]. My hypothesis for the current study was that the increased concentration of HCO_3^- in the m10SBF solution would enhance the stiffness of the nanofibers by producing mineral coatings with smaller grain sizes. Furthermore, it has been reported that negatively charged surfaces are favorable for the heterogeneous nucleation of calcium phosphate [8-11]. The accepted interpretation is that the accumulation of Ca^{2+} ions, due to electrostatic attraction, induces supersaturation near a negatively charged surface and, as such, initial nucleation can be preferentially induced. Therefore, immobilization of negatively charged species on the nanofiber surface may enhance the heterogeneous nucleation of calcium phosphate on that surface, and subsequently increase the thickness of the mineral coating. Increased stiffness could therefore be achieved by reducing the grain size and increasing the density and thickness of the mineral coating [12].

3.2 The Effect of Surface Charge

In this section, four different methods of surface treatment were studied to graft molecules with different signs of charges onto nanofibers. Their effect in promoting the

formation of a dense, thick coating of mineral was also investigated. The experimental parameters for the preparation of all samples are listed in Table 3.1.

Table 3.1. Summary of experimental parameters for sample preparation

Sample	Surface Treatment			HCO_3^- Concentration			Coating
No.	plasma	chitosan	heparin	21	42	63	Round*
1	×	×	×	×	×	×	0
2	×	×	×	×	✓	×	1
3	✓	×	×	×	✓	×	1
4	✓	✓	×	×	✓	×	1
5	✓	✓	✓	×	✓	×	1
6	✓	✓	✓	✓	×	×	3
7	✓	✓	✓	×	✓	×	3
8	✓	✓	✓	×	×	✓	3
9	✓	✓	✓	×	✓	×	2/3
10	✓	✓	✓	×	✓	×	2

**Each round of coating lasted 3 hours. For example, two rounds of coating means that the m10SBF was replaced with the fresh solution at t=3 h.*

Figure 3.1 shows the influence of surface treatment prior to mineral coating. The SEM images were taken from samples 2, 3, 4, and 5, respectively. The major differences among these samples are that they were pre-treated in different ways: sample 2 was not pretreated, sample 3 was treated with plasma only, sample 4 was treated with plasma and then chitosan, and sample 5 was treated with plasma, chitosan, and then heparin. These samples were then mineralized in the same coating solution for 3 h. While samples 2, 3, and 4 had no or very little mineral deposited on their surfaces, sample 5 had a thick and dense mineral coating. A thick mineral layer was also evident from the apparent increase in fiber diameter. For pristine PLGA nanofibers, the average diameter was ~600 nm. Samples 2, 3, and 4 had approximately the same average diameter. The diameter of sample 5 was increased to ~1 μm. This increase in diameter indicates that the thickness of the

mineral layer was ~200 nm. These results indicate that only a negatively charged surface could induce the nucleation of calcium phosphate on the surface of PLGA nanofibers and facilitate the mineral crystallization and growth.

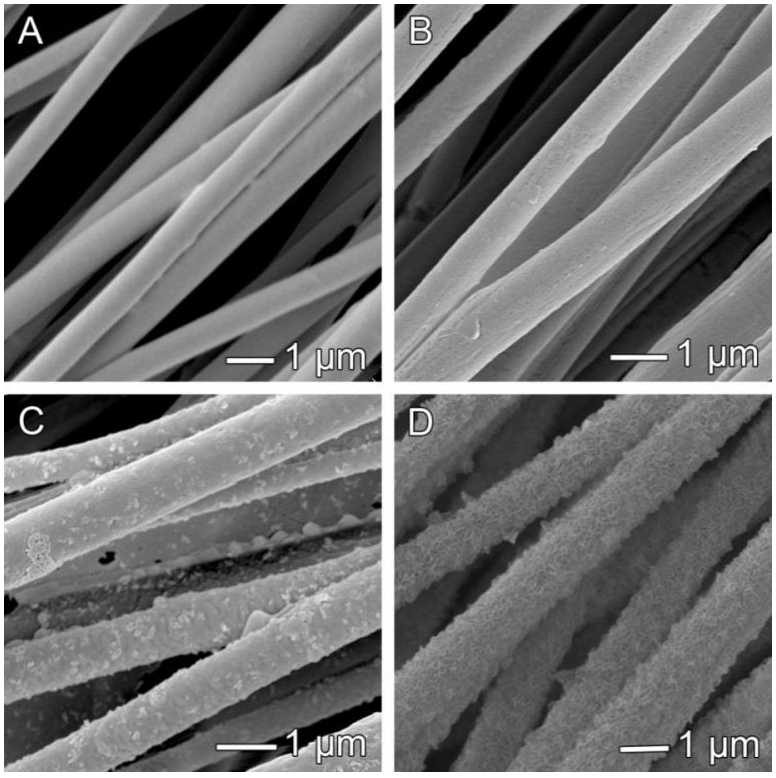

Figure 3.1. *SEM images of PLGA electrospun nanofibers (A) without (sample 2) and (B-D) with different types of surface treatments, followed by immersion in m10SBF (with a concentration of 42 mM for HCO_3^-) for 3 h: (B) treated with plasma (sample 3), (C) treated with plasma and then chitosan (sample 4), and (D) treated with plasma, chitosan, and then heparin (sample 5).*

In Figure 3.1C, the nanofibers were first treated with plasma and then coated with chitosan. Chitosan is likely to be positively charged in the coating solution [13]. Previous studies have demonstrated that a positively charged surface tended to inhibit the nucleation of HA [9]. As a result, the nanofibers in Figure 3.1C were barely coated with HA. The nanofibers in Figure 3.1D were first treated with plasma, and then coated with chitosan and heparin. Heparin is likely to be negatively charged in the solution [13]. A negatively

charged surface promotes the heterogeneous nucleation of HA, leading to a uniform, thick, and dense coating [14]. Heterogeneous nucleation only occurs on the surface of an object when the interaction favors a decrease in the free energy. Anionic groups such as $–COO^-$ brought to the surface of an organic polymer by heparin may, for example, attract Ca^{2+}, resulting in local supersaturation and nucleation of crystallites in the vicinity of the nanofiber and minimization of homogeneous nucleation in the bulk solution. In comparison, the surface of nanofibers in sample 4 was positively charged due to the existence of chitosan, which presents amine groups to the fiber surface thereby inhibiting the precipitation of calcium phosphate on the surface of the scaffold (Figure 3.1C).

3.2 The Influence of HCO_3^- Concentration

The influence of HCO_3^- concentration on mineralization is shown in Figure 3.2. The SEM images were taken from samples 6, 7, and 8. The difference among these samples is the concentration of HCO_3^- in the mineralization solution: 21 mM (sample 6); 42 mM (sample 7); and 63 mM (sample 8). The pH of 10SBF (21 mM) was ~6.1 while the pH of m10SBF (42 mM) was ~6.7. The increase in pH resulting from the additional HCO_3^- could lead to an accelerated rate of HA precipitation. In order to remove this precipitate, I filtered the m10SBF before coating the nanofibers. The concentration of HCO_3^- influenced the grain size, and thus surface roughness of the mineral coating. After incubation in 10SBF containing 21 mM HCO_3^-, plate-like crystals were formed on the fiber surface (Figure 3.2A). When the concentration of HCO_3^- was doubled, there was a significant change in grain size for the mineral coating (Figure 3.2B). The morphology of the mineral coating changed from a plate-like structure to a dense layer with a great reduction in both grain size and surface roughness. After mineralization with an even higher concentration of HCO_3^- in the 10SBF (sample 8), all of the fibers were fully encased in thick mineral sheaths with smooth surfaces (Figure 3.2C). The reduction in grain size may have been due to molecular interactions between the precipitated HA and HCO_3^- ions [14]. Specifically,

the HCO_3^- ions are believed to act as an inhibitor of HA crystal growth in a simulated body fluid. In the absence of growth, nucleation events are favored for HA. The grain size of HA was therefore reduced due to the increased concentration of HCO_3^- in m10SBF [7].

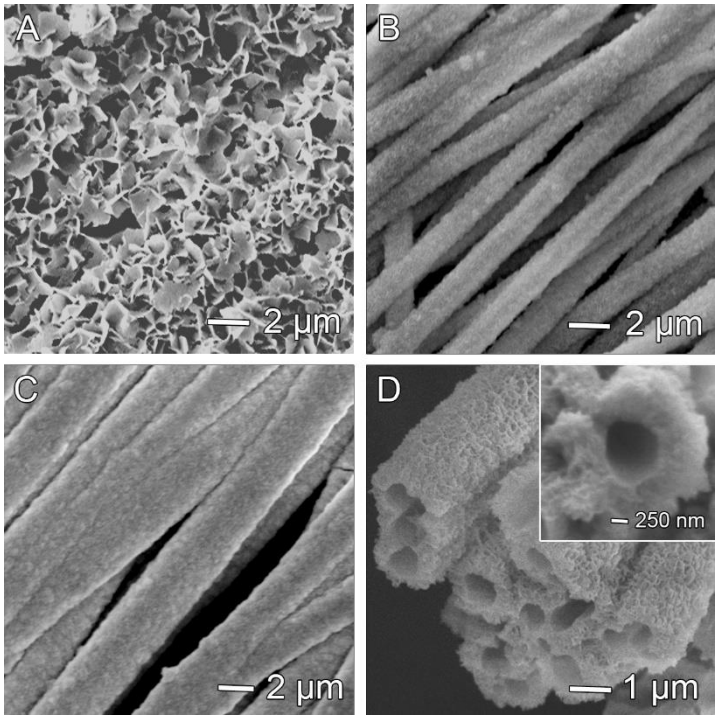

Figure 3.2. *SEM images of PLGA electrospun nanofibers that had been immersed in m10SBF solutions with different concentrations for HCO_3^-: (A) 21 mM (sample 6), (B) 42 mM (sample 7), and (C) 63 mM (sample 8). These samples were all pre-treated with plasma, chitosan and heparin prior to mineral coating. (D) SEM image of tubular structures made of nanocrystalline HA that were obtained by dissolving the PLGA nanofibers (sample 7) in the core.*

To determine the thickness of the mineral coating, sample 7 was immersed in DCM to selectively dissolve the PLGA fibers in the core and obtain tubular fibers made only of the mineral phase (Figure 3.2D). The thickness of these tubes (i.e., the thickness of the mineral coating) was ~420 nm. I then quantified the level of mineral content using an electronic balance and EDX. The mineral content (Ca/(Ca+C)%) increased from 0.5% to 57.7% as the minimization time was increased from 0.5 h to 9 h; at the same time, the mass

percentage of the mineral increased from 0.08% to 3.13% during the course of mineralization for 9 h (Figure 3.3A). As expected, the coating thickness increased from 230 nm to 450 nm with increasing immersion time (Figure 3.3B).

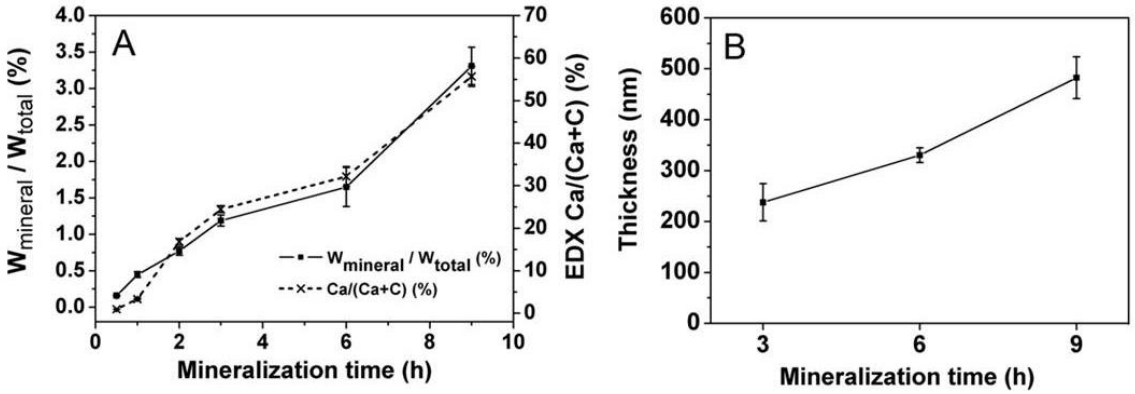

Figure 3.3. *(A) Quantification of the mineral content by EDX and direct weighing measurements, and (B) dependence of the mineral coating thickness on mineralization time.*

3.4 Characterization of the Mineral Coating Produced Using m10SBF

Various characterization tools were employed to better understand the composition and structure of the mineral phase produced using m10SBF (Figure 3.4), including Raman spectroscopy, X-ray diffraction (XRD), transmission electron microscopy (TEM), and high-resolution TEM. A strong peak at 960 cm^{-1} and a medium peak at 1050 cm^{-1} were clearly seen in the Raman spectra for the mineralized nanofibers (Figure 3.4A). These peaks represent symmetric stretching of the phosphate group. It has been reported that peaks in the region of 950-960 cm^{-1} and 1000-1100 cm^{-1}, are characteristic of crystalline HA [15]. The Raman spectra also showed peaks corresponding to the molecular vibrations of the PLGA component, including the C-H (1450 cm^{-1}) and C-COO (875 cm^{-1}) stretch modes of lactic acid.

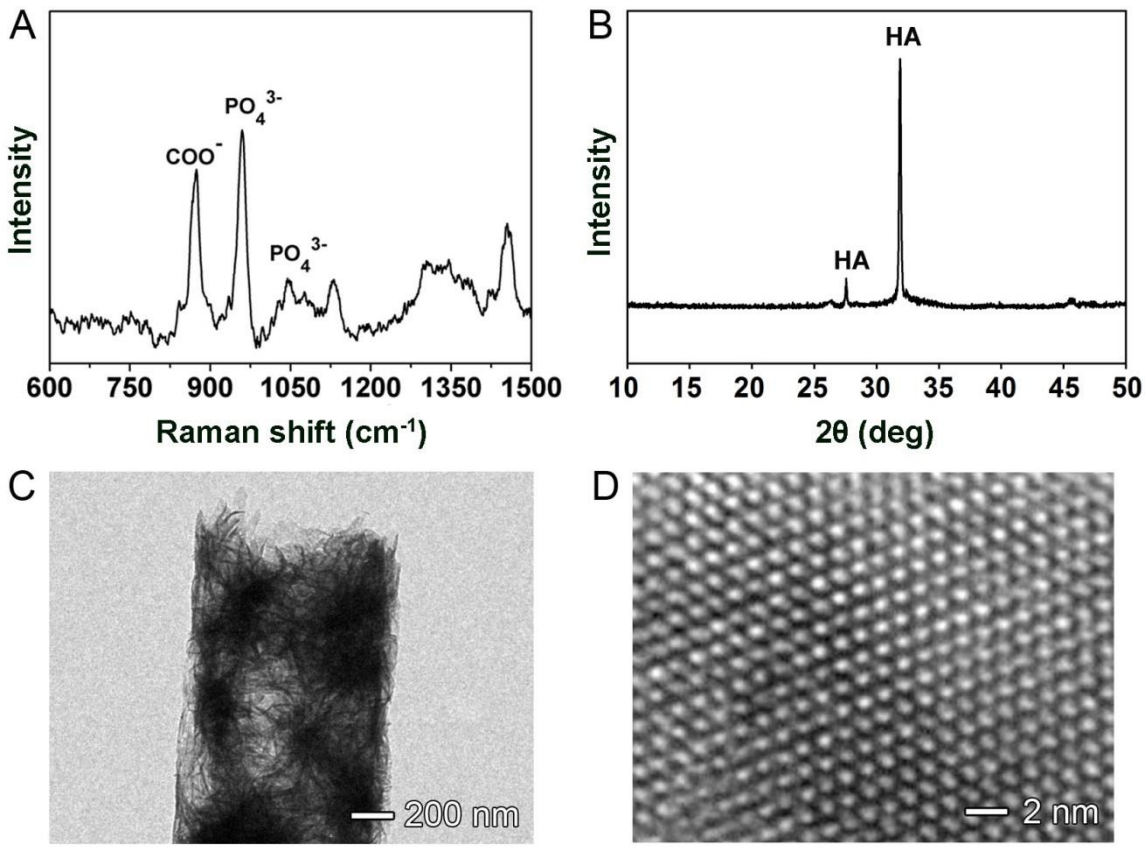

Figure 3.4. *(A) Raman spectrum, (B) X-ray diffraction pattern, (C) TEM image, and (D) high-resolution TEM image taken from sample 7, which was pre-treated with plasma, chitosan, and heparin, followed by immersion in m10SBF for 9 h with change to the fresh solution at t=3 and 6 h.*

XRD was used to investigate the crystal structure of the mineral phase after mineralization in m10SBF for 3 hours. As shown in Figure 3.4B, the XRD pattern only shows peaks for crystalline HA. Figure 3.4C shows a typical TEM image of the HA tube, which was formed by multiple HA grains wrapping tightly together. Figure 3.4D is a high-resolution TEM image, which showed a well-resolved lattice fringe for a single mineral grain. Overall, the mineral produced using m10SBF was mainly HA. These HA grains closely packed together and wrapped around each individual nanofiber to form a thick layer of coating, which in turn increased the stiffness of the scaffold.

3.5 Mechanical Properties of Nanofibers Coated by m10SBF

In terms of mechanical properties, the modulus greatly increased with prolonged coating time, as longer process of mineralization would increase the mineral content in a scaffold (Figure 3.5A). Conversely, the toughness of the scaffolds decreased with prolonged coating time (Figure 3.5B), indicating that the scaffolds had become more brittle (and more bone-like) with longer mineralization time. Despite the increase in stiffness, prolonged coating time did not cause the yield stress to change, implying that the coated mineral did not increase the stress at which permanent deformation began (Figure 3.5C).

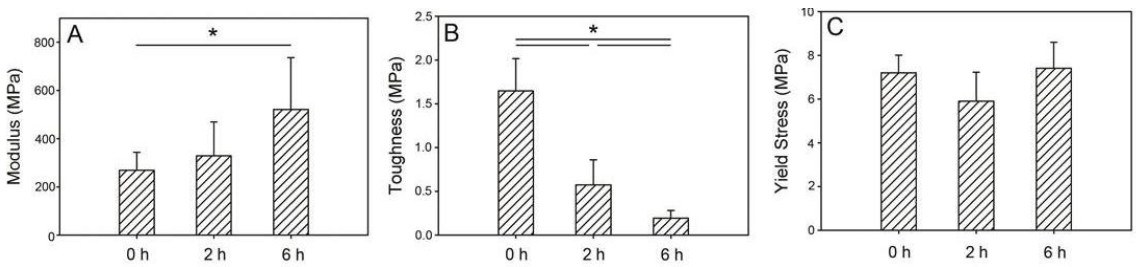

Figure 3.5. *Mechanical testing results for samples mineralized for 0, 2, and 6 h, respectively. (A) Modulus increased with prolonged mineralization time, while (B) toughness (i.e., energy absorption) decreased. (C) Yield stress (i.e., strength) was unchanged during mineralization. (* $p<0.05$)*

These findings demonstrated that the mineral coatings produced using the new m10SBF solution could enhance the stiffness of nanofiber-based scaffolds. For the scaffolds fabricated using the conventional 10SBF, the modulus was only 100 MPa [5]. In comparison, scaffolds coated using m10SBF had a modulus as high as 500 MPa, since the grain size for the mineral coatings was drastically reduced. Specially, increasing the mineralization time had led to an increase in modulus, clearly demonstrating a stiffening effect of the mineral coating.

3.6 Summary

In this chapter, a new type of solution, m10SBF, was developed to coat the surface of electrospun PLGA nanofibers with HA. In a typical procedure, negatively charged heparin was immobilized first, followed by the deposition of HA nanocrystallites through mineralization in m10SBF. I demonstrated that these treatments could facilitate the formation of thick, uniform HA coatings with greatly reduced grain sizes. When compared with scaffolds mineralized using conventional 10SBF, those coated using m10SBF had a significant increase in stiffness.

3.7 Experimental

3.7.1 Materials

PLGA (Mw = 50,000-75,000, lactide:glycolide = 85:15), DCM, DMF, acetic acid, chitosan(low Mw), heparin, 1-ethyl-dimethylaminopropyl carbodiimide (EDC), N-hydroxysuccinimide (NHS), 2-morpholinoethane sulfonic acid (MES), and all the chemicals for preparation of the 10SBF were obtained from Sigma-Aldrich (St. Louis, MO). All of them were used as received.

3.7.2 Fabrication of PLGA Nanofiber Scaffolds by Electrospinning.

The fabrication process is identical to what is described in Section 2.5.2.2.

3.7.3 Pretreatment of PLGA Nanofiber Scaffolds with Chitosan and Heparin

In order to increase the efficiency of immobilizing chitosan and heparin onto the nanofibers, the PLGA surface (typically hydrophobic) was modified by plasma treatment for 8 minutes. The PLGA nanofiber scaffold was then soaked in an aqueous solution containing 0.2% chitosan and EDC/NHS/MES (0.40 g EDC and 0.097 g NHS in 50 mL de-ionized water with 50 mM MES buffer) for 4 h. Afterwards, the sample was transferred

into an aqueous solution of 1% heparin and EDC/NHS/MES for an additional 4 h. Finally, the sample was then washed with de-ionized water and dried in air at room temperature.

3.7.4 Mineralization of Nanofiber Scaffolds Using m10SBF

A supersaturated solution of 10SBF was prepared following the procedure described in Section 2.5.5.3. In order to investigate the role of HCO_3^- in mineralization with the 10SBF, the solution was modified by using three different concentrations for HCO_3^- (m10SBF). In order to remove the impurities, the solutions were filtered through a 0.22 μm pore size filter system. The chitosan- and heparin-coated PLGA scaffolds were then immersed in m10SBF in a capped plastic tube and kept at 37 ºC for 0.5-9 h. The m10SBF solution was changed every 3 h when needed. After removal from m10SBF, the sample was gently washed with water and then dried in air at room temperature.

3.7.5 Structural and Mechanical Property Characterization

The morphologies of the PLGA nanofibers (before and after surface modification with chitosan or heparin) and the PLGA nanofibers after mineralization in m10SBF were examined by SEM (FEI Nova 200 Nanolab). The samples were sputter-coated with gold for 60 s prior to imaging, and an accelerating voltage of 5-15 kV was used.

Samples mineralized for different periods of time (0, 2 and 6 h) were subjected to tensile testing for measurement of their mechanical properties [5]. The scaffold was cut into strips of 3×14 mm^2 in size for uniaxial tensile mechanical testing (N=2-4 per group). The scaffold thickness was measured using a laser micrometer (LK-081, Keyence) while the width was measured from calibrated digital images. The cross-sectional area was calculated as width multiplied by thickness. Mechanical testing was then performed in uniaxial tension under displacement control at a strain rate of ~0.5% per second using a materials testing system (ElectoPuls, Instron). Testing was recorded by video at 1360×1024 resolution at 2.5 fps using a CCD camera (DP70, Olympus). Engineering stress

was calculated as load divided by initial cross-sectional area, and finite strain was determined from image data using custom Matlab (Mathworks, Natick MA) routines. Modulus was calculated as the slope of the linear region of the stress-strain curve. Toughness was calculated as the area under the stress-strain curve, reflecting the energy absorption of the material. Strength was calculated as the maximum stress during the tensile test.

3.8 References

[1] Scadden, D. T. The stem-cell niche as an entity of action. *Nature* **2006**, *441*, 1075-1079.

[2] Pablo Rodríguez, J.; González, M.; Ríos, S.; Cambiazo, V. Cytoskeletal organization of human mesenchymal stem cells (msc) changes during their osteogenic differentiation. *J. Cell. Biochem.* **2004**, *93*, 721-731.

[3] Yourek, G.; Hussain, M. A.; Mao, J. J. Cytoskeletal changes of mesenchymal stem cells during differentiation. *ASAIO J.* **2007**, *53*, 219-228.

[4] McBeath, R.; Pirone, D. M.; Nelson, C. M.; Bhadriraju, K.; Chen, C. S. Cell shape, cytoskeletal tension, and rhoa regulate stem cell lineage commitment. *Dev. Cell* **2004**, *6*, 483-495.

[5] Li, X.; Xie, J.; Lipner, J.; Yuan, X.; Thomopoulos, S.; Xia, Y. Nanofiber scaffolds with gradations in mineral content for mimicking the tendon-to-bone insertion site. *Nano Lett.* **2009**, *9*, 2763-2768.

[6] Veljović, D.; Jokić, B.; Petrović, R.; Palcevskis, E.; Dindune, A.; Mihailescu, I.; Janaćković, D. Processing of dense nanostructured HAp ceramics by sintering and hot pressing. *Ceram. Int.* **2009**, *35*, 1407-1413.

[7] Barrere, F.; Layrolle, P.; Van Blitterswijk, C.; De Groot, K. Biomimetic calcium phosphate coatings on ti_6al_4v: A crystal growth study of octacalcium phosphate and inhibition by Mg^{2+} and HCO_3^-. *Bone* **1999**, *25*, 107S-111S.

[8] Calvert, P.; Mann, S. The negative side of crystal growth. *Nature* **1997**, *386*, 127-129.

[9] Zhu, P.; Masuda, Y.; Koumoto, K. The effect of surface charge on hydroxyapatite nucleation. *Biomaterials* **2004**, *25*, 3915-3921.

[10] Mann, S.; Heywood, B. R.; Rajam, S.; Birchall, J. D. Controlled crystallization of caco 3 under stearic acid monolayers. *Nature* **1988**, *334*, 692-695.

[11] Yamashita, K.; Oikawa, N.; Umegaki, T. Acceleration and deceleration of bone-like crystal growth on ceramic hydroxyapatite by electric poling. *Chem. Mater.* **1996**, *8*, 2697-2700.

[12] Liu, W.; Yeh, Y.-C.; Lipner, J.; Xie, J.; Sung, H.-W.; Thomopoulos, S.; Xia, Y. Enhancing the stiffness of electrospun nanofiber scaffolds with a controlled surface coating and mineralization. *Langmuir* **2011**, *27*, 9088-9093.

[13] Wang, X.; Li, D.; Wang, W.; Feng, Q.; Cui, F.; Xu, Y.; Song, X. Covalent immobilization of chitosan and heparin on PLGA surface. *Int. J. Biol. Macromol.* **2003**, *33*, 95-100.

[14] Chevalier, F.; Lucas, R.; Angulo, J.; Martin-Lomas, M.; Nieto, P. M. The heparin-Ca^{2+} interaction: The influence of the O-sulfation pattern on binding. *Carbohydrate Res.* **2004**, *339*, 975-983.

[15] Nancollas, G. H. The involvement of calcium phosphates in biological mineralization and demineralization processes. *Pure Appl. Chem.* **1992**, *64*, 1673-1678.

CHAPTER 4

GENERATION OF CONTROLLABLE CRIMPS IN NANOFIBERS USING PLASTICIZER-BASED TREATMENT

4.1 Introduction

As discussed in Chapter 1, tendon is a type of highly anisotropic tissue, in which collagen fibrils are assembled into highly ordered, parallel bundles and aligned along the long axis of the tissues [1]. This anatomic structure serves to transmit the forces generated by muscle contraction directly to the skeleton with a minimal loss of energy [2-4]. In addition to packing in parallel bundles, the collagen fibrils exhibit a characteristic crimping pattern that results in non-linear stiffening of the tissue with increasing tensile strain [5-7]. These crimped structures are capable of absorbing more strain than straight fibers, and consequently serve to buffer mechanical loads generated by the attached muscles or bones [3]. Furthermore, the crimp produces a spring-like mechanism that protects the muscle from tearing during contraction [8, 9]. Although much progress has been made in producing biomaterials that match the strength and stiffness of the native tendon and ligament [10-12], little effort has been focused on reproducing the non-linear stiffening behavior for native tissues that is driven by the crimped microstructure. Since electrospun nanofibers can be readily collected as aligned arrays, they represent a promising class of scaffolds for repairing tendon injuries [13]. In this Chapter, I will discuss a new method for generating crimps in nanofibers using plasticizer-based treatment to recapitulate the crimped microstructure in tendon.

Several approaches have been developed to generate crimps in nanofibers. For example, Wang *et al.* produced bicomponent nanofibers through side-by-side electrospinning of two different polymer solutions [14]. A curly morphology was observed when the diameters of the fibers were relatively thick, which can be attributed to the uneven

stretching of the two materials during electrospinning. Amsden *et al.* demonstrated that nanofibers could be introduced to crimp when electrospun at a temperature higher than the polymer's glass-transition temperature (T_g). The residual stresses retained in the fibers would cause the nanofibers to shrink upon removal from the collecting mandrel [15]. Magnetic-field-assisted electrospinning was also reported to be capable of generating crimps in nanofibers when a high flow rate was used for electrospinning [16]. All these approaches involve the introduction of residual stress into the fibers during the generation process, which was later released, allowing the nanofibers to crimp. Although these techniques can be used to fabricate crimped nanofibers for various potential applications, the degree of crimping could not be effectively controlled, compromising the full potential of such structures.

In this chapter, I developed a simple method for generating crimps in fibers by exploiting the interaction between a polymer and a plasticizer. Ethanol was used as a plasticizer to treat poly(lactic acid) (PLA) fibers and induce the formation of crimps. PLA is a widely used material in tissue engineering scaffolds due to its inherent biodegradability [17]. Electrospun nanofibers were first collected as uniaxially aligned arrays to mimic the anisotropic anatomy of the tendon [18]. During electrospinning, the fibers are continuously stretched by a combination of forces, including the electrostatic force in the electric field and the repulsion force among the charges accumulated on them. These forces generate a significant residual stress in the polymer chains composing each fiber and lead to elongation of the chains along the long axes of the nanofiber [19, 20]. My hypothesis is that upon contact with ethanol, the chains will release the residual stress by returning a conformation with lower energy. As a result, crimps will be generated in the nanofibers.

4.2 Generating Controllable Degrees of Crimping in PLA Nanofibers

Since crimping in each individual nanofiber will cause the sheet to shrink, the degree of crimping for the nanofibers can be controlled by varying the degree of shrinkage

for the nanofiber sheets. PLA was first electropun onto a rotating mandrel to obtain a sheet of uniaxially aligned nanofibers. The sheet was then cut into multiple strips of 1×5 cm^2 in size. The nanofibers were aligned in longitudinal direction of the strips. The schematic of the ethanol treatment procedures is shown in Figure 4.1. The original length of the strips was denoted as "L_0". Prior to ethanol treatment, the two edges perpendicular to the alignment were fixed at various distances, as denoted by "L". When $L=L_0$, the samples maintained their original length after ethanol treatment; When $L<L_0$, the samples were initially at slack, but took L as their new length after ethanol treatment.

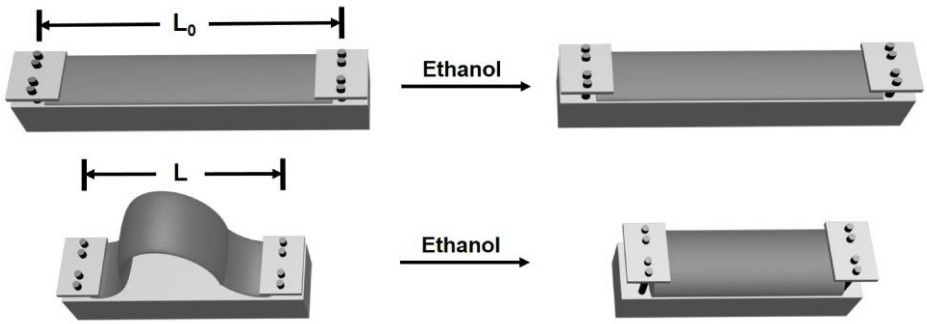

Figure 4.1. *Schematic showing the procedures for ethanol treatment.*

Figure 4.2A shows a SEM image of pristine PLA nanofibers. Figure 4.2, B-E show the SEM images of samples treated with ethanol at L/L_0=100%, 75%, 50%, and 25%, respectively. Samples treated at L/L_0=100% had no crimp whereas samples treated at L/L_0=25% had substantial crimps. A decreasing trend in wavelength (*i.e.*, an increasing trend in degree of crimping) can be visualized in Figure 4.2, B to E. The minimum length a PLA strip can take after treatment with ethanol is around 10% of its original length. In Figure 4.2F, the wavelength and the amplitude of the crimps were plotted against L/L_0. Depending the value of L/L_0, the wavelengths of the crimps could be tuned from ~100 μm to ~10 μm, while the amplitudes remained between 3-10 μm. In addition to crimping upon ethanol treatment, the nanofibers also became thicker.

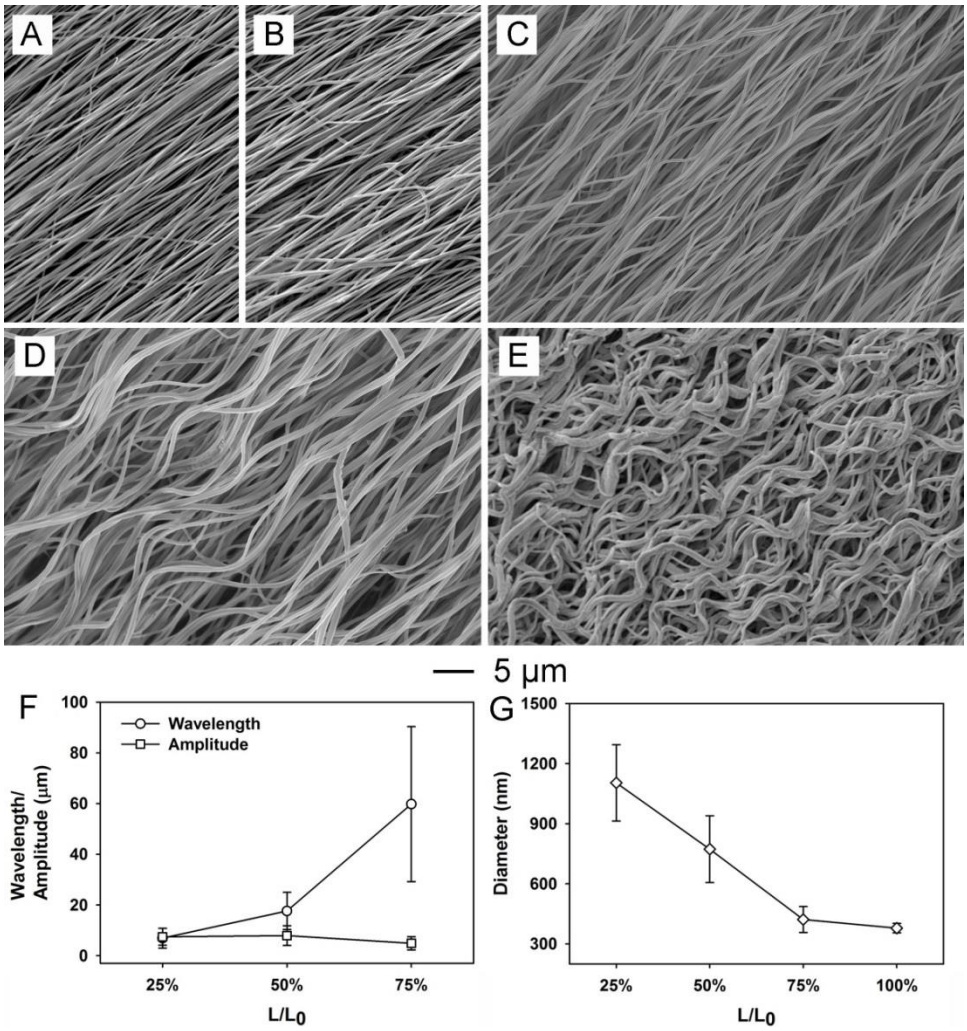

Figure 4.2. *SEM images showing (A) pristine PLA nanofibers, (B-E) PLA nanofibers treated using ethanol at (B) L/L_0=100%, (C) L/L_0=75%, (D) L/L_0=50%, and (E) L/L_0=25%. The degrees of crimping were controlled by varying the value of L/L_0. (F) Plot showing the relationship between wavelength/amplitude of the crimped nanofibers and L/L_0. The wavelength was positively correlated with the value of L/L_0, while the amplitude of the crimp remained unchanged (N=100). (G) Plot showing the relationship between diameter of the crimped nanofibers and L/L_0 (N=100). The diameter was negatively correlated with the value of L/L_0.*

As shown in Figure 4.2G, the diameter of the nanofibers increased from ~350 nm for pristine samples to over 1 μm for fibers treated at L/L_0=25%. This phenomenon

supports the initial hypothesis that crimping is generated upon contact with ethanol by retraction of the elongated polymer chains inside each nanofiber.

Ethanol was also effective for generating crimps in fibers composed of copolymers and polymer blends containing PLA. As shown in Figure 4.3, A and B, fibers composed of PLGA (copolymer of PLA) and PCL/PLA blends also became crimped upon treatment with ethanol. Similarly, crimps were generated using other polymer/plasticizer combinations, such as polyvinylidene fluoride (PVDF) and DMF. Figure 4.3C shows that the PVDF nanofibers became crimped after soaking in DMF.

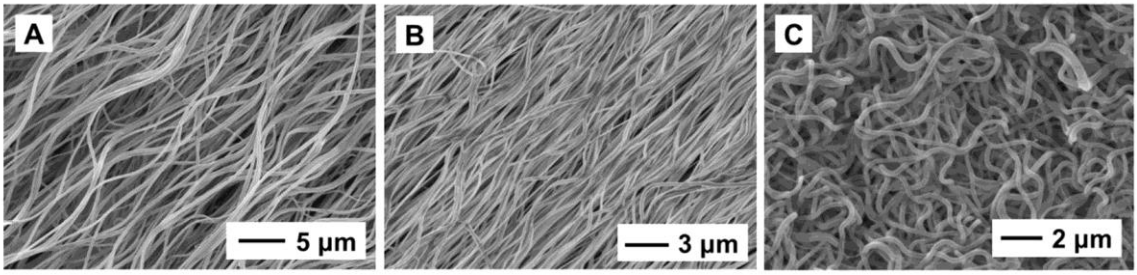

Figure 4.3*. SEM images showing crimped nanofibers composed of (A) PLGA (85:15), (B) PCL/PLA blends after treatment with ethanol, and (C) PVDF after treatment with DMF.*

4.3 Mechanistic Study of the Interaction between Ethanol and PLA

In order to investigate the mechanisms underlying the structural and mechanical changes to PLA nanofibers treated with ethanol, Raman spectroscopy and differential scanning calorimetry (DSC) analysis were performed. Figure 4.4A shows the Raman spectra for pristine nanofibers, samples treated at L/L_0=100%, and samples treated at L/L_0=50%. Many characteristic peaks were observed, and their assignments were discussed in previous literature [21]. The spectra of samples treated at L/L_0=100% and 50% differed most dramatically in the 400 cm^{-1} region. These differences can be attributed to changes in the polymer chain conformation. Bands between 415 and 398 cm^{-1} are assigned to an in plane bending vibration for the carbon-carbonyl backbone. The band at 410 cm^{-1}

is strongly affected by chain conformation whereas that at 397 cm^{-1} is not [22]. Specifically, the intensity of the band at 410 cm^{-1} increases with increasing crystallinity and can therefore be assigned to the crystalline phase, whereas the intensity of the band at 397 cm^{-1} is not affected by crystallinity. The relative intensity between these two bands therefore indicates the level of crystallinity. Figure 4.4A shows that the intensity of the band at 397 cm^{-1} did not differ among pristine samples, samples treated at L/L_0=100%, and samples treated at L/L_0=50%. However, the intensity of the band at 410 cm^{-1} was higher in samples treated at L/L_0=100% and lower in samples treated at L/L_0=50%, as compared to the pristine sample. These results indicate that the crystallinity was increased in samples treated at L/L_0=100% and decreased in samples treated at L/L_0=50%. These observations supported a mechanism by which PLA polymer chains release residual stress during ethanol treatment, leading to increased crystallinity if the initial length is maintained or crimping if the length is not constrained.

The chain conformation or crystallinity of the samples was also analyzed using the intensity of the cold crystallization peak through DSC analysis. A cold crystallization peak appears when an amorphous polymer sample is heated slowly above its T_g. This occurs because crystalline structures are formed when the molecules have sufficient kinetic energy to start crystal growth [23, 24]. This phenomenon occurs in the range of temperature between T_g and the melting point (T_m). The degree of crystallinity, χ, can be calculated as the following:

$$\chi = \frac{\Delta H_f - \Delta H_c}{\Delta H_f^\circ} \times 100\%$$

where ΔH_f is the heat of fushion, ΔH_c is the heat of cold crystallization, and ΔH_f° is the heat of fusion for 100% crystalline PLA, which is 93 J/g [25]. The intensity of the cold crystallization peak is therefore negatively correlated with the crystallinity of the sample. Three major peaks were observed in the DSC spectra for pristine PLA nanofibers, samples treated at L/L_0=50%, and samples treated at L/L_0=100% (Figure 4.4B), representing T_g,

cold crystallization temperature (T_c), and T_m, from left to right, respectively. The samples treated at L/L_0=50% had a large cold crystallization peak at 85.3 ºC. The crystallinity calculations for pristine nanofibers, samples treated at L/L_0=50%, and samples treated at L/L_0=100% were 8.8%, 1.7%, and 32.2%, respectively. Not surprisingly, nanofibers treated at L/L_0=100% showed the highest crystallinity, as the polymer chains released their residual stress but not allowed to retract. In other words, the energy released by the fibers during treatment was used to increase the crystallinity when the length was constrained. In contrast, when the length was not constrained, as in the case for samples held slack at L/L_0=50%, the energy released by the fibers during treatment was converted to fiber retraction and generation of a crimped morphology.

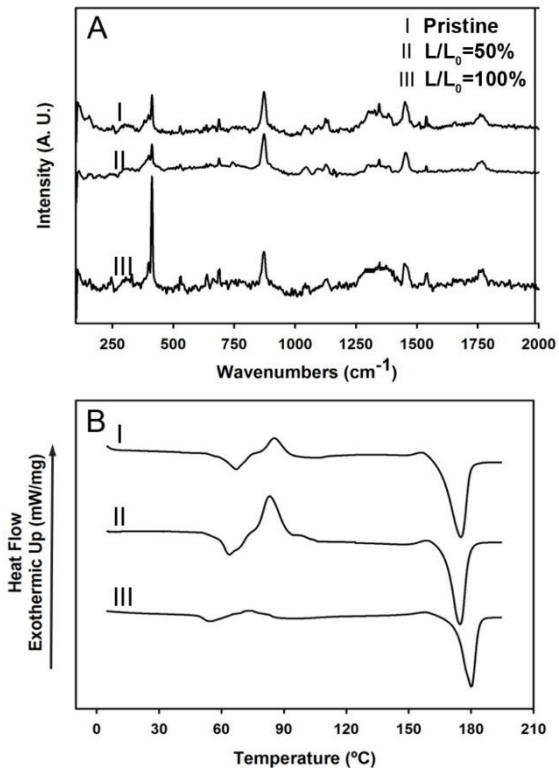

Figure 4.4. *(A) Raman spectra and (B) DSC curves of the pristine PLA nanofibers, samples treated at L/L_0=50%, and samples treated at L/L_0=100%.*

To further examine the energy released by the nanofibers upon treatment with ethanol, force was measured when the samples were immersed in de-ionized water to ethanol, respectively (Figure 4.5). A rise of force was observed during treatment, reaching a plateau after ~1 minute. The maximum force was reached rapidly for the samples soaked in ethanol (9.8 ± 2.5 sec), and rose to a value of 0.13 ± 0.05 N. The stress produced during ethanol treatment was ~16% of the ultimate stress of the pristine nanofibers. In contrast, no obvious change in force was observed for samples submerged in de-ionized water only.

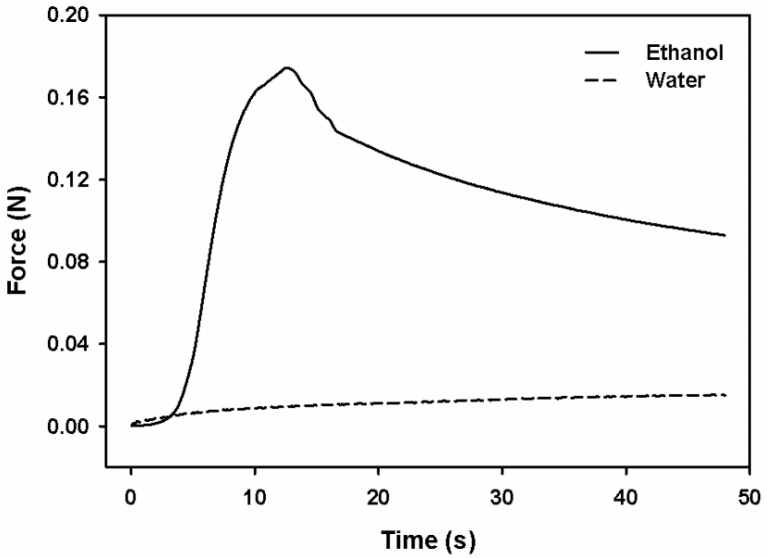

Figure 4.5. *Forces generated by the PLA nanofibers when the samples were immersed in ethanol or de-ionized water.*

4.4 Mechanical Testing

The crimped nanofibers demonstrated many of the mechanical characteristics of native tendon tissue. Specifically, the crimped nanofibers obtained using ethanol treatment at L/L_0=50% displayed a stress-strain curve that included a non-linear toe region, followed by a linear region prior to yield. The toe region in these samples ended at a strain of ~0.075 (Figure 4.6). In contrast, uncrimped nanofibers that were treated with ethanol at L/L_0=100%

and the pristine fibers had toe regions that ended at strains of ~0.005 and ~0.02, respectively. When comparing these three samples, the stress-strain curves were distinct.

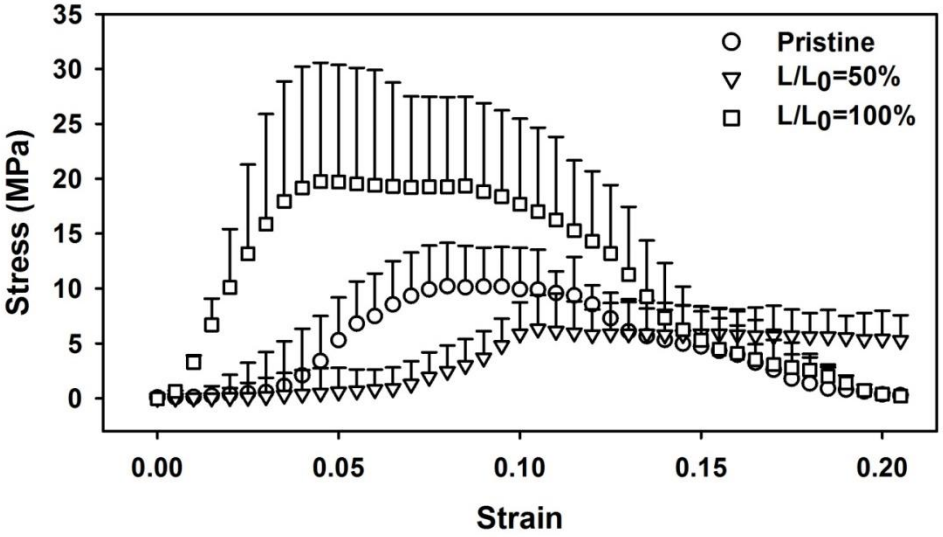

Figure 4.6. *Stress-strain curves for for pristine PLA nanofibers, sample treated with ethanol at L/L_0=50%, and sample treated at L/L_0=100%. N =12 for each group.*

Figure 4.7 compares the mechanical properties of pristine nanofibers with those obtained through ethanol treatment at L/L_0=50% and 100%. Samples treated at L/L_0=100% had the highest modulus and strength, but the lowest yield strain (Figure 4.7, A and B). The significantly higher modulus for the samples treated at L/L_0=100% is consistent with an increase in crystallinity, as modulus and crystallinity are positively correlated (Figure 4.7A) [26]. In contrast, crimped samples treated at L/L_0=50% had the lowest modulus but the highest yield strain, which is defined as the maximum strain a sample can reach before deforming plastically. Prior to the yield point, material deformation is reversible; a deformed material and will return to its original shape when the applied stress or strain is removed. Figure 4.7B shows that the yield strains were 5%, 4%, and 11% for nanofibers annealed at pristine nanofibers, samples treated at L/L_0=100%, and samples treated at L/L_0=50%, respectively. As shown in Figure 4.7, C and D, samples treated at L/L_0=100%

also had the highest toughness and ultimate stress, as compared to the pristine nanofibers and the samples treated at L/L_0=50%.

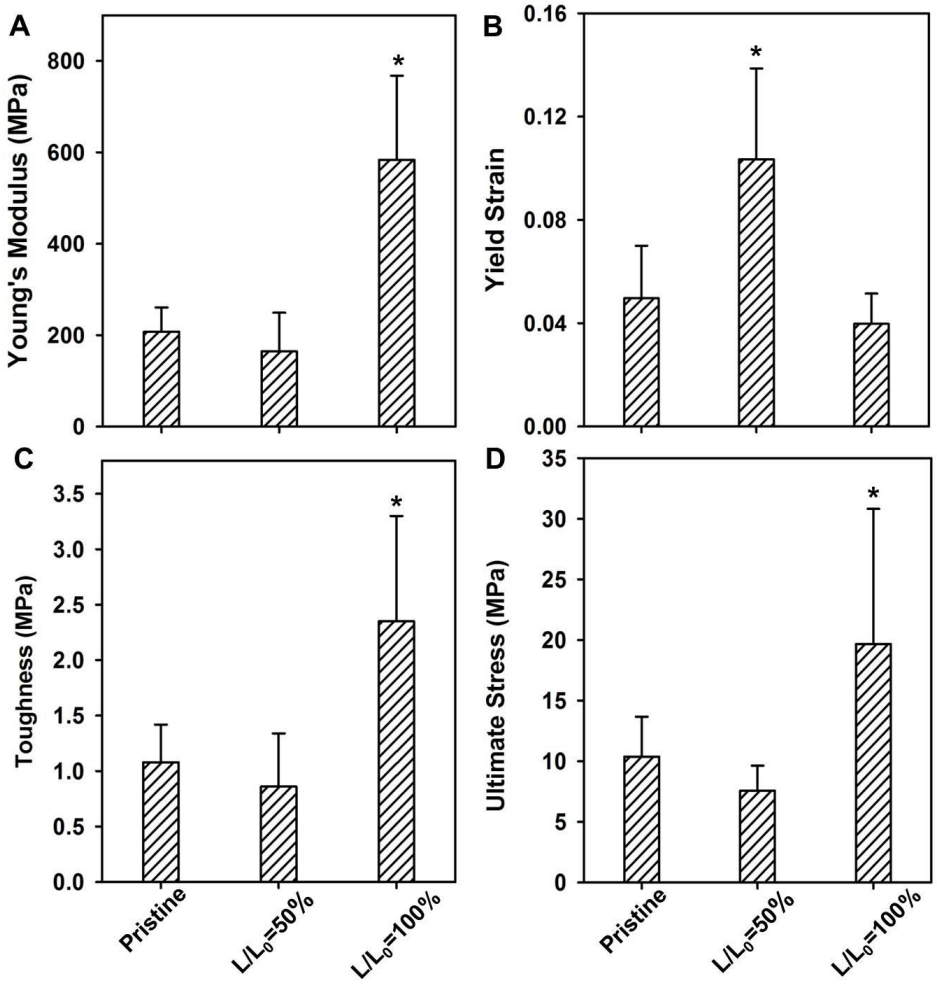

Figure 4.7 *Tensile mechanical testing demonstrating (A) Young's modulus, (B) yield strain, (C) toughenss, and (D) ultimate stress for pristine PLA nanofibers, samples treated at L/L_0=50%, and L/L_0=100%. N = 12 for each group, significance indicated by the * above the bars as compared with the pristine nanofibers ($p<0.05$).*

The higher yield strain in the nanofiber samples annealed at L/L_0=50% was likely a result of the crimp microstructure in the nanofibers. Removal of crimp results in the non-linear toe region observed in native tendon under tension, an important mechanical feature

of soft connective tissues [27, 28]. A relatively low yield strain, as seen in pristine nanofiber scaffolds and uncrimped nanofiber scaffolds treated at L/L_0=100%, may predispose scaffolds to pre-mature rupture in the *in vivo* setting. Crimped nanofiber scaffolds, on the other hand, have a yield strain comparable to native tendon, and may therefore be a better class of scaffolds for repairing soft connective tissues. The toughness and ultimate stress of samples treated at L/L_0=100% were also the highest among the three groups due to its increased crystallinity, while no significant difference were observed between pristine nanofibers and samples treated at L/L_0=50%.

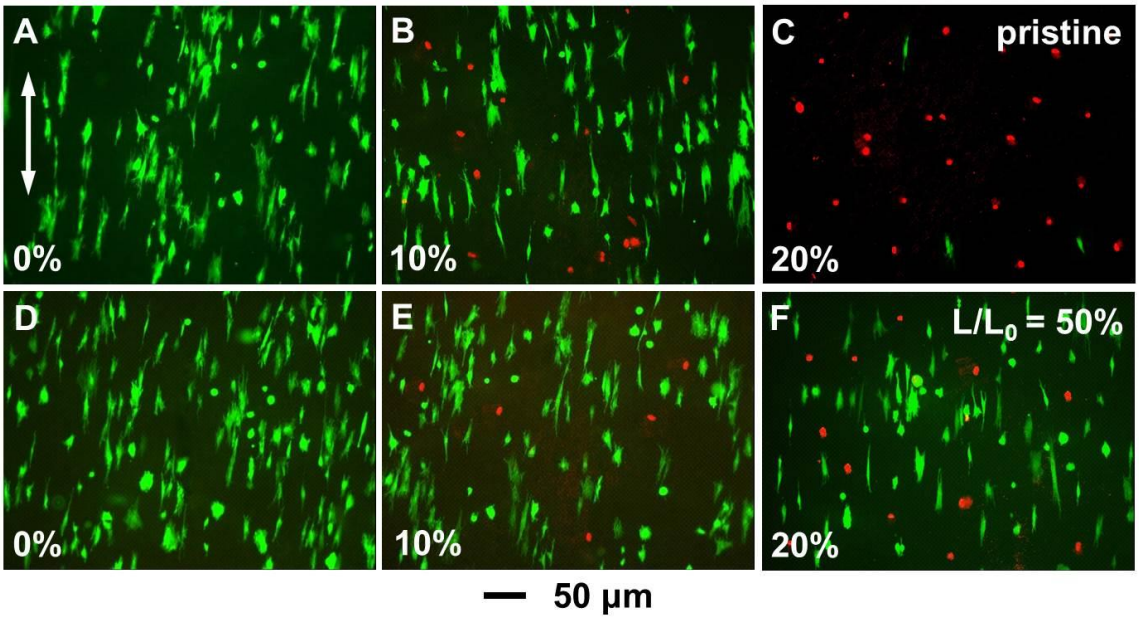

Figure 4.8. *Live/dead staining of the TFBs cultured on (A-C) pristine nanofibers and (D-F) crimped nanofibers treated at L/L_0=50%. The alignment of the nanofibers is indicated by the arrow in (A). The TFBs in (B) and (E) were subjected to 10% strain and remained alive, exihibiting a slightly elongated morphology. The TFBs in (C) and (F) were subjected to 20% strain. While most of the cells died in (C), majority of the cells in (F) stayed alive, suggesting that cells cultured on the crimped nanofibers had a higher tolerance on strain.*

To further demonstrate the advantages of crimped nanofibers in repairing the soft connective tissues such as tendon, I cultured TFBs on pristine nanofiber and crimped nanofibers treated at L/L_0=50%. After allowing attachment for 48 hours, samples in both groups were subjected to static tensile stretching for 24 hours. Live/dead staining was performed to evaluate the viability of the cells (Figure 4.8). Initially, all the cells were stained alive as shown Figure 4.8, A and D. In the pristine group, ~87% of the cells remained viable after the samples were subjected to 10% strain (Figure 4.8B) while this number decreased to ~7% as the stain went up to 20% (Figure 4.8C). A large portion of TFBs even de-attached from the scaffolds as pristine nanofibers ruptured at 20% strain. In the L/L_0=50% group, TFBs assumed a more polar morphology in Figure 4.8E at 10% strain while ~91% remained viable. When the strain increased to 20%, in Figure 4.8F, ~80% of the cells stayed alive. There results indicate that TFBs cultured on crimped nanofibers have a much higher tolerance on strain.

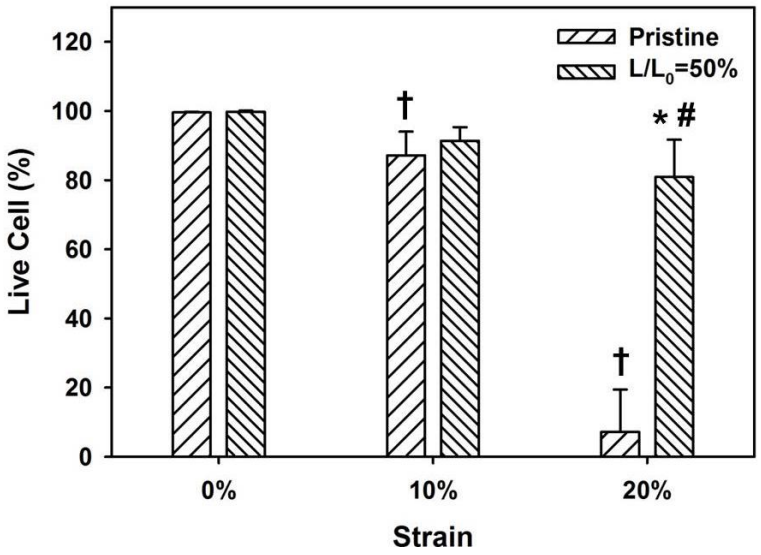

Figure 4.9. *Quantification of live TFBs cultured on pristine nanofibers and crimped nanofiber treated at L/L_0=50% under various strain (N =20). *, †, and # indicate significantly difference ($p<0.05$) between pristine and L/L_0=50% groups at the same strain, within pristine group compared with 0% strain, and within L/L_0=50% group compared with 0% strain, respectively.*

Viability quantification of the TFBs in both groups under various strains is shown in Figure 4.9. Aligned nanofibers with crimps *i)* mimic the anisotropic anatomy of the tendon; *ii)* exihibit non-linear stiffening behavior with increasing tensile strain to recapitulate the mechanical characteristics of the native tendon tissue; *iii)* protects TFBs from strain tearing, are therefore a type of scaffold more advantageous than pristine aligned nanofibers for tendon regeneration.

4.5 Summary

In this chapter, I demonstrated the use of ethanol treatment to generate crimps in electrospun PLA nanofibers. By controlling the length that the scaffolds could take after ethanol treatment, the residual stress was converted either into increased crystallinity (leading to increased modulus for the nanofibers) or longitudinal contraction (leading to crimps). TFBs cultured on the crimped nanofibers showed a higher mechanical tolerance upon strain than those cultured on the pristine, aligned nanofibers. Taken together, the nanofibers with crimps constitute a novel type of scaffolds for tendon and soft connective tissue repair.

4.6 Experimental

4.6.1 Electrospinning

Electrospinning solution was prepared by dissolving 1.25 g PLA (Mw=75,000) was dissolved in 10 mL hexafluoro-2-propanol (HFIP). The solution was loaded into a 5 mL plastic syringe with a 23 ½-gauge needle attached, and dispensed using a syringe pump. The injection rate was 0.5 mL/h. The fibers were collected using a rotating mandrel at a speed of 2 m/s. The distance between the tip of needle and the collector was about 20 cm, and a voltage of 15 kV was applied. All the samples were imaged using a Zeiss Ultra-60 FE-SEM at an accelerating voltage of 5 kV.

4.6.2 Raman Spectroscopy and DSC Analysis

The Raman spectra were recorded using a Thermo Almega XR Micro and Macro Raman Analysis System. The excitation wavelength used was 488 nm. Backscattered Raman signals were collected on a CCD detector. The power of the laser was 20 mW, and the acquisition time was 2 s. The thermal behavior of PLA nanofiber was characterized by DSC (Q2000, TA instrument) in a temperature range from 0°C to 200°C at a heating rate of 20°C/min.

4.6.3 Mechanical Testing

Uniaxial tensile tests were performed using an Instron Electropuls E1000 with custom grips, and analyzed using custom code written in Matlab. Samples from all three groups were cut into testing strips of 1×3 cm^2 in size, with the nanofibers aligned parallel to the longitudinal direction. Untested portions of the scaffold were measured for their thickness using a Keyence LK-081 laser micrometer, and the average value was taken as the thickness of the sample. These samples also were used to calculate the apparent density of the scaffolds using their mass and estimated volume. Samples were tested under uniaxial tension at quasi-static conditions, with a constant strain rate of 0.1% per second along the direction of alignment.

4.6.4 Testing of Force Generation during Ethanol Treatment

Tests were performed to measure the forces produced by PLA nanofiber scaffolds when they were immersed in ethanol or de-ionized water (as control). All the testing strips were held at their original length during the tests. Samples were first placed between magnetic frames for preservation of their initial dimensions during handling and mounting. The frames were mounted onto thin film grips and placed in a container connected to an Instron EPuls E1000 for force measuring. Two of the edges parallel to the alignment were

cut off from the frame to eliminate any force they could contribute. Ethanol or de-ionized water was then quickly added into the container. Force was measured for 50 seconds, with the grips held stationary. The force data was then analyzed by low-pass filtering.

4.6.5 Cell Culture and Live/dead Staining

TFBs were maintained in Dulbecco's modified eagle medium (DMEM) (Invitrogen) supplemented with 10 vol% FBS (Invitrogen) and 1 vol% P/S (Invitrogen) till 80% confluency. Scaffolds were prepared as 5×1 cm^2 strips with the alignment parallel to the shorter edge (1 cm), and attached to 90 mm petri-dishes using medical adhesive (Fisher). Scaffolds were sterilized under UV for 30 min prior to cell seeding. The cultures were kept in an incubator at 37 °C under a humidified atmosphere containing 5% CO_2 for 48 h for cell adhesion. The scaffolds were then mounted onto a home-made device to stretch the scaffolds to 10% or 20% strain. The cells were maintained under static tension for 24 h prior to live/dead staining.

See Section 2.5.5.6 for live/dead staining procedures.

4.6.6 Statistics

Results are presented in the form of mean ± standard deviation, with "N" indicating the number of samples per group. Comparison between groups was performed using the one-way ANOVA and the difference was considered significant for $p<0.05$. Tukey's post-hoc test was used for all pair-wise comparisons and significance was attained at $p<0.05$. Statistical analyses were performed with Systat 13 (Crane Software International, Chicago, IL).

4.7 References

[1] Kastelic, J.; Galeski, A.; Baer, E. The multicomposite structure of tendon. *Connect. Tissue Res.* **1978**, *6*, 11-23.

[2] Franchi, M.; Fini, M.; Quaranta, M.; De Pasquale, V.; Raspanti, M.; Giavaresi, G.; Ottani, V.; Ruggeri, A. Crimp morphology in relaxed and stretched rat achilles tendon. *J. Anat.* **2007**, *210*, 1-7.

[3] Franchi, M.; Trirè, A.; Quaranta, M.; Orsini, E.; Ottani, V. Collagen structure of tendon relates to function. *Sci. World J.* **2007**, *7*, 404-420.

[4] Zhang, G.; Young, B.; Ezura, Y.; Favata, M.; Soslowsky, L.; Chakravarti, S.; Birk, D. Development of tendon structure and function: Regulation of collagen fibrillogenesis. *J. Musculoskelet. Neuronal Interact.* **2005**, *5*, 5-21.

[5] Hansen, K. A.; Weiss, J. A.; Barton, J. K. Recruitment of tendon crimp with applied tensile strain. *J. Biomech. Eng.* **2002**, *124*, 72-77.

[6] Kastelic, J.; Palley, I.; Baer, E. A structural mechanical model for tendon crimping. *J. Biomech.* **1980**, *13*, 887-893.

[7] Magnusson, S.; Qvortrup, K.; Larsen, J. O.; Rosager, S.; Hanson, P.; Aagaard, P.; Krogsgaard, M.; Kjaer, M. Collagen fibril size and crimp morphology in ruptured and intact achilles tendons. *Matrix Biol.* **2002**, *21*, 369-377.

[8] Scott, S. H.; Loeb, G. E. Mechanical properties of aponeurosis and tendon of the cat soleus muscle during whole-muscle isometric contractions. *J. Morphol.* **1995**, *224*, 73-86.

[9] Muramatsu, T.; Muraoka, T.; Takeshita, D.; Kawakami, Y.; Hirano, Y.; Fukunaga, T. Mechanical properties of tendon and aponeurosis of human gastrocnemius muscle *in vivo*. *J. Appl. Physiol.* **2001**, *90*, 1671-1678.

[10] Kumbar, S.; James, R.; Nukavarapu, S.; Laurencin, C. Electrospun nanofiber scaffolds: Engineering soft tissues. *Biomed. Mater.* **2008**, *3*, 034002.

[11] Sahoo, S.; Ouyang, H.; Goh, J. C.-H.; Tay, T.; Toh, S. Characterization of a novel polymeric scaffold for potential application in tendon/ligament tissue engineering. *Tissue Eng.* **2006**, *12*, 91-99.

[12] Moffat, K. L.; Kwei, A. S.-P.; Spalazzi, J. P.; Doty, S. B.; Levine, W. N.; Lu, H. H. Novel nanofiber-based scaffold for rotator cuff repair and augmentation. *Tissue Eng. A* **2008**, *15*, 115-126.

[13] Li, D.; Wang, Y.; Xia, Y. Electrospinning of polymeric and ceramic nanofibers as uniaxially aligned arrays. *Nano Lett.* **2003**, *3*, 1167-1171.

[14] Lin, T.; Wang, H.; Wang, X. Self-crimping bicomponent nanofibers electrospun from polyacrylonitrile and elastomeric polyurethane. *Adv. Mater.* **2005**, *17*, 2699-2703.

[15] Surrao, D. C.; Hayami, J. W.; Waldman, S. D.; Amsden, B. G. Self-crimping, biodegradable, electrospun polymer microfibers. *Biomacromol.* **2010**, *11*, 3624-3629.

[16] Liu, Y.; Zhang, X.; Xia, Y.; Yang, H. Magnetic-field-assisted electrospinning of aligned straight and wavy polymeric nanofibers. *Adv. Mater.* **2010**, *22*, 2454-2457.

[17] Drumright, R. E.; Gruber, P. R.; Henton, D. E. Polylactic acid technology. *Adv. Mater.* **2000**, *12*, 1841-1846.

[18] Goh, J. C.-H.; Ouyang, H.-W.; Teoh, S.-H.; Chan, C. K.; Lee, E.-H. Tissue-engineering approach to the repair and regeneration of tendons and ligaments. *Tissue Eng.* **2003**, *9*, 31-44.

[19] Zong, X.; Kim, K.; Fang, D.; Ran, S.; Hsiao, B. S.; Chu, B. Structure and process relationship of electrospun bioabsorbable nanofiber membranes. *Polymer* **2002**, *43*, 4403-4412.

[20] Kakade, M. V.; Givens, S.; Gardner, K.; Lee, K. H.; Chase, D. B.; Rabolt, J. F. Electric field induced orientation of polymer chains in macroscopically aligned electrospun polymer nanofibers. *J. Am. Chem. Soc.* **2007**, *129*, 2777-2782.

[21] Kister, G.; Cassanas, G.; Vert, M. Effects of morphology, conformation and configuration on the IR and Raman spectra of various poly(lactic acid)s. *Polymer* **1998**, *39*, 267-273.

[22] Kang, S.; Hsu, S. L.; Stidham, H. D.; Smith, P. B.; Leugers, M. A.; Yang, X. A spectroscopic analysis of poly (lactic acid) structure. *Macromolecules* **2001**, *34*, 4542-4548.

[23] Wunderlich, B. Theory of cold crystallization of high polymers. *J. Chem. Phys.* **1958**, *29*, 1395-1404.

[24] Kulinski, Z.; Piorkowska, E. Crystallization, structure and properties of plasticized poly(L-lactide). *Polymer* **2005**, *46*, 10290-10300.

[25] Pyda, M.; Bopp, R.; Wunderlich, B. Heat capacity of poly (lactic acid). *J. Chem. Thermodyn.* **2004**, *36*, 731-742.

[26] Crist, B. The ultimate strength and stiffness of polymers. *Annu.Rev. Mater. Sci.* **1995**, *25*, 295-323.

[27] Lynch, H. A.; Johannessen, W.; Wu, J. P.; Jawa, A.; Elliott, D. M. Effect of fiber orientation and strain rate on the nonlinear uniaxial tensile material properties of tendon. *J. Biomech. Eng.* **2003**, *125*, 726-731.

[28] Hirokawa, S.; Tsuruno, R. Three-dimensional deformation and stress distribution in an analytical/computational model of the anterior cruciate ligament. *J. Biomech.* **2000**, *33*, 1069-1077.

CHAPTER 5

THE OUTGROWTH AND MATURATION OF NEURONS DERIVED FROM EMBRYONIC STEM CELLS

5.1 Introduction

As discussed in Chapter 1, electrospun nanofibers are emerging as a platform for neural tissue engineering because they can be readily aligned to create anisotropic topographies, closely mimicking the anatomy of the nerves [1-3]. For improved regeneration, the nanofiber scaffolds can be delivered in combination with certain types of cells with therapeutic effects [4-7], since the loss of functional neurons is the main cause of most disorders in the nervous system [8, 9]. In addition, traumatic injuries to the nervous system often result in the nearly irreversible deprivation of neurons [10]. Current clinical procedures can address the symptoms but are inadequate in halting the neuronal death and rescuing, or regenerating, the cellular functions [11-14].

Many cell sources have been investigated by researchers for their therapeutic effects. Among these sources, ESCs represent one of the most promising candidates. ESCs display pluripotency and can divide rapidly *in vitro,* providing a sufficient number of cells for *in vivo* implantation within a reasonable time frame [15-18]. Many groups have explored the use of ESC-derived neurons for treating various neurological disorders. For example, Mckay *et al.* reported that the ESCs could efficiently generate midbrain precursors and dopamine neurons *in vitro* and extend axons into the host striatum to form moderately functional synaptic connections in a rat model of Parkinson's disease [19]. Jessell *et al.* showed that ESCs-derived motor neurons could be used to treat amyotrophic lateral sclerosis (ALS) by implanting them into the spinal cords of chick embryos. ESC-derived neurons could populate the embryonic spinal cord, extending axons and forming

synapses with target muscles 7 days post implantation [20]. Results from these studies have established the foundation of ESC transplantation.

To date, numerous studies have demonstrated that aligned nanofibers can guide neurites to extend along the fibers in the direction of alignment (parallel outgrowth) [21-24]. However, rarely were the investigations devoted to understanding the interactions between neurites and nanofibers mechanistically. Our group has recently piloted a study to understand how the interaction between neurites and nanofibers could affect the outgrowth patterns of the neurites derived from dorsal root ganglia (DRG) [25]. Although it was generally believed that DRG neurites would extend along the nanofibers [23, 26-28], our group observed, for the first time, that DRG neurites could also grow along a direction perpendicular to the aligned nanofibers [25]. During studies, I also observed a similar behavior for neurites derived from EBs (spherical aggregates of ESCs), which inspired me to perform the research described in this chapter.

Herein, I will first discuss the different patterns of outgrowth for neurites derived from EBs on nanofibers with different properties (e.g., fiber density and hydrophilicity, among others), followed by some preliminary mechanistic studies. Since EBs need to be dissociated into single neurons for delivery purposes, I also investigated the outgrowth patterns and maturation of individual neurons derived from ESCs.

5.2 Outgrowth Patterns of Neurites Projected from EBs

5.2.1 The Effect of Fiber Density on Neurite Outgrowth

I first investigated the effects of the density of uniaxially aligned PCL nanofibers on neurite outgrowth emanating from EBs. The fiber density was controlled by varying the collection time. The samples were sterilized with 70% ethanol prior to seeding with EBs. Figure 5.1, A-C shows the density of nanofibers when collected for 1, 2, and 15 min, respectively. Figure 5.1D shows the relationship between numbers of fibers per mm and collection time.

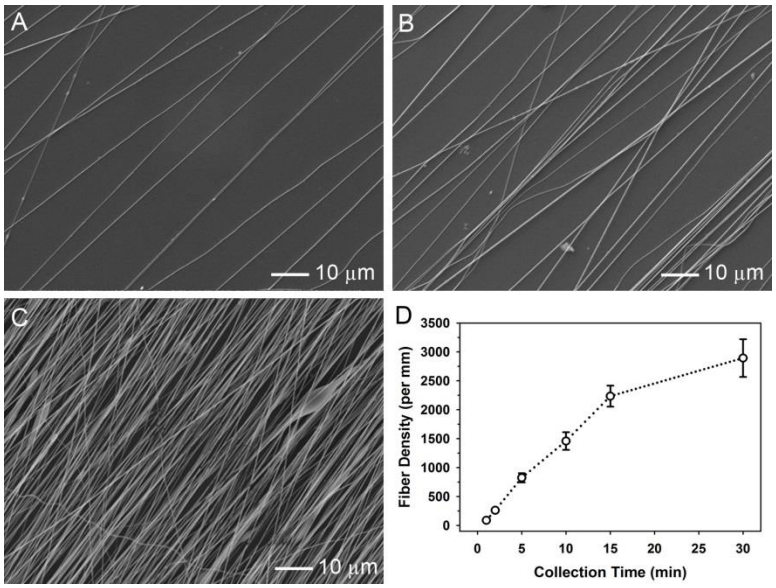

Figure 5.1. *(A-C) Typical SEM images of nanofibers which were collected for 1, 2, and 15 min, respectively. (D) Fiber densities at different fiber collection times [23].*

Figure 5.2 shows typical neurite fields projected from EBs seeded on aligned nanofibers with different fiber densities. Few neurites emanated from EBs on fibers with very low densities (collected for 1 min), together with no clear trend for the outgrowth direction (Figure 5.2A). Some neurites grew parallel to the direction of alignment while others grew perpendicularly. Additionally, the length of the neurites growing on scaffolds with a very low density of fibers was much shorter compared to those growing on denser counterparts (Figure 5.2, B-D). Contrary to most previous reports, the majority of neurites grew perpendicularly to the direction of fiber alignment indicated by the arrow in Figure 5.2A. EBs cultured on uniaxially aligned nanofibers were imaged by SEM after dehydration. Figure 5.3A clearly shows that the neurites extending from the EBs were perpendicular to fiber alignment. Figure 5.3B shows the enlarged view of the neurites in Figure 5.3A.

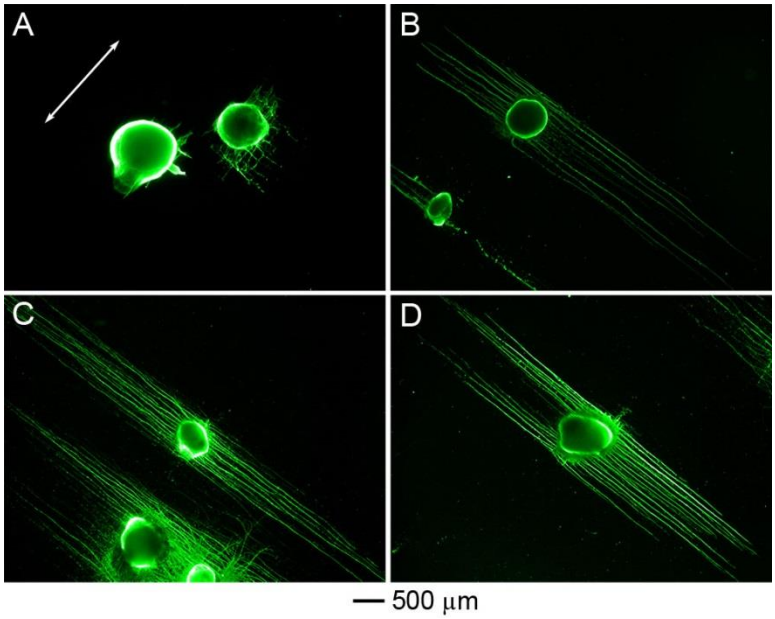

Figure 5.2. *Fluorescence micrographs showing typical neurite fields projected from EBs seeded on scaffolds consisting of uniaxially aligned nanofibers with different densities. The white arrow indicates the direction of fiber alignment. The scaffolds with different nanofiber densities were obtained with the deposition time of (A) 1 min, (B) 3 min, (C) 5 min and (D) 10 min. Neurites preferred to grow perpendicularly to the fiber alignment at all examined fiber densities, except for the case when the fiber density was too low to support significant neurite outgrowth.*

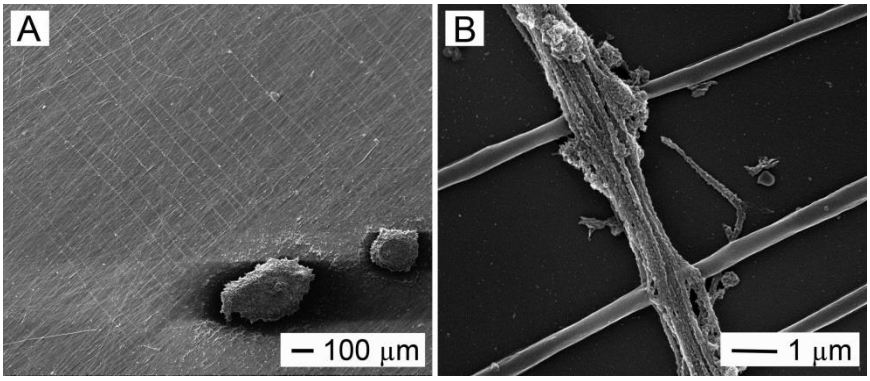

Figure 5.3. *SEM images of neurites projecting from EBs on electrospun PCL nanofibers. (A) overview of the perpendicular outgrowth of neurites extending from EBs. (B) Enlarged view of the neurites in (B).*

Previous studies have demonstrated that uniaxially aligned nanofibers can direct neurite outgrowth along the direction of the fiber alignment. Neurites emanating from various types of cells, including DRG, hippocampal neurons, PC12, *xenopus* spinal neurons, and c17.2 neural stem cell-derived neurons were reported to be extending parallel to the alignment [26, 29-31]. It is noteworthy that the substrates used in these studies were modified in some ways. For example, in one of our previous studies, only parallel outgrowth of the neurites emanating from EBs was observed. This is because the samples used in previous study were sterilized *via* ethylene oxide (EtO) treatment, which would oxidize the backbone of PCL molecules into carbonyl species and increase the hydrophilicity of the substrates [32]. The substrates used in Figure 5.2 were pristine PCL nanofibers, whose hydrophilicity were much lower than those treated with EtO. As a result, the neurites adopted a pattern of perpendicular outgrowth instead. These observations indicate that the direction of neurite outgrowth is closely related to the extent of hydrophilicity of nanofibers. Since increasing the hydrophilicity of the nanofibers often leads to better adhesion between cells and their substrates [33-35], it is reasonable for me to assume that the pattern of neurite outgrowth on nanofibers is determined by the strength of adhesion between the two. The next section will therefore be focused on the investigation of the outgrowth patterns of the neurites projecting from EBs cultured on substrates with different surface modifications.

5.2.2 The Effect of Surface Modification on Neurite Outgrowth

In this section, I further examined the outgrowth of neurites on PCL nanofibers with two different types of alignments–uniaxial and radial–and different degrees of hydrophilicity. SEM images of the nanofibers with these two alignments are shown in the insets of Figure 5.4, A and D, respectively. The nanofibers were obtained by collecting for 10 min, sterilized with 70% ethanol overnight. Nanofibers used in Figure 5.4, A and D were pristine, while those in Figure 5.4, B and E, and Figure 5.4, C and F were treated with

air plasma for 10 min and 20 min, respectively. As shown in Figure 5.4, A-C, the neurites exhibited perpendicular outgrowth on the pristine fibers, a mixed pattern of parallel and perpendicular outgrowth on fibers treated for 10 min, and parallel growth on fibers treated for 20 min. This phenomenon can be explained by taking into consideration of their difference in surface properties (*i.e.*, hydrophilicity and cell adhesion). Similar trends of outgrowth were observed for EB-derived neurites cultured on radially aligned nanofibers (Figure 5.4, D-F), which were fabricated using a procedure described in our previous publication [36]. It is worth noting that the neurites tended to grow along a curve as they attempted to project perpendicularly to radial alignment (Figure 5.4, D and E). It appears that neurites can accommodate variations in local topography and change direction accordingly during projection.

It was demonstrated that oxygen-containing groups, including –OH and –C=O, on the surface of PCL nanofibers increased during plasma treatment, resulting in an increase in hydrophilicity and enhancement of biological performance (*i.e.*, cell adhesion and proliferation) [37]. The direction of neurite outgrowth appears to be mainly determined by the surface properties of the fibers. Interaction between cells and the substrates can also be enhanced by coating the nanofibers with adhesive molecules in the ECM, such as fibronectin and laminin. As a result, the neurites also exhibited a pattern of parallel outgrowth on fibronectin and laminin coated nanofibers. Additionally, neurites can grow in an arc on radially aligned nanofibers, meaning that neurite are very sensitive to local topography and capable of making adjustments accordingly.

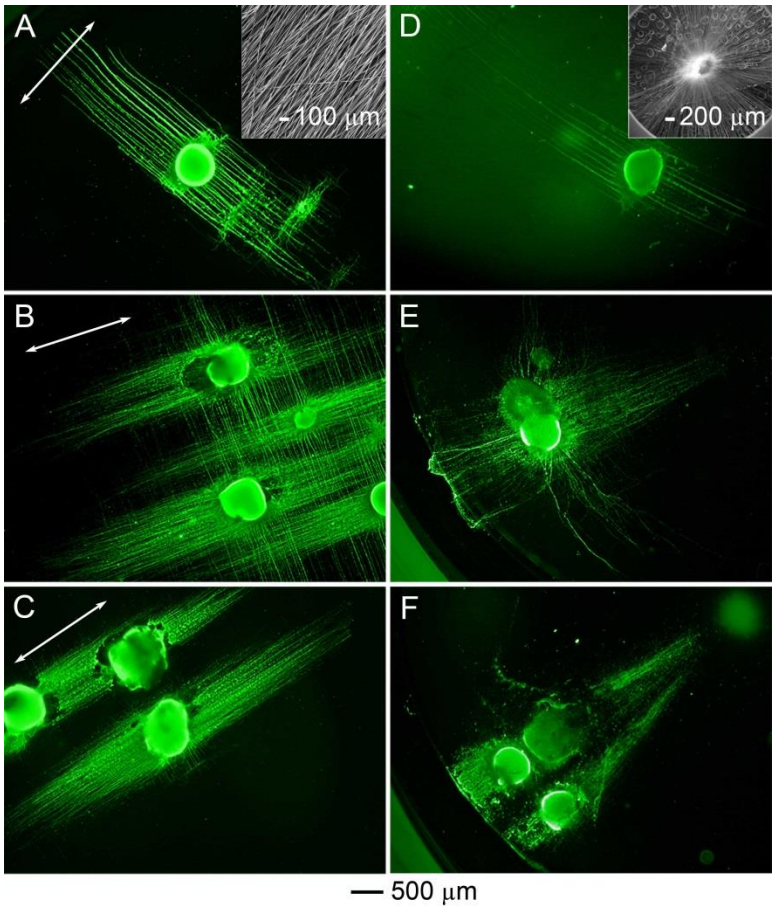

Figure 5.4. *Fluorescence micrographs showing the outgrowth patterns of neurites projected from EBs on (A-C) uniaxially and (D-F) radially aligned nanofibers, as determined by their surface properties. (A, D) pristine nanofibers, (B, E) fibers treated with plasma for 10 min, and (C, F) fibers treated with plasma for 20 min. Insets show SEM images of (A) uniaxially aligned nanofibers and (D) radially aligned nanofibers. The arrows indicate the direction of uniaxially-aligned nanofibers.*

5.2.3 The Pharmacological Effect on the Neurite Outgrowth

The outgrowth patterns of neurites on various types of scaffolds described in Section 5.2.2 collectively suggest that the projecting behavior of neurites is most likely mediated by adhesion mechanism. When neurites adhere tightly to nanofibers, they tend exihibit parallel outgrowth; when the adhesion is relatively weak, neurites prefer to adhere to each other and fasciculate by forming bundles to reduce their contact area with the

nanofibers. At the same time, the filopodia at the tip of the growth cone keeps exploring its vicinity by grasping onto the nanofibers and pulls itself forward by extending perpendicularly to the alignment. In order to validate this hypothesized mechanism, EBs were cultured on uniaxially-aligned PCL nanofibers in the presence of a number of different chemical species in the medium. All scaffolds were fabricated with a collection time of 10 min. According to the observations in Figure 5.1D, neurites should extend perpendicularly to the alignment in the normal culture medium. However, it appeared that neurites extending from EBs cultured on nanofibers in the presence of blebbistatin, an inhibitor of myosin II, mainly presented parallel growth (Figure 5.5A), suggesting that myosin II may play some role in perpendicular outgrowth. Growth cones rich in actin microfilaments have the potential to interact with myosin II, a member of the myosin family of molecular motors that drives the transportation of actins [38]. It has been reported that myosin II isoforms played an important role in cellular adhesion through modulation of the interaction between integrin receptors and the extracellular matrix [39]. Inhibition of myosin II would result in impairment of neuronal growth cone motility due to its involvement in retrograde flow and actin filament organization [40, 41]. When the neurites are extending perpendicularly, the growth cone is in an "exploring" mode, which requires very high motility so that it can protrude and retract in a timely fashion. Inhibiting the phosphorylation of myosin II in the presence of blebbistatin will therefore lead to parallel outgrowth.

When EBs were cultured on fibers in the presence of Y27632, a specific inhibitor of Rho-associated kinase (ROCK), neurites projecting from EBs mainly exhibited perpendicular growth (Figure 5.5B). ROCK inhibits the depolymerization of actin filaments, and therefore leads to their stabilization and an increase in numbers. The increased number of stable actin filaments and the reduction in actin monomers contribute to a reduction of cell migration. Therefore, in the presence of Y27632, the growth cones maintained their mobility and exhibited perpendicular outgrowth mainly. In the presence

of anti-neural cell adhesion molecules (anti-NCAM), most of the neurites displayed parallel growth, with a few of them grew perpendicularly (Figure 5.5C). NCAM is a homophilic binding glycoprotein expressed on the surface of neurons which regulates the cell-cell adhesion between neurons. When it is inhibited, the cell-cell interaction between neurites will be weakened. The adhesion between cell and substrate becomes comparable to that between cells, so a significant portion of neurites switch to parallel instead. Meanwhile, few neurites were able to sprout when cultured in the presence of anti-neurofascin (Figure 5.5D). Neurofascin is a member of the L1 subgroup of the Ig superfamily and involved in axon subcellular targeting and synapse formation during neural development. It promotes axon outgrowth through interactions with NCAM [42, 43]. Anti-neurofascin seemed to have an overall effect in inhibiting neurite extension.

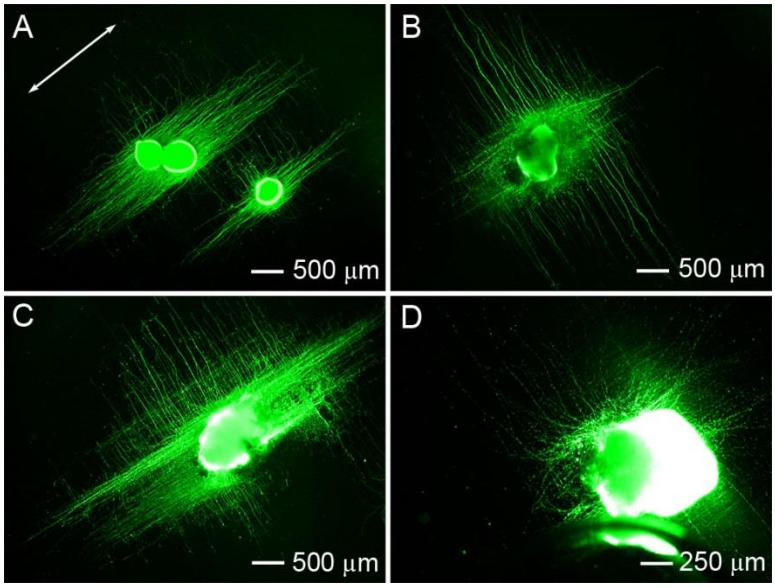

Figure 5.5. *Fluorescence micrographs showing typical neurite fields projecting from EBs cultured on uniaxially-aligned nanofibers in the presence of (A) blebbistatin (50 μg/mL), (B) Y27632 (10 μM), (C) anti-NCAM (50 μg/mL), and (D) anti-neurofascin (50 μg/mL). The arrow indicates the direction of uniaxially-aligned nanofibers.*

The mechanisms of neurite navigation on aligned fibers are not yet fully understood. Pharmacological studies found that myosin II and NCAM may play a partial role in perpendicular growth. It is known that the directional extension of neurites is a result of traction force exerted by filopodia. When the neurites are extending perpendicularly, the growth cones of neurites may grasp the fibers, applying force to the fibers and pulling the neurites forward (Figure 5.6) [44].

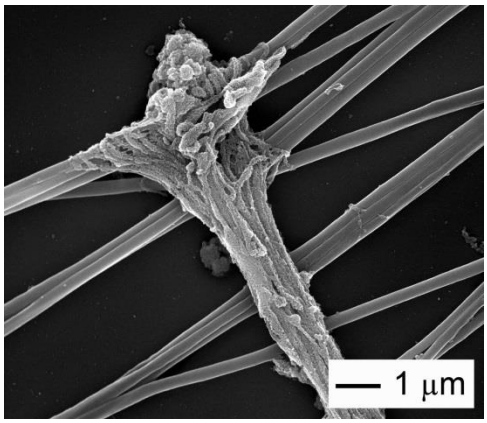

Figure 5.6. *SEM images showing that neurites extending from the EBs could grasp the fibers during their extension process.*

5.3 Outgrowth and Maturation of Neurons Derived from Dissociated EBs

As clusters of cells, EBs are not directly deliverable to the injured site. Therefore, understanding the outgrowth patterns of neurons derived from dissociated EBs is of pivotal significance for the successful application of aligned electrospun nanofibers as scaffolds to facilitate nerve regeneration. In addition to projecting neurites, the maturation of neurons on nanofiber scaffolds also remains to be explored. Therefore, this Section is divided into two parts: *i*) outgrowth patterns of neurons derived from dissociated EBs and *ii*) functional characterization of their maturation.

5.3.1 Outgrowth Patterns of Neurons Derived from Dissociated EBs

Individual neurons were obtained by trypsinizing EBs. Typically, 1×10^5 cells were seeded in each well of a 24-well plate containing aligned nanofibers. Superimposed fluorescence images of DAPI and Tuj1 staining were shown in Figure 5.7, A and B. When seeded on pristine nanofibers, the neurites preferentially perpendicular outgrowth (Figure 5.7A). The direction of alignment was indicated by the arrow. When seeded on nanofibers that were treated with plasma for 20 min, the pattern switched to parallel outgrowth (Figure 5.7B). These observations were consistent with those observed for EBs in Section 5.2. Figure 5.7, C and D shows the superimposed image of nanofibers in brightfield and neurites with Tuj1 staining in fluorescence.

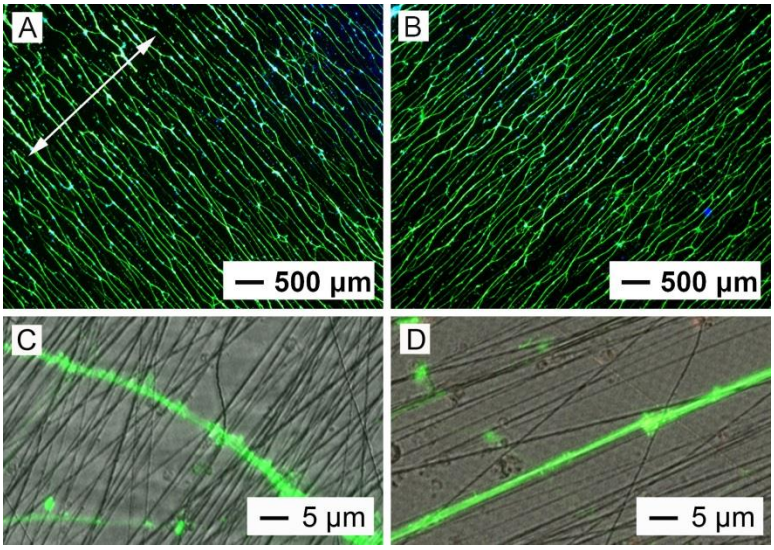

Figure 5.7. *Fluorescence micrographs showing outgrowth of neurons derived from dissociated EBs. (A, C) perpendicular outgrowth when cultured on pristine nanofibers and (B, D) parallel outgrowth when cultured on nanofibers treated with air plasma for 20 min. Cell nuclei were stained with DAPI in blue, neurites were stained with Tuj1 in green.*

5.3.2 Functional Characterization of Neurons Derived from Dissociated EBs

In order to examine the functions of neurons derived from dissociated EBs, I first measured the extracellular action potentials of a sampling neuron. Action potentials are

generated by voltage-gated ion channels embedded in the cell membrane [45]. These channels are shut at resting potential. When there is an increase in membrane potential, these channels rapidly open and allow an inward flow of sodium ions, which in turn produces a further rise in the membrane potential and causes more channels to open. The ions flowing across the cell membrane result in electrical currents in the resistive extracellular volume around the neuron. These currents establish dynamic electrical field changes which can be sensed with an extracellular recording electrode [45].

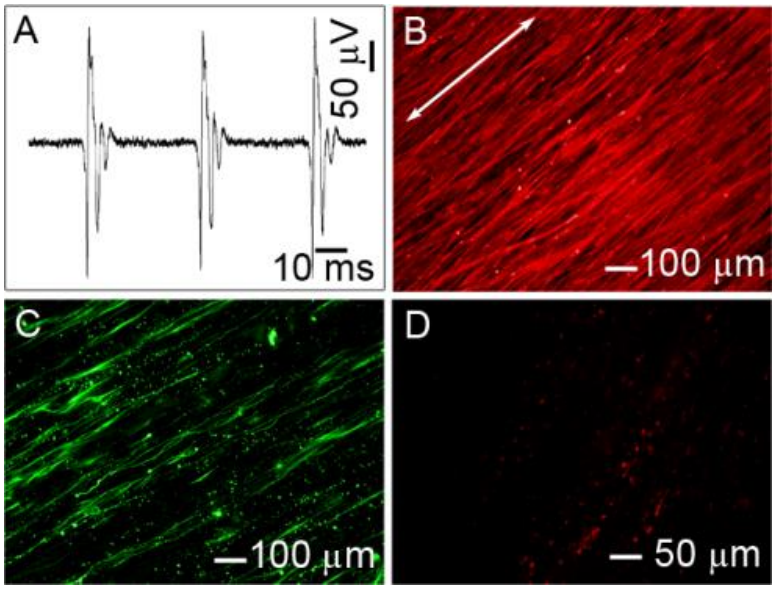

Figure 5.8. *Functional characterization of the neurons derived from dissociated EBs. (A) Typical recordings of a mature neuron. (B) Fluorescence images showing F-actin staining of myotubes on aligned nanofibers. (C) Fluorescence images showing Tuj1 staining of neurons derived from dissociated EBs, which were seeded on top of myotubes. (D) Fluorescence images showing α-bungaratoxin staining for the acetylcholine clusters. Neuromuscular junctions were formed between the neurons and the myotubes during co-culture.*

Figure 5.8A shows the recording of a typical extracellular action potential of a mature neuron derived from dissociated EBs. To further assess the functions of the neurons, I developed a system to investigate the formation of neuromuscular junctions by co-

culturing them with myoblasts. Myoblasts were cultured on aligned nanofibers for the first 3 days, after which the proliferation medium was substituted with the differentiation medium. After 5 days in differentiation medium, myotubes formed. Neurons derived from dissociated EBs were seeded on the top of the myotubes in a neural basal medium with B27 as a supplement. Figure 5.8B shows F-actin staining of myotubes. It was seen that myotubes were aligned along the direction of fiber alignment, in line with the previous reports. Figure 5.8C shows Tuj1 staining of neurites seeded on top of myotubes. Neurites preferentially oriented in a parallel way along the myotubes on the uniaxially aligned fibers. Figure 5.8D shows α-bungaratoxin staining for acetylcholine receptors, which were distributed along fiber alignment on uniaxially aligned fibers. After 7 days, myotubes started to contract when co-cultured with neurons derived from dissociated EBs. It is noteworthy that the direction of myotube contraction was in line with the direction of fiber alignment for uniaxially aligned scaffolds. These results indicated that aligned nanofibers can direct not only the outgrowth of neurons derived from dissociated EBs, but also the orientation of the neuromuscular junctions, which in turn determines the contraction direction of the muscles.

5.4 Summary

In this chapter, I first elaborated on controlling the outgrowth patterns of the neurites emanating from EBs on uniaxially aligned electrospun nanofibers. Depending on the strength of adhesion, neurites can extend either along the nanofibers (when the adhesion is strong), or in the direction perpendicular to the alignment (when the adhesion is weak). The pharmacological effects of blebbistatin, Y27632, anti-NCAM, and anti-neurofacscin supported this hypothesized mechanism. In the second part, I demonstrated that neurons derived from dissociated EBs were able to mature on aligned electrospun nanofibers, as the neurons were capable of emitting a complete action potential and forming neuromuscular junctions with muscle cells.

5.5 Experimental

5.5.1 Fabrication of Electrospun Nanofibers

The electrospinning setup and the collector used for fabricating and collecting uniaxially and radially aligned nanofibers are similar to those used in our previous studies [36, 46, 47]. PCL was dissolved in a mixture of DCM and DMF (Fisher), at a volume ratio of 80:20) to obtain a 20% (w/v) solution. A staple collector and a metal ring with a needle at the center-were employed to collect nanofibers with uniaxial and radial alignment, respectively. Following electrospinning, the aligned fiber samples were transferred to glass cover slips and then fixed using medical adhesive (Dow Corning co., Midland, Mi, USA). The PCL fibers were sputter-coated with gold before imaging with SEM (NOVA 200 nanolab, FEI, Oregon, USA) at an accelerating voltage of 15 kV. Samples prepared for cell culture were inserted into a 24-well tissue culture polystyrene (TCPS) and sterilized with 70% ethanol.

5.5.2 Culture of ESCs and Formation of EBs

The protocols for ESC culture and EB formation was adapted from previous publications [17, 18]. RW4 mouse ESCs were obtained from Dr. David I. Gottlieb's lab (Washington University School of Medicine) and cultured in T25 culture flasks coated with a 0.1% gelatin solution (Sigma-Aldrich, St. Louis, MO) in the presence of 1000 U/mL leukemia inhibitory factor (LIF; Chemicon, Temecula, CA) and 10^{-4} M β-mercaptoethanol (BME; Invitrogen, Grand Island, NY) to maintain their undifferentiated state. Cells were cultured in complete media consisting of DMEM (Invitrogen) supplemented with 10% new born calf serum, 10% FBS (invitrogen), and 0.3 mM of each of the following nucleosides: adenosine, guanosine, cytosine, thymidine, and uridine (Sigma-Aldrich), and passaged at a ratio of 1:4 every two days.

Undifferentiated ESCs were induced to form EBs containing neural progenitor cells

using the 4-/4+ retinoic acid treatment protocol. ESCs were cultured in 100 mm petri dishes coated with a 0.1% agar solution (Sigma-Aldrich) in complete media in the absence of LIF and BME for 4 days. Retinoic acid (Sigma-Aldrich) at 500 nM was then added to the complete media for the final 4 days of culture. Media was changed every other day during the eight day process.

5.5.3 Seeding of EBs and Dissociated Cells

In a typical procedure, 1 mL of neural basal media containing B27 supplement (Invitrogen) was diluted by 1:50 and added to each well of a 24-well plate (Corning, Corning, NY) containing nanofiber samples. Three EBs were seeded onto the surface of PCL sample in each well. The media was not changed for the rest of the experiment. In order to investigate the differentiation of dissociated cells on the surface of PCL scaffold, EBs were dissociated using trypsin and ~1× 10^5 cells were seeded into each well of 24-well plate and cultured as described above.

5.5.4 Recording of Extracellular Action Potentials

Extracellular action potentials were recorded using tungsten-epoxy electrodes (0.5–1 mω, A-M systems, Aequim, WA) inserted into a culture dish containing neurons derived from dissociated EBs. Electrodes were advanced vertically into the dish (and neuron itself, when necessary) until spiking activity was detected, similar to the standard procedures used for recording neurons in the brain [48, 49]. The recorded voltages were amplified (A-M systems model 1800 AC amplifier) before being digitized and sorted using a waveform template (FHC APC neural spike recording system, Bowdoinham, ME). The recorded action potential typically fired continually at steady intervals and had waveform shapes indicative of neurons.

5.5.5 Co-culture of Neurons and Myoblasts

C2C12 cells were purchased from American Type Culture Collection and proliferated in the medium consisting of DMEM plus 10% FBS and 1% gentamicin and streptomycin. The medium was changed every other day till confluence. C2C12 cells were then seeded on nanofibers and proliferated for 3 days. Then, the medium was changed to differentiating medium (DMEM supplemented with 2% normal horse serum). After around 5 days, myotubes were formed. Neurons dissociated from EBs were seeded on the myotubes in the presence of neural basal medium containing B27 as a supplement and differentiating medium for myoblasts.

5.5.6 Immunostaining

Immunohistochemical analysis was performed to visualize the spatial distribution of cells and neurites. After 14 days of culture, each well was washed with 1 mL of PBS (Invitrogen) and then fixed for 30 min with 400 µL of 3.7% formaldehyde. When necessary, cells were then permeabilized using 400 µL of 0.1% Triton-X 100 in PBS for 30 min. Cells were blocked with 400 µL of 5% normal goat serum (NGS; Invitrogen) in PBS for 1 h and incubated with primary antibody overnight at 4 ^{o}C. Tuj1 primary antibody (dilution 1:300) was used to visualize the neurites. Following incubation, each well was washed 3 times with PBS for 5 min each. Secondary antibodies (1:200 dilution) were applied for 1 h at room temperature. Each well was then washed with PBS and fluorescent images were taken using a QICAM fast cooled mono 12-bit camera (Q imaging, Burnaby, BC, Canada) attached to an Olympus microscope with Ocapture 2.90.1 (Olympus, Tokyo, Japan).

5.6 References

[1] Li, D.; Wang, Y.; Xia, Y. Electrospinning of polymeric and ceramic nanofibers as uniaxially aligned arrays. *Nano Lett.* **2003**, *3*, 1167-1171.

[2] Li, D.; Xia, Y. Electrospinning of nanofibers: Reinventing the wheel? *Adv. Mater.* **2004**, *16*, 1151-1170.

[3] Li, D.; Wang, Y.; Xia, Y. Electrospinning nanofibers as uniaxially aligned arrays and layer-by-layer stacked films. *Adv. Mater.* **2004**, *16*, 361-366.

[4] Mazzini, L.; Fagioli, F.; Boccaletti, R.; Mareschi, K.; Oliveri, G.; Olivieri, C.; Pastore, I.; Marasso, R.; Madon, E. Stem cell therapy in amyotrophic lateral sclerosis: A methodological approach in humans. *Amyotroph. Lateral. Sc.* **2003**, *4*, 158-161.

[5] Lindvall, O.; Kokaia, Z. Stem cells for the treatment of neurological disorders. *Nature* **2006**, *441*, 1094-1096.

[6] Lindvall, O.; Kokaia, Z. Stem cells in human neurodegenerative disorders-time for clinical translation? *J. Clin. Invest.* **2010**, *120*, 29.

[7] McKay, R. Stem cells in the central nervous system. *Science* **1997**, *276*, 66-71.

[8] Dawson, T. M.; Dawson, V. L. Molecular pathways of neurodegeneration in Parkinson's disease. *Science* **2003**, *302*, 819-822.

[9] Mitchell, J. D.; Borasio, G. D. Amyotrophic lateral sclerosis. *Lancet* **2007**, *369*, 2031-2041.

[10] Liu, X. Z.; Xu, X. M.; Hu, R.; Du, C.; Zhang, S. X.; McDonald, J. W.; Dong, H. X.; Wu, Y. J.; Fan, G. S.; Jacquin, M. F. Neuronal and glial apoptosis after traumatic spinal cord injury. *J. Neurosci.* **1997**, *17*, 5395-5406.

[11] Bartus, R. T. On neurodegenerative diseases, models, and treatment strategies: Lessons learned and lessons forgotten a generation following the cholinergic hypothesis. *Exp. Neurol.* **2000**, *163*, 495-529.

[12] Meissner, W.; Hill, M. P.; Tison, F.; Gross, C. E.; Bezard, E. Neuroprotective strategies for Parkinson's disease: Conceptual limits of animal models and clinical trials. *Trends Pharmacol. Sci.* **2004**, *25*, 249-253.

[13] Ross, C. A.; Tabrizi, S. J. Huntington's disease: From molecular pathogenesis to clinical treatment. *Lancet Neurol* **2011**, *10*, 83-98.

[14] Barnham, K. J.; Masters, C. L.; Bush, A. I. Neurodegenerative diseases and oxidative stress. *Nat. Rev. Drug Discov.* **2004**, *3*, 205-214.

[15] Wobus, A. M.; Boheler, K. R. Embryonic stem cells: Prospects for developmental biology and cell therapy. *Physiol. Rev.* **2005**, *85*, 635-678.

[16] Reubinoff, B. E.; Pera, M. F.; Fong, C.-Y.; Trounson, A.; Bongso, A. Embryonic stem cell lines from human blastocysts: Somatic differentiation *in vitro*. *Nat. Biotechnol.* **2000**, *18*, 399-404.

[17] Lee, S.-H.; Lumelsky, N.; Studer, L.; Auerbach, J. M.; McKay, R. D. Efficient generation of midbrain and hindbrain neurons from mouse embryonic stem cells. *Nat. Biotechnol.* **2000**, *18*, 675-679.

[18] Zhang, S.-C.; Wernig, M.; Duncan, I. D.; Brüstle, O.; Thomson, J. A. *In vitro* differentiation of transplantable neural precursors from human embryonic stem cells. *Nat. Biotechnol.* **2001**, *19*, 1129-1133.

[19] Kim, J.-H.; Auerbach, J. M.; Rodríguez-Gómez, J. A.; Velasco, I.; Gavin, D.; Lumelsky, N.; Lee, S.-H.; Nguyen, J.; Sánchez-Pernaute, R.; Bankiewicz, K.; McKay, R. D. Dopamine neurons derived from embryonic stem cells function in an animal model of Parkinson's disease. *Nature* **2002**, *418*, 50-56.

[20] Wichterle, H.; Lieberam, I.; Porter, J. A.; Jessell, T. M. Directed differentiation of embryonic stem cells into motor neurons. *Cell* **2002**, *110*, 385-397.

[21] Schnell, E.; Klinkhammer, K.; Balzer, S.; Brook, G.; Klee, D.; Dalton, P.; Mey, J. Guidance of glial cell migration and axonal growth on electrospun nanofibers of poly(ε-caprolactone) and a collagen/poly(ε-caprolactone) blend. *Biomaterials* **2007**, *28*, 3012-3025.

[22] Xie, J.; MacEwan, M. R.; Willerth, S. M.; Li, X.; Moran, D. W.; Sakiyama-Elbert, S. E.; Xia, Y. Conductive core–sheath nanofibers and their potential application in neural tissue engineering. *Adv. Funct. Mater.* **2009**, *19*, 2312-2318.

[23] Xie, J.; MacEwan, M. R.; Li, X.; Sakiyama-Elbert, S. E.; Xia, Y. Neurite outgrowth on nanofiber scaffolds with different orders, structures, and surface properties. *ACS Nano* **2009**, *3*, 1151-1159.

[24] Koh, H.; Yong, T.; Chan, C.; Ramakrishna, S. Enhancement of neurite outgrowth using nano-structured scaffolds coupled with laminin. *Biomaterials* **2008**, *29*, 3574-3582.

[25] Xie, J.; Liu, W.; MacEwan, M. R.; Bridgman, P. C.; Xia, Y. Neurite outgrowth on electrospun nanofibers with uniaxial alignment: The effects of fiber density, surface coating, and supporting substrate. *ACS Nano* **2014**, *8*, 1878-1885.

[26] Corey, J. M.; Lin, D. Y.; Mycek, K. B.; Chen, Q.; Samuel, S.; Feldman, E. L.; Martin, D. C. Aligned electrospun nanofibers specify the direction of dorsal root ganglia neurite growth. *J. Biomed. Mater. Res. A* **2007**, *83*, 636-645.

[27] Patel, S.; Kurpinsku, K.; Quigley, R.; Gao, H.; Hsiao, B. S.; Poo, M.; Li, S. Bioactive nanofibers: Synergistic effects of nanotopography and chemical signaling on cell guidance. *Nano Lett.* **2007**, *7*, 2122-2128.

[28] Wang, H. B.; Mullins, M. E.; Cregg, J. M.; Hurtado, A.; Oudega, M.; Trombley, M. T.; Gilbert, R. J. Creation of highly aligned electrospun poly(L-lactic) acid fibers for nerve regeneration applications. *J. Neural Eng.* **2009**, *6*, 016001.

[29] Lee, J. Y.; Bashur, C. A.; Gomez, N.; Goldstein, A. S.; Schmidt, C. E. Enhanced polarization of embryonic hippocampal neurons on micron scale electrospun fibers. *J. Biomed. Mater. Res. A* **2010**, *92*, 1398-1406.

[30] Yang, F.; Murugan, R.; Wang, S.; Ramakrishna, S. Electrospinning of nano/micro scale poly(L-lactic) acid aligned fibers and their potential in neural tissue engineering. *Biomaterials* **2005**, *26*, 2603-2610.

[31] Liu, X.; Chen, J.; Gilmore, K. J.; Higgins, M. J.; Liu, Y.; Wallace, G. G. Guidance of neurite outgrowth on aligned electrospun polypyrrole/poly (styrene-*β*-isobutylene-*β*-styrene) fiber platforms. *J. Biomed. Mater. Res. A* **2010**, *94*, 1004-1011.

[32] Costa, L.; Luda, M.; Trossarelli, L.; Brach del Prever, E.; Crova, M.; Gallinaro, P. Oxidation in orthopaedic uhmwpe sterilized by gamma-radiation and ethylene oxide. *Biomaterials* **1998**, *19*, 659-668.

[33] Ranella, A.; Barberoglou, M.; Bakogianni, S.; Fotakis, C.; Stratakis, E. Tuning cell adhesion by controlling the roughness and wettability of 3D micro/nano silicon structures. *Acta Biomater.* **2010**, *6*, 2711-2720.

[34] Horbett, T.; Waldburger, J.; Ratner, B.; Hoffman, A. Cell adhesion to a series of hydrophilic-hydrophobic copolymers studies with a spinning disc apparatus. *J. Biomed. Mater. Res.* **1988**, *22*, 383-404.

[35] Lampin, M.; Warocquier-Clérout, R.; Legris, C.; Degrange, M.; Sigot-Luizard, M. Correlation between substratum roughness and wettability, cell adhesion, and cell migration. *J. Biomed. Mater. Res.* **1997**, *36*, 99-108.

[36] Xie, J.; MacEwan, M. R.; Ray, W. Z.; Liu, W.; Siewe, D. Y.; Xia, Y. Radially aligned, electrospun nanofibers as dural substitutes for wound closure and tissue regeneration applications. *ACS Nano* **2010**, *4*, 5027-5036.

[37] Martins, A.; Pinho, E. D.; Faria, S.; Pashkuleva, I.; Marques, A. P.; Reis, R. L.; Neves, N. M. Surface modification of electrospun polycaprolactone nanofiber meshes by plasma treatment to enhance biological performance. *Small* **2009**, *5*, 1195-1206.

[38] Lewis, A. K.; Bridgman, C. Nerve growth cone lameuipodia contain two populations of actin filaments that differ in organization and polarity. *J. Cell Biol.* **1992**, *119*, 1219-1243.

[39] Rochlin, M. W.; Itoh, K.; Adelstein, R. S.; Bridgman, P. C. Localization of myosin ii a and b isoforms in cultured neurons. *J. Cell Sci.* **1995**, *108*, 3661-3670.

[40] Lin, C.; Espreafico, E.; Mooseker, M.; Forscher, P. Myosin drives retrograde F-actin flow in neuronal growth cones. *Neuron* **1996**, *16*, 769-782.

[41] Turney, S. G.; Bridgman, P. C. Laminin stimulates and guides axonal outgrowth via growth cone myosin II activity. *Nat. Neurosci.* **2005**, *8*, 717-719.

[42] Rathjen, F. G.; Wolff, J. M.; Chang, S.; Bonhoeffer, F.; Raper, J. A. Neurofascin: A novel chick cell-surface glycoprotein involved in neurite-neurite interactions. *Cell* **1987**, *51*, 841-849.

[43] Maness, P. F.; Schachner, M. Neural recognition molecules of the immunoglobulin superfamily: Signaling transducers of axon guidance and neuronal migration. *Nat. Neurosci.* **2006**, *10*, 19-26.

[44] Lamoureux, P.; Buxbaum, R. E.; Heidemann, S. R. Direct evidence that growth cones pull. *Nature* **1989**, *340*, 159-162.

[45] Barnett, M. W.; Larkman, P. M. The action potential. *Prac. Neurol.* **2007**, *7*, 192-197.

[46] Xie, J.; Willerth, S. M.; Li, X.; Macewan, M. R.; Rader, A.; Sakiyama-Elbert, S. E.; Xia, Y. The differentiation of embryonic stem cells seeded on electrospun nanofibers into neural lineages. *Biomaterials* **2009**, *30*, 354-362.

[47] Liu, W.; Yeh, Y.-C.; Lipner, J.; Xie, J.; Sung, H.-W.; Thomopoulos, S.; Xia, Y. Enhancing the stiffness of electrospun nanofiber scaffolds with a controlled surface coating and mineralization. *Langmuir* **2011**, *27*, 9088-9093.

[48] Watkins, P. V.; Barbour, D. L. Specialized neuronal adaptation for preserving input sensitivity. *Nat. Neurosci.* **2008**, *11*, 1259-1261.

[49] Watkins, P. V.; Barbour, D. L. Level-tuned neurons in primary auditory cortex adapt differently to loud *versus* soft sounds. *Cereb. Cortex* **2011**, *21*, 178-190.

CHAPTER 6

SUMMARY AND FUTURE DIRECTIONS

6.1 Summary

This dissertation explores the potential of using electrospun nanofibers with uniaxial alignment as scaffolds for repairing tissues with anisotropic structures, with a focus on tendon-to-bone insertions, tendons, and nerves. Various modifications were made to improve the functionality of the nanofibers in their niches. For tendon-to-bone insertion repair, minerals were coated onto the nanofibers in a graded fashion to mimic the compositional transition at the native enthesis. The scaffolds wer e then employed to induce the graded osteogenesis of ASCs *in vitro*. As a result, a gradient in the density of osteoblasts and pre-osteoblasts, which was positively correlated with the mineral content, were established. I also developed another method for generating a gradient in cell density on electrospun nanofibers. Briefly, the scaffold was inserted into a homogeneous suspension of cells at a tilted angle. Since the number of cells above the scaffold varied, a gradient in cell density could be established after cell sedimentation. Reverse gradients in TFBs and osteoblasts were fabricated by two sequential seedings, with the scaffold rotated horizontally by 180 degrees in between. Both approaches were able to generate a gradient in cell phenotypes on aligned nanofibers, making them a class of promising scaffolds for repairing injuries at tendon-to-bone insertion.

To enhance stiffness at the highly mineralized end of a graded scaffold, I modified the coating solution to coat the nanofibers with a thicker mineral layer. Compared to the regular coating solution (10SBF), the new formulation, m10SBF, had a higher concentration of HCO_3^-, which promoted the generation of HA with a smaller grain size. In addition, I pre-coated the scaffolds with negatively-charged heparin to further encourage

initial nucleation of HA on the surface of the nanofibers. Consequently, nanofibers with a significantly higher stiffness were fabricated.

As for tendon repair, a method of generating controllable crimps in aligned nanofibers was developed to mimic the crimped microstructure and recapitulate the non-linear stiffening behavior of tendon. I used ethanol as a plasticizer to release the residual stress retained in the nanofibers after electrospinning. With ethanol treatment, the nanofibers were induced to retract to different extents, resulting in crimps of various degrees in nanofibers. Crimped nanofibers fabricated using this method have mechanical characteristics similar to native tendon, giving the TFBs cultured on them a higher tolerance on strain.

Nerve is another type of anisotropic tissue whose regeneration can be enhanced by the application of aligned nanofibers. Depending on the strength of adhesion, neurites derived from ESCs can extend in a direction either parallel (strong adhesion) or perpendicular (weak adhesion) to fiber alignment. In addition, I also characterized the maturation of neurons derived from dissociated EBs on nanofibers by measuring their extracellular action potential and ability to form neuromuscular junctions when co-cultured with muscle cells. All these demonstrations help build a foundation for using aligned nanofibers as scaffolds in neural tissue engineering.

6.2 Future Directions

This dissertation focuses on the development of tissue engineering scaffolds based on aligned nanofibers and the assessment of cellular response to such scaffolds *in vitro*. Work accomplished in this dissertation lays the foundation for the ultimate goal of applying these scaffolds in patients to boost the regeneration events and facilitate healing. To be able to achieve this ultimate goal, plenty of work still needs to be done. Future work should mostly be devoted to the *in vivo* testing of the scaffolds, or deeper understanding of the interaction between cells and their substrates, should more appropriate *ex vivo* tissue

models be developed in next few years. Some immediate future work pertaining to the projects in this dissertation is described in the following context.

6.2.1 Nanofibers with Graded Mineral Coatings for Tendon-to-bone Insertion Repair

The majority of future work for tendon-to-bone insertion repair lies in assessing the scaffold with a graded mineral coating *in vivo*. Our groups have already piloted one set of experiments to explore the regenerative capacity of such scaffolds in a rotator cuff injury/repair model in rats. Four experimental groups were tested, including suture only, acellular scaffold, scaffolds seeded with ASCs (cellular group), and scaffolds seeded with ASCs transfected with an advenovirus that can produce bone morphogenetic protein 2 (BMP2) fusion protein (BMP2 group) [1]. In the three groups repaired with scaffolds, a 5×5 mm^2 scaffold was attached over the repaired insertion, with the mineralized end placed over the bone, while the unmineralized end was placed over the tendon. Figure 6.1 shows a schematic, how the scaffold was placed during surgery.

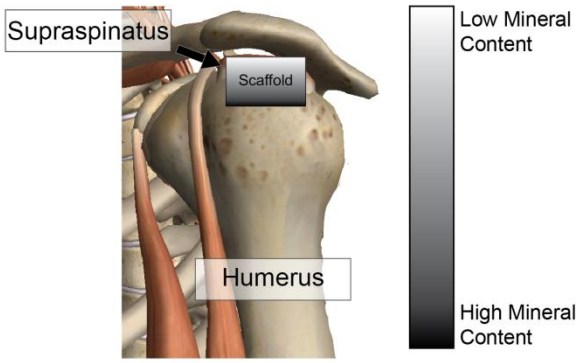

Figure 6.1. *The scaffold was placed over the repair site in an effort to guide healing. The mineralized end was placed over the bone, and the unmineralized was placed over the tendon.*

Micro-computed tomography (microCT) was performed to measure the density and volume of two important areas: the scarred tendon-to-bone insertion, and the trabecular bone of the humeral head (Figure 6.2A). Scar characteristics were measured in a 4 mm

region near the tendon-to-bone attachment of the supraspinatus tendon. Trabecular bone morphometry was measured in a volume of interest spanning approximately 2.5 mm between the growth plate and the epiphyseal surface, excluding the cortical bone. Measurements of the scar showed that scar size was not significantly affected by the treatment or timepoint, suggesting that the scar was neither expanding nor condensing during the time between day 28 and 56 (Figure 6.2B). Trabecular bone data showed that at day 28, there were significantly less trabeculae in the BMP2 group. After day 56, however, the trabecular bone parameters among the groups were not statistically different (Figure 6.2C). Trabecular thickness was not statistically different among groups, either (Figure 6.2D).

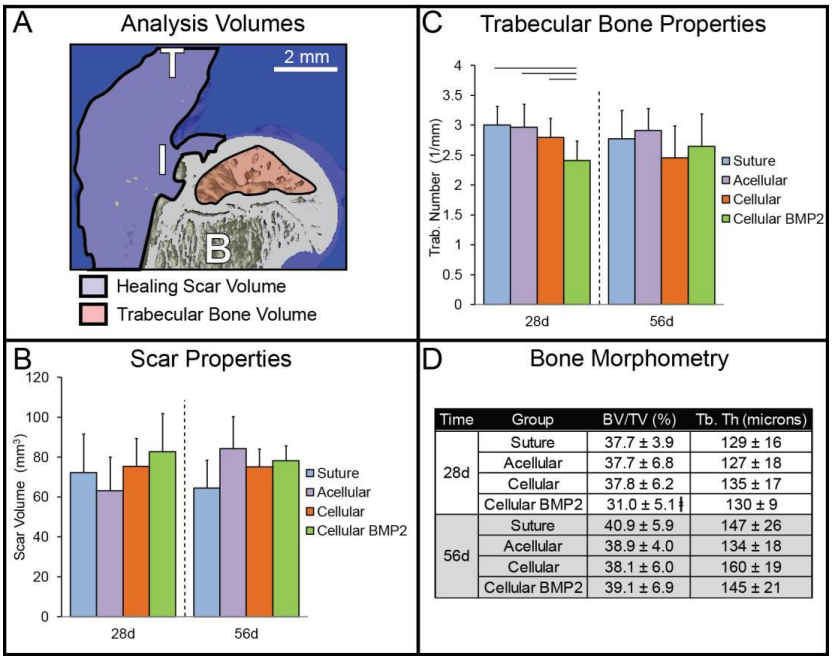

Time	Group	BV/TV (%)	Tb. Th (microns)
28d	Suture	37.7 ± 3.9	129 ± 16
	Acellular	37.7 ± 6.8	127 ± 18
	Cellular	37.8 ± 6.2	135 ± 17
	Cellular BMP2	31.0 ± 5.1‡	130 ± 9
56d	Suture	40.9 ± 5.9	147 ± 26
	Acellular	38.9 ± 4.0	134 ± 18
	Cellular	38.1 ± 6.0	160 ± 19
	Cellular BMP2	39.1 ± 6.9	145 ± 21

Figure 6.2. *(A) Representative 3D reconstruction of repaired attachment. Regions of analysis are indicated by the shaded areas (blue: scar volume, red: trabecular bone) (B: Bone, I: Insertion, T: Tendon) (B) Scar volume was similar in all groups. (C) Trabecular number was significantly lower in the 28 d cellular BMP2 group compared to other 28 d groups. (D) Bone volume as a percentage of total volume (BV/TV) was decreased in the cellular BMP2 group compared to other groups at day 28, but there was no difference at day 56. (Mean + SD, line: p<0.05).*

Average stress-strain curves appeared similar among the groups, and over time stresses increased (Figures 6.3, A and B). The BMP2 group had significantly lower strength than the acellular group at day 28. The same was lower in the acellular group when compared to the suture group at day 56 (Figure 6.3C). The modulus was lower in the BMP2 group when compared to the suture group at day 56. Also, modulus was lower in the acellular group when compared to the suture group at day 56 (Figure 6.3D).

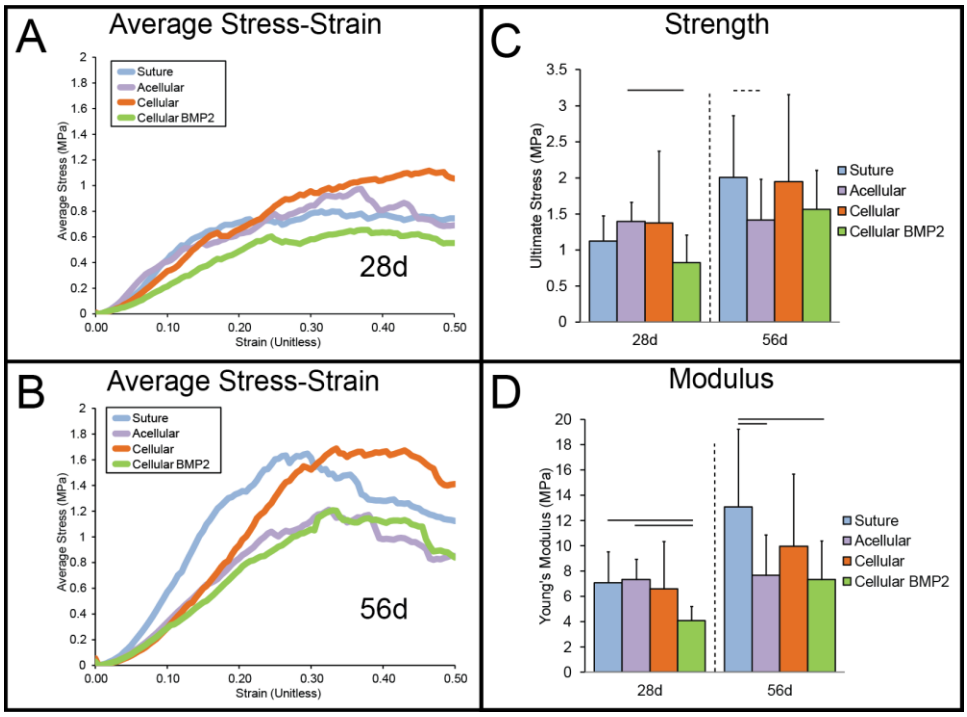

Figure 6.3. *(A) Average stress-strain curves for 28 d groups and (B) 56 d groups. (C) Ultimate stress (i.e., strength) and (D) Modulus for four groups at day 28 and 56. (Bars: Mean + SD, dashed line: $p<0.1$, solid line: $p<0.05$)*

In general, these results collectively suggested that none of the three groups repaired with scaffolds had a statistically significant improvement on tendon-to-bone healing when compared with the suture only group. The major reason lies in that the rat rotator cuff model is very small, requiring skilled surgeons and repeatable surgical

techniques. In this study, scaffold placement was crucial, and could be a source of variability. Moreover, instead of being placed between tendon and bone, the scaffolds were placed on top of the insertion after the regular surgery was performed. This placement forces the scaffolds to rely solely on proximity and diffusion to affect the regeneration at the insertion site. Since the insertion in rats is too small for the surgeons to place the scaffolds in their biological footprint, a larger animal model, such as rabbit, would therefore be more appropriate for assessing the regeneration capacity of the nanofiber scaffolds with a gradient in mineral content. Future endeavors will be devoted to constructing a new injury/repair model in rabbits, followed by developing a better way to integrate the scaffolds into the injured site, in order to see whether improved regeneration can be achieved.

6.2 Crimped Nanofibers for Tendon Repair

In Chapter 4, I have shown that crimps in nanofibers were capable of protecting the TFBs from static mechanical strain. How the TFBs will respond to recurrent loading remains unexplored. In native tendon, the TFBs often experience repetitive mechanical loading with various degrees of strain [2]. Cyclic loading, therefore, better replicates the mechanical dynamics in native tendon.

When subjected to cyclic loading, the proliferation rate and production of transforming growth factor-beta (TGF-β), platelet-derived growth factor (PDGF), and basic fibroblast growth factor (bFGF) of the TFBs were upregulated [3-7]. Moreover, the expression levels of collagen genes I, III, and XII, as well as aggrecan, fibronectin, prolyl hydroxylase, and tenascin, were consistent with those of TFBs in native tendon [8-10]. Furthermore, cyclic loading is capable of promoting the differentiation of MSCs into the fibroblastic lineage [11]. Taken together, these results indicate that cyclic mechanical stretching may have a positive impact on tendon healing through stimulation of cell proliferation, differentiation, and matrix formation.

However, the elastic substrates used in the aforementioned studies were composed of either non-biodegradable materials such as silicone and other rubbers [3, 9, 10], or collagen gel that does not mimic the anisotropic structure of tendon [8]. Aligned nanofibers with crimps therefore provide certain advantage as tissue engineering scaffolds for tendon repair. Future endeavors may be devoted to investigating the cellular behavior (viability, proliferation, and differentiation, among others) on crimped nanofibers under cyclic loading, and eventually, assessing their regeneration potential *in vivo*.

6.3 Aligned Nanofibers for Neural Tissue Engineering

In Chapter 5, I demonstrated that neurons derived from dissociated EBs were able to mature on nanofibers. It is noteworthy that neuronal cultures derived from dissociated EBs usually contain various neuronal subtypes and non-neural cells such as glia [12-15]. The major type of glia cells derived from ESCs is astrocytes, which usually lead to scar formation [16-18]. Minimizing the percentage of astrocytes in the cell population is therefore critical to promoting the regenerative capacity of ESC therapy. My preliminary results showed that few cells were stained positively for glial fibrillary acidic protein (GFAP) when PCL nanofibers were used as the substrate, regardless of their topography (Figure 6.4, A-D), whereas the percentage of astrocytes was ~40% for cells derived from dissociated EBs cultured on TCPS (Figure 6.4, E and F). The potential reason for the reduction in population of astrocytes may lie in the ability of the nanofibers to suppress the proliferation of astrocytes. For example, Chew *et al.* demonstrated that electrospun poly[caprolactone-*co*-(ethyl ethylene phosphate)] nanofibers could significantly inhibit the proliferation rate of rat cortical astrocytes, while promoting apoptosis and gene-silencing [19, 20].

A systematic investigation of the mechanism underlying this inhibition effect of nanofibers on astrocytes is still in its infancy. For example, it is not clear whether this effect is unique to nano-sized structures. Future work dedicated to understanding the interaction

between astrocytes and nanofibers will further broaden the application of nanofiber scaffolds for neural tissue engineering.

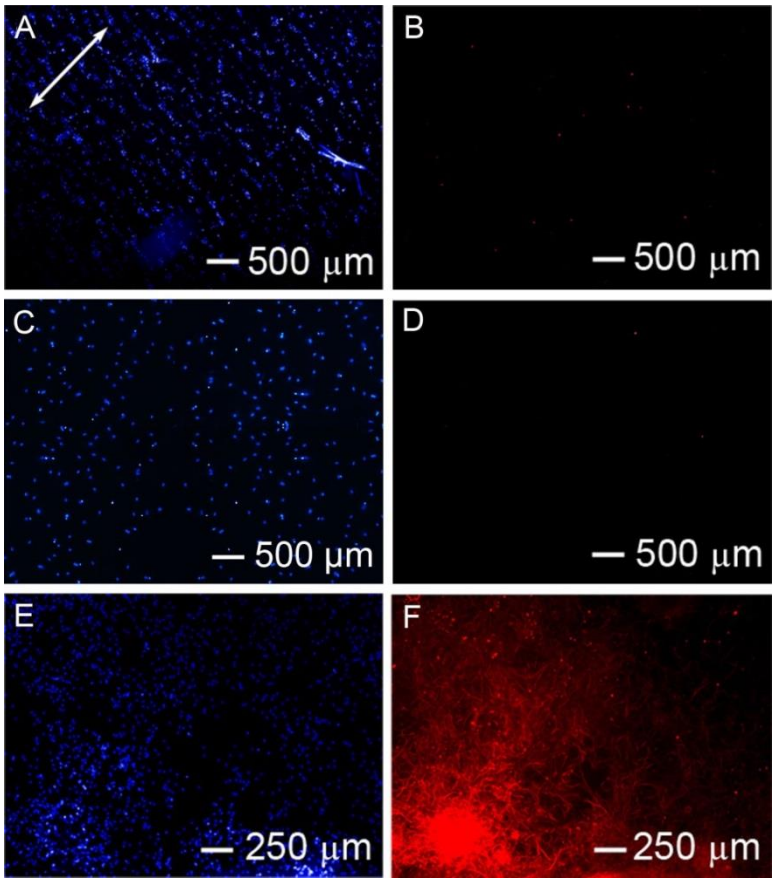

Figure 6.4 *Fluorescence images showing (A, C, E) DAPI straining for cell nuclei and (B, D, F) GFAP staining for astrocyptes. Cells were maintained on (A, B) aligned nanofibers, (C, D) random nanofibers, and (E, F) TCPS for 14 days in neural basal medium. No positive GFAP stain for cells cultured on nanofibers can be seen, while a large population of the cells cultured on TCPS differentiated into astrocytes.*

6.4 References

[1] Tsuji, K.; Bandyopadhyay, A.; Harfe, B. D.; Cox, K.; Kakar, S.; Gerstenfeld, L.; Einhorn, T.; Tabin, C. J.; Rosen, V. BMP2 activity, although dispensable for bone formation, is required for the initiation of fracture healing. *Nat. Genet.* **2006**, *38*, 1424-1429.

[2] Almekinders, L. C.; Banes, A. J.; Ballenger, C. A. Effects of repetitive motion on human fibroblasts. *Med. Sci. Sport. Exer.* **1993**, *25*, 603-607.

[3] Zeichen, J.; van Griensven, M.; Bosch, U. The proliferative response of isolated human tendon fibroblasts to cyclic biaxial mechanical strain. *Am. J. Sports Med.* **2000**, *28*, 888-892.

[4] Skutek, M.; Griensven, M.; Zeichen, J.; Brauer, N.; Bosch, U. Cyclic mechanical stretching modulates secretion pattern of growth factors in human tendon fibroblasts. *Eur. J. Appl. Physiol.* **2001**, *86*, 48-52.

[5] Petersen, W.; Varoga, D.; Zantop, T.; Hassenpflug, J.; Mentlein, R.; Pufe, T. Cyclic strain influences the expression of the vascular endothelial growth factor (VEGF) and the hypoxia inducible factor 1 alpha (HIF-1α) in tendon fibroblasts. *J. Orthop. Res.* **2004**, *22*, 847-853.

[6] Wang, J. H.-C.; Jia, F.; Yang, G.; Yang, S.; Campbell, B. H.; Stone, D.; Woo, S. L.-Y. Cyclic mechanical stretching of human tendon fibroblasts increases the production of prostaglandin E2 and levels of cyclooxygenase expression: A novel *in vitro* model study. *Connect. Tissue Res.* **2003**, *44*, 128-133.

[7] Arnoczky, S. P.; Tian, T.; Lavagnino, M.; Gardner, K.; Schuler, P.; Morse, P. Activation of stress-activated protein kinases (SAPK) in tendon cells following cyclic strain: The effects of strain frequency, strain magnitude, and cytosolic calcium. *J. Orthop. Res.* **2002**, *20*, 947-952.

[8] Yang, G.; Crawford, R. C.; Wang, J. H. Proliferation and collagen production of human patellar tendon fibroblasts in response to cyclic uniaxial stretching in serum-free conditions. *J. Biomech.* **2004**, *37*, 1543-1550.

[9] Garvin, J.; Qi, J.; Maloney, M.; Banes, A. J. Novel system for engineering bioartificial tendons and application of mechanical load. *Tissue Eng.* **2003**, *9*, 967-979.

[10] Screen, H. R.; Shelton, J. C.; Bader, D. L.; Lee, D. A. Cyclic tensile strain upregulates collagen synthesis in isolated tendon fascicles. *Biochem. Bioph. Res. Co.* **2005**, *336*, 424-429.

[11] Qiu, Y.; Lei, J.; Koob, T. J.; Temenoff, J. S. Cyclic tension promotes fibroblastic differentiation of human MSCs cultured on collagen-fibre scaffolds. *J. Tissue Eng. Regen. Med.* **2014**. DOI: 10.1002/term.1880

[12] Xie, J.; Willerth, S. M.; Li, X.; Macewan, M. R.; Rader, A.; Sakiyama-Elbert, S. E.; Xia, Y. The differentiation of embryonic stem cells seeded on electrospun nanofibers into neural lineages. *Biomaterials* **2009**, *30*, 354-362.

[13] Willerth, S. M.; Arendas, K. J.; Gottlieb, D. I.; Sakiyama-Elbert, S. E. Optimization of fibrin scaffolds for differentiation of murine embryonic stem cells into neural lineage cells. *Biomaterials* **2006**, *27*, 5990-6003.

[14] Perrier, A. L.; Tabar, V.; Barberi, T.; Rubio, M. E.; Bruses, J.; Topf, N.; Harrison, N. L.; Studer, L. Derivation of midbrain dopamine neurons from human embryonic stem cells. *Proc. Natl. Acad. Sci. USA* **2004**, *101*, 12543-12548.

[15] Kalyani, A.; Hobson, K.; Rao, M. S. Neuroepithelial stem cells from the embryonic spinal cord: Isolation, characterization, and clonal analysis. *Dev. Biol.* **1997**, *186*, 202-223.

[16] Brüstle, O.; Jones, K. N.; Learish, R. D.; Karram, K.; Choudhary, K.; Wiestler, O. D.; Duncan, I. D.; McKay, R. D. Embryonic stem cell-derived glial precursors: A source of myelinating transplants. *Science* **1999**, *285*, 754-756.

[17] Zhang, S.-C.; Wernig, M.; Duncan, I. D.; Brüstle, O.; Thomson, J. A. *In vitro* differentiation of transplantable neural precursors from human embryonic stem cells. *Nat. Biotechnol.* **2001**, *19*, 1129-1133.

[18] Reubinoff, B. E.; Pera, M. F.; Fong, C.-Y.; Trounson, A.; Bongso, A. Embryonic stem cell lines from human blastocysts: Somatic differentiation *in vitro*. *Nat. Biotechnol.* **2000**, *18*, 399-404.

[19] Cao, H.; Marcy, G.; Goh, E. L. K.; Wang, F.; Wang, J.; Chew, S. Y. The effects of nanofiber topography on astrocyte behavior and gene silencing efficiency. *Macromol. Biosci.* **2012**, *12*, 666-674.

[20] Min, S. K.; Kim, S. H.; Kim, C. R.; Paik, S.-M.; Jung, S.-M.; Shin, H. S. Effect of topography of an electrospun nanofiber on modulation of activity of primary rat astrocytes. *Neurosci. Lett.* **2013**, *534*, 80-84.

APPENDIX A

COPYRIGHT INFORMATION

Chapter 1; Figures 1.1, 1.4:

Reprinted (adapted) with permission from Ref. 11. Copyright 2010 American Chemical Society.

Chapter 1; Figures 1.3A:

Reprinted (adapted) with permission from Ref. 18. Copyright 2008 Elsevier.

Chapter 1; Figures 1.3B:

Reprinted (adapted) with permission from Ref. 19. Copyright 2005 Publishing House of Warmia and Mazury in Olsztyn (Poland).

Chapter 2; Figure 2.1-2.12:

Reprinted (adapted) with permission from Ref. 13. Copyright 2014 American Chemical Society.

Chapter 2; Figure 2.13-2.20:

Reprinted (adapted) with permission from Ref. 14. Copyright 2013 Wiley-VCH.

Chapter 3; Table 3.1, Figures 3.1–3.5:

Reprinted (adapted) with permission from Ref. 12. Copyright 2011 American Chemical Society.

Chapter 5; Figure 5.1:

Reprinted (adapted) with permission from Ref. 23 Copyright 2014 American Chemical Society.

VITA

WENYING LIU

LIU was born in Nanchang, Jiangxi, China. She received her B.S. degree in Biological Engineering from School of Chemical Engineering and Technology at Tianjin University in 2009. She then came to the U.S. and pursued her Ph.D. degree in Department of Energy, Environmental, and Chemical Engineering at Washington University in St. Louis until December 2011. She then relocated with Dr. Younan Xia to School of Chemical and Biomolecular Engineering at Georgia Institute of Technology. Her research interests include the production of electrospun nanofibers and exploration of their applications in regenerative medicine. In spare time, she enjoys cooking, traveling, reading, and music.